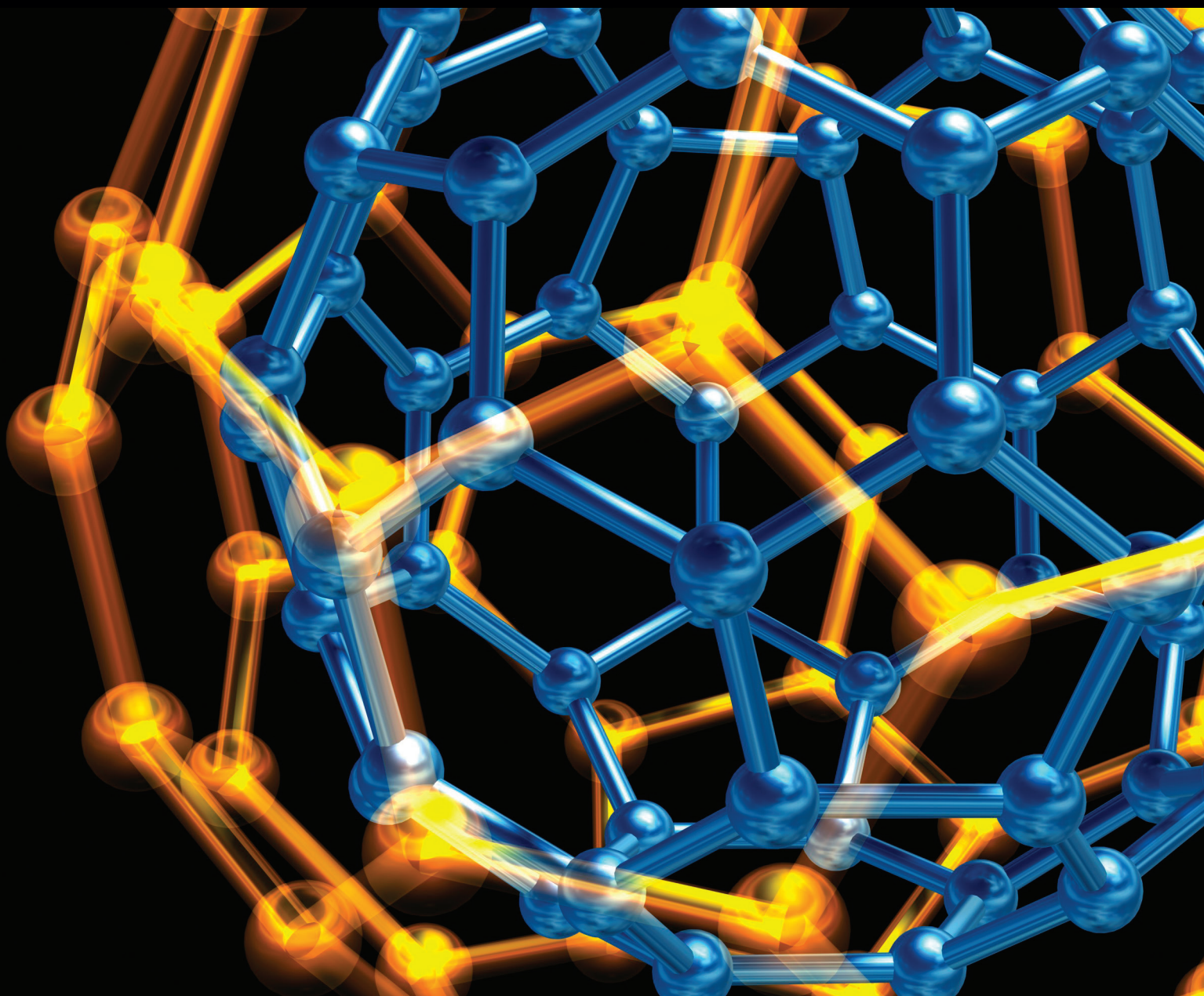# Micro/Nanofabrication and Characterization of Advanced Materials and Devices

Lead Guest Editor: Yanxi Li
Guest Editors: Liang He, Mengyu Yan, and Zhengjun Wang

Micro/Nanofabrication and Characterization of Advanced Materials and Devices

Micro/Nanofabrication and Characterization of Advanced Materials and Devices

Lead Guest Editor: Yanxi Li
Guest Editors: Liang He, Mengyu Yan, and Zhengjun Wang

Editorial Board

Contents

Editorial

Micro/Nanofabrication and Characterization of Advanced Materials and Devices

Yanxi Li,[1] **Liang He,**[2] **Mengyu Yan** ⬤,[3] **and Zhengjun Wang**[4]

[1]*Department of Materials Science and Engineering, Virginia Tech, Blacksburg, VA 24061, USA*
[2]*State Key Laboratory of Advanced Technology for Materials Synthesis and Processing, Wuhan University of Technology, Wuhan 430070, China*
[3]*Department of Materials Science and Engineering, University of Washington, Seattle, WA 98195, USA*
[4]*Department of Physics and Astronomy, West Virginia University, Morgantown, WV 26506, USA*

Correspondence should be addressed to Mengyu Yan; myyan@uw.edu

The controllable fabrication of materials/devices in micro- and nanoscale, which is supported by advanced characterization, is the key for nanotechnology revolution. Compared to decades ago when the so-called nanotechnology was restricted to the literature, we have made it a reality. Some specific fields, silicon chips fabrication for example, have touched the nanoeffect and are working on avoiding the quantum effects. In another hotspot field, energy storage and conversion, we have seen the dawn of nanomaterials. The energy storage capability and conversion efficiency increased by folds upon nanosizing the materials. The uncontrollable side reactions in chemistry, however, are still a challenge in looking for better batteries, supercapacitors, and catalysts. Thus, rational and controllable fabrication of nanomaterials is needed. In this special issue, we can find some recent updates in nanotechnology.

Bacterial adhesion on medical devices leads to severe infections, which trouble people a lot. A group from Colombia has developed a superficial modification technique to decrease bacterial adhesion on steel 316L by one fold. Importantly, this magic bacterial adhesion thin film can also be transferred to other substrates. The scientists from The University of Manchester created a methodology for scalable fabrication of TiO_2 nanotubes on Ti and Ti alloys. The diameters of the TiO_2 nanotubes are controllable from 25 to 100 nm. It is worth emphasizing that a 7.5 times lower cost is achieved by using the new methodology above. Another development in nanotubes is reported by a Malaysian research group. They functionalized the carbon nanotubes and used them to detect benzene contents in the atmosphere. Benzene, as a carcinogenic chemical, has been widely used in plastics and other polymer products. These carbon nanotube chemical sensors would be meaningful in monitoring benzene contents in workplaces of Malaysia and other Southeast Asian countries. The last two papers were contributed from China, Iran, and Iraq. Bing Han et al. optimized supercapacitors by modulating the pore structure of carbon flakes. A high capacitance and superior rate performance are achieved in lamellar activated carbons. It is worth noting that there is only 0.4% capacitance decay in these supercapacitors even after 2000 long cycles.

Conflicts of Interest

The authors declare that there are no conflicts of interest regarding the publication of this paper.

Yanxi Li
Liang He
Mengyu Yan
Zhengjun Wang

Research Article

A Novel Methodology for Economical Scale-Up of TiO$_2$ Nanotubes Fabricated on Ti and Ti Alloys

Juan Shong Khaw [iD],[1] **Michele Curioni,**[1] **Peter Skeldon,**[1] **Christopher R. Bowen** [iD],[2] **and Sarah H. Cartmell** [iD][1]

[1]*School of Materials, The University of Manchester, Manchester M13 9PL, UK*
[2]*Department of Mechanical Engineering, University of Bath, Bath BA2 7AY, UK*

Correspondence should be addressed to Sarah H. Cartmell; sarah.cartmell@manchester.ac.uk

The prospective use of nanotechnology for medical devices is increasing. While the impact of material surface nanopatterning on the biological response is convincing, creating a large surface area with such nanotechnology remains an unmet challenge. In this paper, we describe, for the first time, a reproducible scale-up manufacturing technique for creating controlled nanotubes on the surfaces of Ti and Ti alloys. We describe an average of approximately 7.5-fold increase in cost and time efficiency with regards to the generation of 20, 50, and 100 nm diameter nanotubes using an anodisation technique. These novel materials have great potential in the medical field through their influence on cellular activity, in particular, protein absorption, focal adhesion, and osteoinduction. In this paper, we provide a step-by-step guide to optimise an anodisation system, starting with design rationale, proof of concept, device upscaling, consistency, and reproducibility check, followed by cost and efficiency analysis. We show that the optimised device can produce a high number of anodised specimens with customisable specimen shape at reduced cost and time, without compromising the repeatability and consistency. The device can fabricate highly uniform and vertically oriented TiO$_2$ nanotube layer with desired pore diameters.

1. Introduction

Nanotubular films on titanium (Ti) and Ti alloys are used in a significant number of applications including biomedical devices [1–4], dye-sensitised solar cells [5–12], and photocatalysis [13–17]. Figure 1(a) shows the increasing trend in the number of publications focusing on titanium oxide (TiO$_2$) nanotubes within the last ten years; Figure 1(b) presents the applications of TiO$_2$ nanotubes and their respective percentages among the published papers in year 2017.

For the biomedical field, a wide range of target applications have been reported regarding TiO$_2$ nanotubes grown on Ti and its alloys, for instance, drug delivery [18–20], antibacterial [21–23], biosensors [24–26], and dental and bone implants [22, 27–29]. In particular, the increasing demand for dental and hip implants is becoming a prime turnover in the orthopaedic industry [30–32]. *In vitro* and *in vivo* investigations for implant applications often require a high number of specimens for assessing the biocompatibility of the biomaterials (typically a minimum of 30 specimens for fundamental biocompatibility assays). Currently, the production rate of such surfaces is slow and limited to the production of a single specimen at a time [33, 34], hence the rationale for an improved scale-up methodology was used that allows the rapid, reproducible production of specimens.

Recently, titanium and a variety of titanium alloys, including Ti-6Al-4V, Ti-6Al-4V-ELI (extra low interstitial), Ti-6Al-7Nb, and Ti-13Nb-13Zr, have received significant attention due to their exceptional material properties. In particular, they demonstrate high corrosion resistance, high biocompatibility, low stiffness, and low density [2, 35–37]. They have thus been widely used as implant materials to replace failed hard tissues, more specifically, in the area of bone plates, dental implants, fracture fixation screws, and total knee and hip replacement [35, 38–40].

(a)

*approximate number of publications in Year 2017

(b)
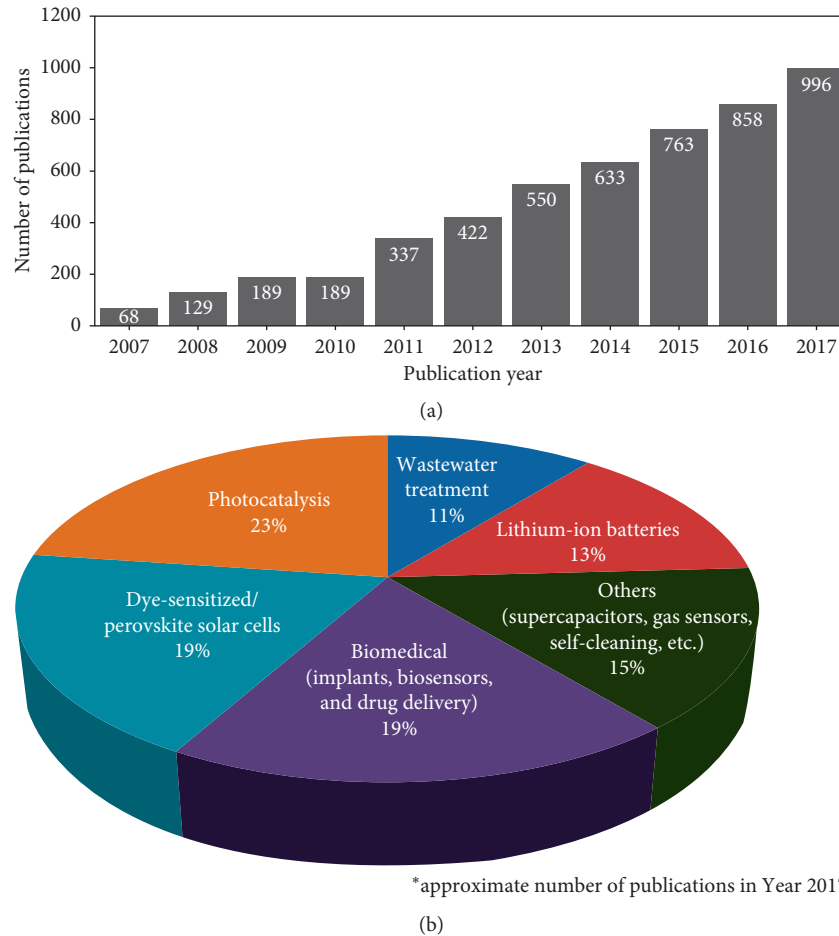
FIGURE 1: (a) The increasing trend outlining the number of papers published on TiO_2 nanotubes from 2007 to 2017 (data were obtained from the Science Direct database on Oct 1, 2018, using keywords of "TiO_2 nanotube" with result filters of review articles and research articles under the article type); (b) range of applications of TiO_2 nanotubes and their respective percentage with regard to the number of published papers within the area of TiO_2 nanotubes in the year 2017 (data were obtained from the Science Direct database on Oct 1, 2018, using keywords "TiO2" and "nanotube" and "*corresponding keywords shown in the pie chart*," with result filters of review articles and research articles under the article type and year 2017).

The high surface-to-volume ratio of TiO_2 nanotubes grown on both pure titanium and titanium alloys have been demonstrated to promote excellent protein adsorption [41–43] and to offer a platform for cell adhesion, proliferation, and differentiation, leading to the enhancement of osseointegration [22, 44–46]. Research has demonstrated that a small change in the nanotube pore size can significantly affect cellular behaviour [22, 29, 47–49], while nanotube length does not have a major impact on cellular response [50]. It is suggested that pore size changes the arrangement and strength of the focal contacts made by cells. Cells grown on nanoporous or nanotubular surfaces exhibit an upregulation in the integrin receptors that mediate the focal contacts with resulting improvements in cytoadherence, mechanotransduction, and hydroxyapatite formation [45, 51, 52].

Anodisation using a fluoride-containing electrolyte has been long recognised as a promising method to synthesise nanotubular structures on titanium substrates. Compared with other nanotube fabrication methods such as sol-gel

template [39, 53–58] and hydrothermal techniques [59–64], electrochemical anodisation has the advantages of being simple, rapid, low cost, and providing more controllable and reproducible results for the preparation of highly ordered and vertically oriented TiO_2 nanotube layer [65–67]. The surface morphology and desired nanotube dimensions can be readily controlled by tailoring the anodising conditions, including the applied potential, electrolyte composition, and pH [1, 2, 34]. If an optimised condition is achieved, anodisation can effectively and consistently enable the formation of self-assembled and uniformly aligned nanotube arrays [68–70].

Electrochemical anodisation is an electrolytic method used to increase the thickness of the natural oxide layer on metal surfaces [71] and to create biocompatible micro- or nanoporous TiO_2 coatings, with increased surface energy and roughness [72, 73]. During anodisation, aqueous or organic electrolytes with fluoride ions are generally employed to produce the nanotubes. Some examples of the electrolytes include aqueous electrolyte solutions with acids,

e.g., H_2SO_4 or H_3PO_4 [51, 74]; salts, e.g., $(NH_4)_2SO_4$ or Na_2SO_4 [75]; and organic electrolytes with glycerol or ethylene glycol [76, 77].

Anodisation experiments are usually carried out in a two-electrode or three-electrode electrochemical system, with Ti or a Ti alloy as the anode, inert platinum foil as the cathode, and in the case of a three-electrode system, an Ag or AgCl electrode as the reference electrode [2]. TiO_2 nanotubes can be obtained either under a constant potential (potentiostatic) or constant current (galvanostatic) mode. Anodisation can be performed using specimens of a variety of shapes and sizes, depending on the maximum allowable load of the power source [72]. The thickness and morphology of the oxide layers formed are usually determined by the applied potential, the duration of the anodisation process, and the chemical composition of the electrolyte used [71]. Previous works have concluded that, at a given time point using the same electrolyte, the nanotube pore diameter, interpore distance, and nanotube length are directly proportional to the applied potential [67, 78–81].

A detailed growth mechanism of TiO_2 nanotube using anodisation techniques is described in the literature [33, 74, 82, 83]. Briefly, the stages of nanotube formation in an aqueous electrolyte under constant potential can be monitored by the changes of current over the anodising time. As the anodising potential is initially applied, the current rapidly decays to a minimum due to the formation of a high-resistance oxide layer. Subsequently, the current rises to a maximum with the development of pore nucleation and the formation of a porous structure. The current will eventually attain an approximately constant value when an equilibrium state is achieved, i.e., the rate of oxide formation is equaled by the rate of dissolution.

Conventional anodisation systems are usually limited for production of *in vitro* specimens by the following factors: (i) anodising is limited to a specific specimen rather than the entire surface, leading to material wastage; (ii) trimming of specimens for *in vitro* studies causes specimen damage; (iii) usually only one specimen can be accommodated in the system, and high volume production is typically expensive in cost and time; and (iv) consistency and reproducibility cannot be guaranteed from specimens to specimens due to small variations in the anodising conditions. Figure 2 shows the schematic diagrams of typical conventional anodisation systems, in which the desired anodised area is defined by an O-ring on the specimen holder.

The limitations above highlight the need for a tailored anodisation device design to produce fully anodised surfaces and to increase the productivity and repeatability of the anodisation process. In the present work, we designed an optimised anodisation setup to reduce fabrication costs and to maximise the efficiency rate of anodising titanium discs, for the first time, with the following objectives: (i) to anodise the entirety of specimen surfaces so as to reduce excessive material waste; (ii) to increase the number of specimens per anodised batch; (iii) to anodise batches of specimens with consistent results; (iv) to anodise specimens of desired TiO_2 nanotube pore diameters; (v) to customise the specimen shape for actual practical application, in our case, for *in vitro* biocompatibility

tests; (vi) to evaluate the current cost per complete anodised specimen associated with the optimised device.

2. Materials and Methods

Pure Ti foils (thickness 0.25 mm; purity 99.5%; Alfa Aesar) and Ti-6Al-4V foils (thickness 0.4064 mm; titanium grade 5 ASTM B265; William Gregor Ltd.) were cut to the desired shape using an iPG laser ytterbium fiber laser 1 kW cutting tool, or AgieCharmilles CUT 200 Sp EDM wire-cut machine.

Before electrochemical treatment, the titanium foils were ultrasonically degreased in equal volumes of acetone, ethanol, and deionised (DI) water for 5 minutes, followed by drying under a cool air stream. An additional pickling process was introduced to Ti-6Al-4V foils prior to anodisation using a pickling mixture (Sigma-Aldrich) containing hydrofluoric acid, nitric acid, and DI water for five minutes to remove the naturally formed oxide layer.

For the electrochemical experiments, an anodising device with a three-electrode configuration was used. Specimens were mounted onto a copper rod wrapped with heat-shrink polytetrafluoroethylene (PTFE) tubing; areas other than the circular working area of the specimens were masked with lacquer (Stopper 45 MacDermid) to prevent exposure to the electrolyte. A platinum foil (thickness 0.1 mm; purity 99.99%; Alfa Aesar) served as the counter electrode, placed at 40 mm distance from the working electrode. A saturated calomel Hg/Hg_2Cl_2 (1M KCl) electrode was used as a reference electrode, connected to the setup by a salt bridge placed close to the working electrode.

Constant potentials were applied using an EG&G Instruments Scanning Potentiostat (Model 362) connected to a Ministat MKIV Sycopel Scientific signal amplifier; the *in situ* current-time responses (per anodisation process) were recorded using Labview software. The current density was then plotted using the current-time data per total surface area of the working specimens.

For pure Ti specimens, the electrolyte consisted of a mixture of 1M H_3PO_4 and 0.25 wt% HF. For Ti-6Al-4V titanium alloy specimens, 1M H_2SO_4 containing 0.1 wt% HF was used. All anodisation experiments were carried out at room temperature for 60 minutes. After the electrochemical treatment, the specimens were rinsed with DI water and then ultrasonically cleaned for 10 minutes and further dried under a cool air stream.

In the following, the specimens are designated according to the material type and anodising potential; for example, TiNT-2.5V refers to Ti specimens anodised at 2.5V to create nanotubes (NT), while Ti64NT-20V refers to Ti-6Al-4V specimens anodised at 20V. As shown in Figure 3, Version A of the anodisation setup used only one specimen, while Version B accommodated 10 specimens and a larger platinum foil as the counter electrode. The specimen was designed to fit into *in vitro* tissue culture plates and with a tag to assist handling of specimens using tweezers. To verify that the anodisation setup was applicable to alloy, the present work was being reproduced using Ti-6Al-4V foils. The preparation time and costs for both versions were recorded and analysed.
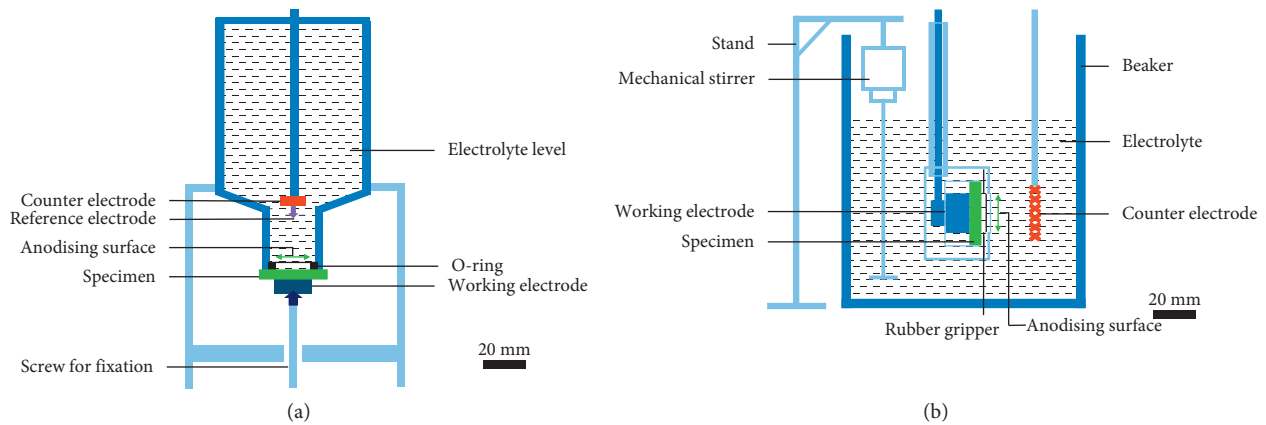
(a)

(b)

Figure 2: Typical conventional anodisation systems used in material fabrication laboratories. The number and position of electrodes involved, the configuration, and the area of anodising surface; (a) top-bottom with three-electrode configuration, reported by Molchan [34]; (b) left-right with two-electrode configuration, reported by Regonini [33, 84]. The specimen (working electrode) used in both systems is bounded by an O-ring or a rubber gripper, resulting in an anodising surface of approximately 20 mm in diameters.

The anodised specimens were characterised using a ZEISS Ultra 55 field emission scanning electron microscope (FE-SEM) equipped with an energy dispersive X-ray spectrometer (EDS), as reported previously [85]. The FE-SEM was operated under the InLens detector mode with 5 kV EHT in a high vacuum environment. ImageJ image analysis software was used to measure the nanotube pore diameters, interpore distances, and nanotube lengths of the anodised specimens.

Statistical significance was analysed using analysis of variance (ANOVA) and counter-confirmed using the two-tailed paired Student's t-test in Microsoft Excel. Data are presented as mean ± standard deviation (S.D.). Probability (p value) less than 0.05 was considered to be significant.

3. Results and Discussion

3.1. Design Rationales. While designing the new anodisation device, the design rationales of the device setup were initially evaluated, followed by proof of concept data, leading to further upscale and optimisation. The design rationales included the following:

 (i) To create a scalable device design that was suitable for multiple specimens per batch of the anodisation process

 (ii) Maintain constant electrode distances for process control

 (iii) Ensure device setup that was compatible with the use of hydrofluoric acid (HF)

 (iv) Allow an even distribution of potential and current to all specimens

 (v) Allow monitoring of the potential of the working electrode during the anodisation process

 (vi) Include a counter electrode that was at least similar or larger area to that of the working electrode

 (vii) Allow no contamination from copper parts, which deleteriously affects the anodising process and *in vitro* cell and tissue culture tests

 (viii) Allow manufacture of a specimen shape that maximises the surface area for *in vitro* tests

 (ix) Allow ease of use when transferring the specimens during *in vitro* assays post manufacture

A PTFE beaker was employed to contain the electrolyte as PTFE is resistant to HF, as compared with glass or other plastic materials like low-density polyethylene (LDPE), high-density polyethylene (HDPE), polypropylene (PP), polymethylpentene (PMP), and styrene acrylonitrile (SAN). The PTFE beaker can also be autoclaved under high temperature if needed. The holder for the working electrode was a copper rod (shielded by PTFE and lacquer masking to prevent copper from exposing to the electrolyte) to which specimens were attached. Anodisation was able to take place over the entirety of the specimen, and the specimen shape could be varied according to the application.

The platinum counter-electrode was also attached to a shielded copper rod holder. The counter-electrode was positioned 40 mm from the working electrode holder. Figure 3 shows a detailed schematic of the device setup. In Version B, as the surface area of the working electrode was increased, the area of the counter-electrode was increased to be at least similar to that of the working electrode. Two square platinum foils (50 mm × 50 mm) were welded to provide an electrode of area approximately 94 mm × 50 mm.

The reference electrode was placed close to the working electrode to monitor the changes of potentials across the systems. Lacquer was used to seal connections of the platinum and specimens to the copper rods. The top cover jig of the device permitted the electrode arrangements to be preserved between batches. An opening in the cover jig allowed access of air.

As the bottom well diameter of a commonly used 24 circular well plates is 15.54 mm, as shown in Figure 3(c), a disc-shaped specimen was adopted with a diameter of 14 mm and area 3.08 cm^2. In Version A of the device design, a single specimen was anodised. In Version B, 10 wire-cut electrical discharge machining (EDM) connected specimens
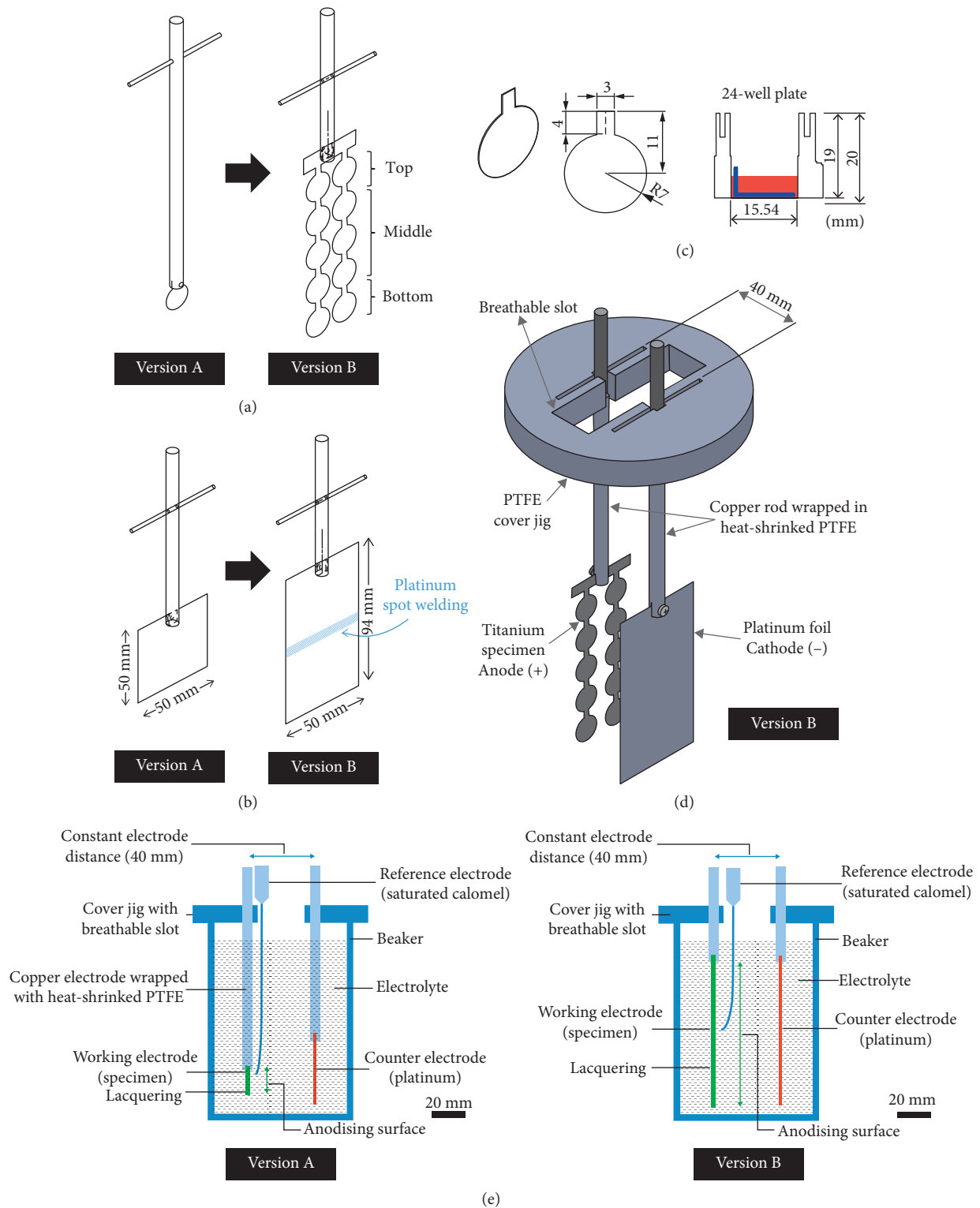
FIGURE 3: (a) The design optimisation of Version A to Version B with 10x increase of specimens per anodisation; (b) spot weld of two pieces of platinum foil as the size of counter-electrode should be at least, if not larger than the overall area of the working electrode; (c) the specimen shape after cut using a precision cutting device; the tag can be folded into L shape for cell and tissue culture activity; (d) full configuration of the optimised anodisation device (Version B); (e) the schematic comparison of the two versions; note that the anodising surface on Version B was dramatically increased as compared with Version A.

were anodised. The specimens could be later readily separated by cutting the connecting strips between the discs provided by the metal sheet cutting procedure. The resulting tags on each disc could be folded into L shape to ease the transference of specimens without damaging the specimen surface and living cell culture during *in vitro* tests. The

number of specimens was limited to 10 to be compatible with the output of the power supply.

3.2. Proof of Concept.

Version A, as illustrated in Figure 3, was used for initial proof of concept. The schematic of the full anodisation setup is displayed in Figure 3(e). The current density response recorded during anodising of a titanium specimen at 20V is shown in Figure 4. After the first few seconds of anodisation, the current fell and decayed to approximately $1.0 \, \text{mA} \, \text{cm}^{-2}$ due to the initial formation of a barrier layer and subsequent development of the nanotube layer. A uniform array of nanotubes was observed on the anodised specimens; the top view FE-SEM micrograph is displayed in Figure 5(e). The pore diameters (∼100 nm), as shown in Figure 6(a) TiNT-20V, are comparable to that reported by Bauer et al. [80].

3.3. Upscaling and Optimisation.

The full 3D render of the optimised device (Version B) can be seen in Figure 3(d), and the schematic of the setup is displayed in Figure 3(e). The schematic compares the upscaling of the anodising surface in Version B as compared with Version A. To a greater extent, the actual anodising surface of Version B was two times as shown in the schematic, as there were two connected strips of five specimens (total $n = 10$) per anodisation batch. As the geometry of the working electrode and the anodisation system is symmetrical, the current passing through the system was considered evenly distributed.

When determining the maximum number of specimens allowed in the system, it is necessary to consider the maximum allowable load and current for the anodisation power supply with respect to the applied potential and total anodising surface area. In theory, considering that the current flows homogeneously across the system, the potentiostat used in this work would allow more than 20 specimens per batch if the anodising potential was under or about 20V. However, due to practical safety and constraints, the number of specimens was set to $n = 10$ per batch so to ensure that the power supply was not overloaded.

The current density responses for each experiment using the 10-specimen setup (Version B) are presented in Figure 4. These results are consistent with those of other studies [86–88] and suggest that current density increased with an increase in anodising potential.

As presented Figures 5 and 6, nanotube dimensions measured from the FE-SEM top view of the pure titanium specimens indicated that increasing potential led to an increase in the mean nanotube pore diameter, interpore distance, and nanotube length. In addition to the pore diameter and nanotube length, the interpore distance is also a crucial indicator of the consistency of the pore nucleation and dissolution rate in an anodisation process [33, 83]. The EDS analysis showed that elements of titanium and oxygen were found on the anodic layer, with traces of carbon and fluorine. The data presented above were proportional to the previously reported studies [48, 69, 80].

The nanotube dimensions, morphology, and EDS analysis of the anodised Ti-6Al-4V titanium alloy specimens showed a similar trend to those reported in previous
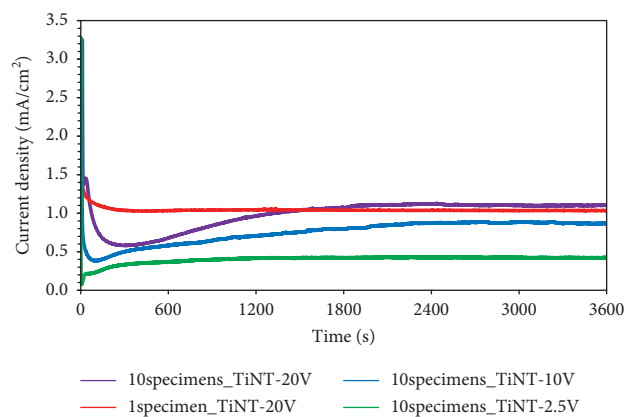
FIGURE 4: Current density recorded over time corresponding to the number of specimens per anodisation and their respective anodising potentials.

publications [79, 89–92]. The EDS analysis revealed that the anodic layer was composed of titanium, aluminium, vanadium, oxygen, and traces of carbon and fluorine. As the applied potential (20V) was the same as that applied to pure titanium specimens (TiNT-20V), the nanotube pore diameter of the anodised Ti-6Al-4V specimens (Ti64NT-20V) was almost similar. However, the nanotube length of the anodised Ti-6Al-4V specimens appeared to be shorter than that of the anodised pure titanium specimens. It could be due to the different electrolyte and base material composition used, as well as the effect of the additional pickling process before the anodisation is carried out to remove the naturally occurred oxide layer. These phenomena have been previously demonstrated in other comparable studies [90, 93, 94]. In addition to that, the literature has also shown that changes in nanotube length are the least significant for the modulation of cellular behaviour [50], unlike the pore size and interpore distance, which are important. The overall results substantiated that the imperative dimensions of the nanotube were exquisitely controlled.

3.4. Consistency and Reproducibility Check.

Current density curves were monitored during every anodisation batch to ensure the consistency of the electrochemical treatment. After anodisation, the morphology and elemental composition of the anodised specimens were characterised using FE-SEM and EDS to confirm the absence of contaminating elements, irregular distribution, or any inconsistency of the nanotube array.

As the anodisation outcomes using both Version A and Version B were expected to be similar, the nanotube dimensions, including pore diameter, interpore distance, and nanotube length, of the anodised specimens using both versions were measured and compared. The morphologies of subsequent batches of anodised specimens were also examined to evaluate the reliability and reproducibility using the optimised device (Version B). Data analysis presented in Figure 6 concluded that the multiple measurements on different batches were consistent as there was no statistically significant difference, i.e., a p value greater than 0.05, between Version A and each of the four batches of Version B
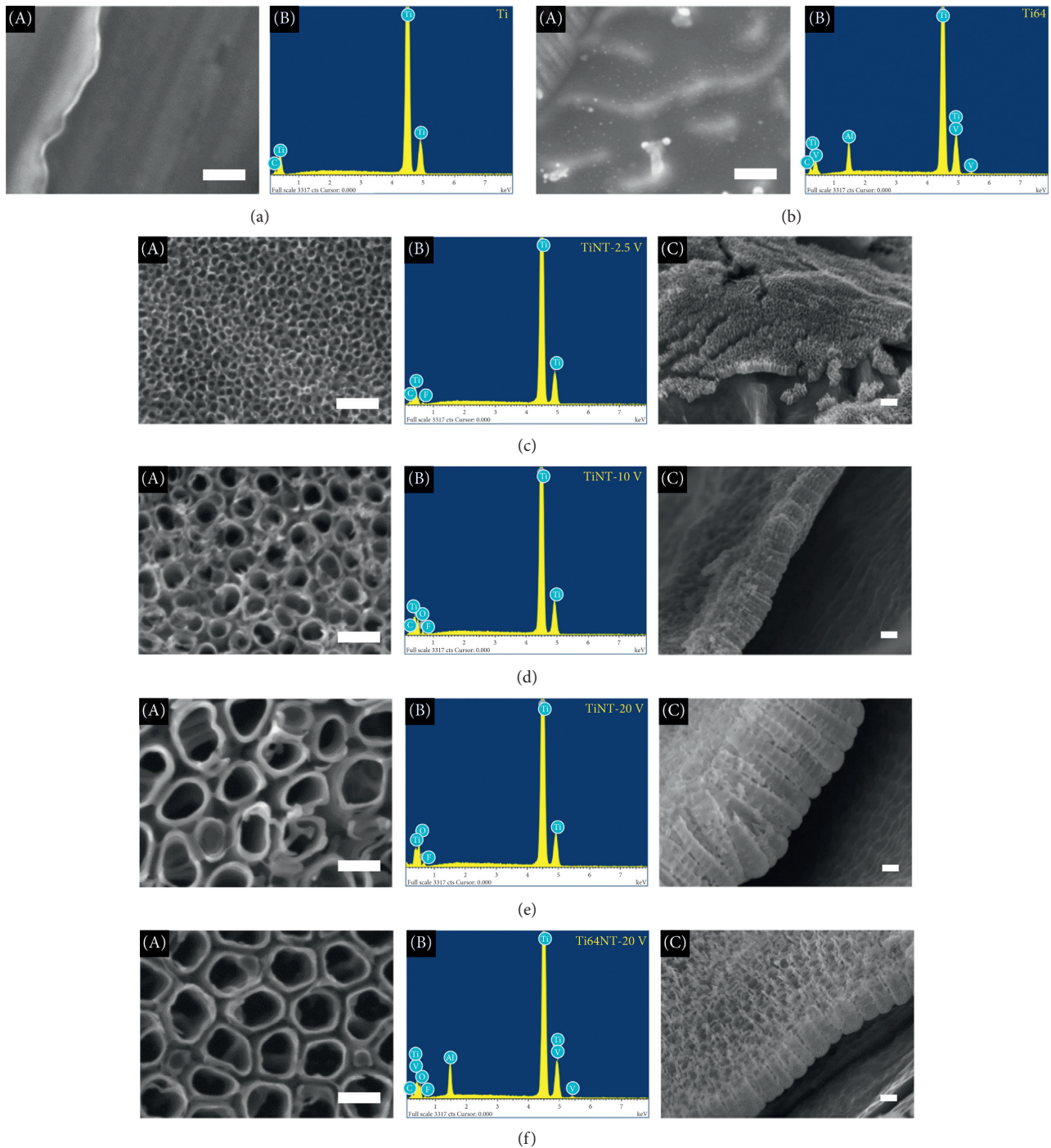
Figure 5: Top view FE-SEM micrographs (A); respective EDS analysis (B); cross sections of the nanotube layer (C); base material: pure titanium (a) and Ti-6Al-4V (b); anodised specimens (c)–(f). Scale bar = 100 nm. (a) Ti. (b) Ti64. (c) TiNT-2.5V. (d) TiNT-10V. (e) TiNT-20V. (f) Ti64NT-20V.

anodised at their respective anodising potentials, regardless of the position of the specimen in the specimen holder.

3.5. Cost Analysis.
As the specimens were of customised shape, the use of cutting devices was included in the cost analysis. Two commonly used precision automated disc cutting techniques were compared: fiber laser cutting (Method 1) and wire-cut EDM (Method 2). The corresponding costs are displayed in Table 1.

Both cutting methods offer an accurate and precise cutting result, although some burr or burnt edges can be found following Method 1. Method 1 was favoured in terms of staff costs and turnaround time. However, the consumable cost of Method 2 was slightly lower because the sheet metal can be stacked into a pile and cut using EDM, whereas
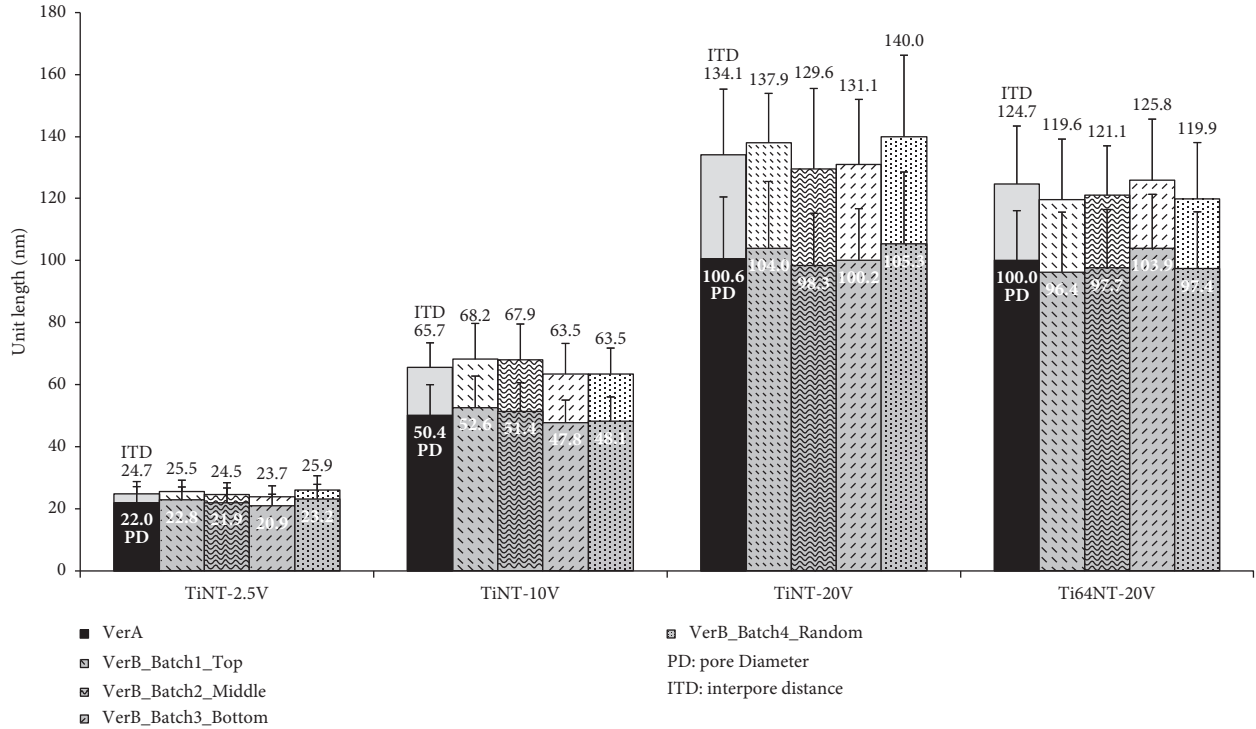
(a)
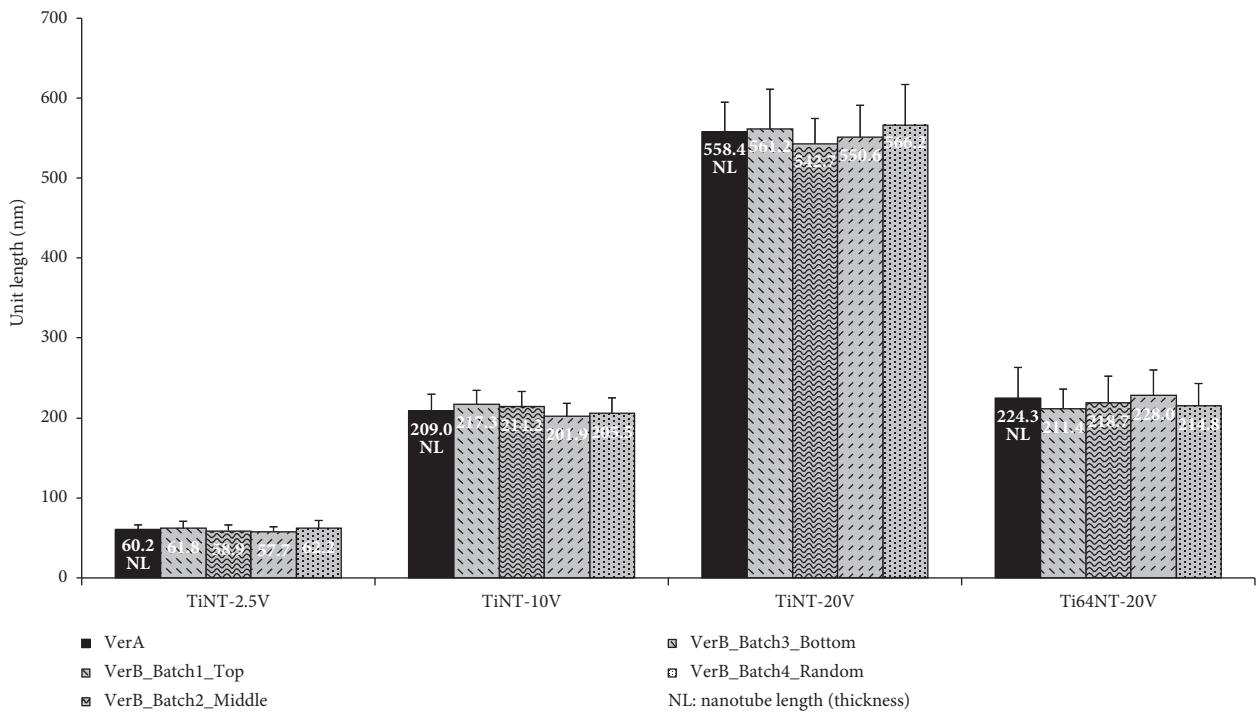
(b)

FIGURE 6: Statistical plots of the nanotube dimensions correspond to their respective anodising potentials; (a) the pore diameter (lower bar, labelled PD) and the interpore distance (upper bar, labelled ITD) of the anodised specimen using Version A (first bar with solid black fill) and one specimen from each of the four batches using Version B (bars with patterned fill), chosen from different positions in the 10-specimen holder, i.e., top corner, middle, bottom corner, and random position, as indicated in Figure 3. (a) $n = 100$, error bars represent standard deviation; (b) the nanotube length of the anodised specimens, measured using the same specimen as (a) ($n = 15$, error bars represent standard deviation).

Table 1: Cost analysis of the disc cutting methods. Titanium foils (thickness 0.25 mm; purity 99.5%; 100 × 2000 mm; Alfa Aesar) were used. Staff rate of £20 per hour was considered as a typical wage for technical staff members trained to graduate level in the UK (prices current June 2018).

Disc cutting methods	Method 1 (laser cut)	Method 2 (wire-cut EDM)
Disc cutting device name	iPG laser ytterbium fiber laser 1 kW cutting tool	AgieCharmilles CUT 200 sp EDM wire-cut machine
Associated consumables	2 protecting optics-£142; 2 pressurised argon gas tank-£30	2 EDM brass cutting wires 0.25 mm-£100
Total staff hours (£20/hr)	4 hours-£80	6 hours-£120
Total materials costs	Ti foil of 0.25 × 100 × 2000-£364	Ti foil of 0.25 × 100 × 2000-£364
Gross cost (a)	£616	£584
Total cut specimens (b)	313	450
Actual usable specimens (c)	281	419
Rejection rate ((b − c) × 100/b)	10.2%	6.9%
Estimated cost per usable specimen ($d = a/c$)	**£2.19**	**£1.39**

Table 2: Time and cost analysis comparing the two anodisation device designs. Wire-cut EDM (cutting Method 2) was adopted for calculating the costs due to its overall advantages. Staff rate of £20 per hour was incorporated as a typical wage for technical staff members trained to graduate level in the UK (prices current June 2018).

Descriptions	Version A	Version B
Number of specimens at one anodisation process	1 specimen	10 specimens
Preparation time per anodisation batch*	$a_1 = 1.5$ hr	$b_1 = 2$ hr
Anodisation time per anodisation batch	$a_2 = 1$ hr	$b_2 = 1$ hr
Preparation time for 30 specimens†	$a_3 = a_1 \times 30 = 45$ hr	$b_3 = b_1 \times 3 = 6$ hr
Anodisation time for 30 specimens	$a_4 = a_2 \times 30 = 30$ hr	$b_4 = b_2 \times 3 = 3$ hr
Total time for anodising 30 specimens	$a_5 = a_3 + a_4 = 75$ hr	$b_5 = b_3 + b_4 = 9$ hr
Total labour time per anodised specimen	$a_6 = a_5/30 = $ **150 min**	$b_6 = b_5/30 = $ **18 min**
% increase in time efficiency compared to version A (A/B ∗ 100)	—	833
Total labour cost per specimen (staff rate £20/hour)	$a_7 = a_6 \times 20 = £\ 50.00$	$b_7 = b_6 \times 20 = £\ 6.00$
Estimated cost per usable specimen, d_{T2} (carried from Table 1)	£ 1.39	£ 1.39
Estimated price of one complete anodised specimen	$a_7 + d_{T2} = $ **£ 51.39**	$b_7 + d_{T2} = $ **£ 7.39**
% increase in cost efficiency compared to version A [A/B ∗ 100]	—	695%

*Specimen preparation time includes deburring, degreasing, assembling, lacquering, cleaning after anodisation, disassembling, sonicating, and packing for sterilisation after anodisation. †"30 specimens" were used as a standard quantity needed for a fundamental *in vitro* statistical assessment, i.e., biocompatibility assays on anodised specimens of different nanotube diameters.

Method 1 can only be used on one sheet at a time, leading to increased use of consumables. Method 2 also has a significantly lower rejection rate. As no dangerous chemicals, gases, or heat dissipation were involved in Method 2, it was generally less hazardous being conducted in an enclosed chamber, and less supervision was required during the operation. Method 2 (wire-cut EDM) was chosen over Method 1 due to its overall advantages, machining quality, and lower price.

In calculating the cost, we assumed that the cutting and anodising operations were conducted by trained personnel costed at a rate of £20 per hour if in the UK. Rejection of pieces could arise due, for example, to scratches, imprecise cutting, alteration of shape, or severe burning. The costs of electricity, apparatus, and chemicals (including cutting machine energy consumption, potentiostat power supply, electrolyte, anodising device construction, etc.) have not been considered.

The time and cost for producing anodised specimens were evaluated, as shown in Table 2. As mentioned, the wire-cut EDM technique was used for the calculations. For Version B, a one-off cost for an extra piece of platinum plus spot welding process was not included. The preparation time prior to biocompatibility test was also included to provide an actual estimation of cost when applied in real applications. As no previous literature has estimated the cost and efficiency of an anodisation setup, Version A was assumed as an approximate replica of the conventional anodisation system because it was capable of producing single anodised specimen at a given time.

Based on the analysis, the total labour time per anodised specimen for Version A was approximately 8.5 times more than that of Version B, owing to anodising of only one specimen in the former. Combining the specimen cutting and labour cost for anodising the specimens, Version B has substantially reduced the cost per anodised specimen by a factor of about 7. Overall, the significant increase in time and cost efficiency as displayed in Table 2 has made the optimised device (Version B) a promising and economical option for anodisation.

4. Conclusions

Our results and cost analysis displayed a promising optimisation of an anodisation device that has a potential for use in various applications and industries, for example, laboratory researches, small-medium enterprises (SMEs), and

cross-disciplinary experiments. The design and methodology used in this study concluded that the new anodisation device is capable of producing a highly ordered uniform TiO$_2$ nanotube layer with tuneable pore diameters for use in, but not limited to, biocompatibility *in vitro* tests. Not only significantly reducing the overall time and costs associated with high volume production of anodised specimens, but also the optimised device successfully provided consistent anodisation results with increased specimen throughput, customisation of the specimen shape, and high reproducibility.

Data Availability

The data used to support the findings of this study are available from the corresponding author upon request.

Conflicts of Interest

The authors declare that there are no conflicts of interest regarding the publication of this paper.

References

[1] X. Liu, P. Chu, and C. Ding, "Surface modification of titanium, titanium alloys, and related materials for biomedical applications," *Materials Science and Engineering: R: Reports*, vol. 47, no. 3-4, pp. 49–121, 2004.

[2] M. Kulkarni, A. Mazare, E. Gongadze et al., "Titanium nanostructures for biomedical applications," *Nanotechnology*, vol. 26, no. 6, article 062002, 2015.

[3] M. Geetha, A. K. Singh, R. Asokamani, and A. K. Gogia, "Ti based biomaterials, the ultimate choice for orthopaedic implants—a review," *Progress in Materials Science*, vol. 54, no. 3, pp. 397–425, 2009.

[4] P. Roy, S. Berger, and P. Schmuki, "TiO$_2$ nanotubes: synthesis and applications," *Angewandte Chemie International Edition*, vol. 50, no. 13, pp. 2904–2939, 2011.

[5] G. K. Mor, K. Shankar, M. Paulose, O. K. Varghese, and C. A. Grimes, "Use of highly-ordered TiO$_2$ nanotube arrays in dye-sensitized solar cells," *Nano Letters*, vol. 6, no. 2, pp. 215–218, 2005.

[6] D. Kuang, J. Brillet, P. Chen et al., "Application of highly ordered TiO$_2$ nanotube arrays in flexible dye-sensitized solar cells," *ACS Nano*, vol. 2, no. 6, pp. 1113–1116, 2008.

[7] J. R. Jennings, A. Ghicov, L. M. Peter, P. Schmuki, and A. B. Walker, "Dye-sensitized solar cells based on oriented TiO$_2$ nanotube arrays: transport, trapping, and transfer of electrons," *Journal of American Chemical Society*, vol. 130, no. 40, pp. 13364–13372, 2008.

[8] B. Liu and E. S. Aydil, "Growth of oriented single-crystalline rutile TiO$_2$ nanorods on transparent conducting substrates for dye-sensitized solar cells," *Journal of American Chemical Society*, vol. 131, no. 11, pp. 3985–3990, 2009.

[9] K. Zhu, T. B. Vinzant, N. R. Neale, and A. J. Frank, "Removing structural disorder from oriented TiO$_2$ nanotube arrays: reducing the dimensionality of transport and recombination in dye-sensitized solar cells," *Nano Letters*, vol. 7, no. 12, pp. 3739–3746, 2007.

[10] M. Paulose, K. Shankar, O. K. Varghese, G. K. Mor, and C. A. Grimes, "Application of highly-ordered TiO$_2$ nanotube-arrays in heterojunction dye-sensitized solar cells," *Journal of Physics D: Applied Physics*, vol. 39, no. 12, pp. 2498–2503, 2006.

[11] T.-S. Kang, A. P. Smith, B. E. Taylor, and M. F. Durstock, "Fabrication of highly-ordered TiO$_2$ nanotube arrays and their use in dye-sensitized solar cells," *Nano Letters*, vol. 9, no. 2, pp. 601–606, 2009.

[12] P. Roy, D. Kim, K. Lee, E. Spiecker, and P. Schmuki, "TiO$_2$ nanotubes and their application in dye-sensitized solar cells," *Nanoscale*, vol. 2, no. 1, pp. 45–59, 2010.

[13] S. P. Albu, A. Ghicov, J. M. Macak, R. Hahn, and P. Schmuki, "Self-Organized, free-standing TiO$_2$ nanotube membrane for flow-through photocatalytic applications," *Nano Letters*, vol. 7, no. 5, pp. 1286–1289, 2007.

[14] Z. Wu, F. Dong, W. Zhao, H. Wang, Y. Liu, and B. Guan, "The fabrication and characterization of novel carbon doped TiO$_2$ nanotubes, nanowires and nanorods with high visible light photocatalytic activity," *Nanotechnology*, vol. 20, no. 23, article 235701, 2009.

[15] C. Li, J. Yuan, B. Han, L. Jiang, and W. Shangguan, "TiO$_2$ nanotubes incorporated with CdS for photocatalytic hydrogen production from splitting water under visible light irradiation," *International Journal of Hydrogen Energy*, vol. 35, no. 13, pp. 7073–7079, 2010.

[16] M. Zlamal, J. Macak, P. Schmuki, and J. Krysa, "Electrochemically assisted photocatalysis on self-organized TiO$_2$ nanotubes," *Electrochemistry Communications*, vol. 9, no. 12, pp. 2822–2826, 2007.

[17] J. M. Macak, M. Zlamal, J. Krysa, and P. Schmuki, "Self-organized TiO$_2$ nanotube layers as highly efficient photocatalysts," *Small*, vol. 3, no. 2, pp. 300–304, 2007.

[18] M. Jarosz, A. Pawlik, M. Szuwarzyński, M. Jaskuła, and G. D. Sulka, "Nanoporous anodic titanium dioxide layers as potential drug delivery systems: drug release kinetics and mechanism," *Colloids and Surfaces B: Biointerfaces*, vol. 143, pp. 447–454, 2016.

[19] N. Çalışkan, C. Bayram, E. Erdal, Z. Karahaliloğlu, and E. B. Denkbaş, "Titania nanotubes with adjustable dimensions for drug reservoir sites and enhanced cell adhesion," *Materials Science and Engineering: C*, vol. 35, pp. 100–105, 2014.

[20] M. Lai, Z. Jin, X. Yang, H. Wang, and K. Xu, "The controlled release of simvastatin from TiO$_2$ nanotubes to promote osteoblast differentiation and inhibit osteoclast resorption," *Applied Surface Science*, vol. 396, pp. 1741–1751, 2017.

[21] X. Chen, K. Cai, J. Fang et al., "Dual action antibacterial TiO$_2$ nanotubes incorporated with silver nanoparticles and coated with a quaternary ammonium salt (QAS)," *Surface and Coatings Technology*, vol. 216, pp. 158–165, 2013.

[22] E. P. Su, D. F. Justin, C. R. Pratt et al., "Effects of titanium nanotubes on the osseointegration, cell differentiation, mineralisation and antibacterial properties of orthopaedic implant surfaces," *Bone and Joint Journal*, vol. 100, no. 1, pp. 9–16, 2018.

[23] A. Roguska, M. Pisarek, A. Belcarz et al., "Improvement of the bio-functional properties of TiO$_2$ nanotubes," *Applied Surface Science*, vol. 388, pp. 775–785, 2016.

[24] J. Tian, Y. Li, J. Dong, M. Huang, and J. Lu, "Photoelectrochemical TiO$_2$ nanotube arrays biosensor for asulam determination based on in-situ generation of quantum dots," *Biosensors and Bioelectronics*, vol. 110, pp. 1–7, 2018.

[25] K.-S. Mun, S. D. Alvarez, W.-Y. Choi, and M. J. Sailor, "A stable, label-free optical interferometric biosensor based on TiO$_2$ nanotube arrays," *ACS Nano*, vol. 4, no. 4, pp. 2070–2076, 2010.

[26] M. Terracciano, V. Galstyan, I. Rea, M. Casalino, L. De Stefano, and G. Sbrevegleri, "Chemical modification of TiO$_2$ nanotube arrays for label-free optical biosensing applications," *Applied Surface Science*, vol. 419, pp. 235–240, 2017.

[27] J. Ni, C. J. Frandsen, K. Noh et al., "Fabrication of thin film TiO$_2$ nanotube arrays on Co-28Cr-6Mo alloy by anodization," *Materials Science and Engineering: C*, vol. 33, no. 3, pp. 1460–1466, 2013.

[28] P. Sharma, S. Cartmell, and A. J. El Haj, "Bone tissue engineering," *Applications of Cell Immobilisation Biotechnology*, vol. 8, pp. 153–166, 2005.

[29] K. S. Brammer, S. Oh, C. J. Cobb, L. M. Bjursten, H. v. d. Heyde, and S. Jin, "Improved bone-forming functionality on diameter-controlled TiO$_2$ nanotube surface," *Acta Biomaterialia*, vol. 5, no. 8, pp. 3215–3223, 2009.

[30] National Joint Registry, *The National Joint Registry for England, Wales, Northern Ireland and the Isle of Man 2015 Public and Patient Guide to the NJR's 12th Annual Report 2015–Hip Replacement Edition*, National Joint Registry, Hemel Hempstead, UK, 2015.

[31] A. Svedbom, E. Hernlund, M. Ivergård et al., "Osteoporosis in the European Union: a compendium of country-specific reports," *Archives of Osteoporosis*, vol. 8, no. 1-2, p. 137, 2013.

[32] Accuracy Research LLP, *Global Orthopedic Implants Market Worth USD 91.42 Billion by 2025 - Analysis, Technologies and Forecasts Report 2016-2025-Vendors: 3M Health Care, Abbott Labs, Baxter International-Research and Markets*, Business Wire, San Francisco, SA, USA, 2016.

[33] D. Regonini, *Anodised TiO$_2$ Nanotubes: Synthesis, Growth Mechanism and Thermal Stability*, University of Bath, Bath, UK, 2008.

[34] T. Molchan, *Generation of Porous and Nanotubular Anodic Films on Titanium and Titanium-Aluminium alloy*, The University of Manchester, Manchester, UK, 2014.

[35] C. N. Elias, J. H. C. Lima, R. Valiev, and M. A. Meyers, "Biomedical applications of titanium and its alloys," *JOM*, vol. 60, no. 3, pp. 46–49, 2008.

[36] N. Ren, S. Zhang, Y. Li et al., "Bone mesenchymal stem cell functions on the hierarchical micro/nanotopographies of the Ti-6Al-7Nb alloy," *British Journal of Oral and Maxillofacial Surgery*, vol. 52, no. 10, pp. 907–912, 2014.

[37] J. M. Hernández-López, A. Conde, J. de Damborenea, and M. A. Arenas, "Correlation of the nanostructure of the anodic layers fabricated on Ti13Nb13Zr with the electrochemical impedance response," *Corrosion Science*, vol. 94, pp. 61–69, 2015.

[38] S. Minagar, C. C. Berndt, J. Wang, E. Ivanova, and C. Wen, "A review of the application of anodization for the fabrication of nanotubes on metal implant surfaces," *Acta Biomaterialia*, vol. 8, no. 8, pp. 2875–2888, 2012.

[39] C. Covarrubias, M. Mattmann, A. Von Marttens et al., "Osseointegration properties of titanium dental implants modified with a nanostructured coating based on ordered porous silica and bioactive glass nanoparticles," *Applied Surface Science*, vol. 363, pp. 286–295, 2016.

[40] L. Lin, H. Wang, M. Ni et al., "Enhanced osteointegration of medical titanium implant with surface modifications in micro/nanoscale structures," *Journal of Orthopaedic Translation*, vol. 2, no. 1, pp. 35–42, 2014.

[41] L. S. Jung, J. S. Shumaker-Parry, C. T. Campbell, S. S. Yee, and M. H. Gelb, "Quantification of tight binding to surface-immobilized phospholipid vesicles using surface plasmon resonance: binding constant of phospholipase A$_2$," *Journal of American Chemical Society*, vol. 122, no. 17, pp. 4177–4184, 2000.

[42] M. Kulkarni, A. Mazare, J. Park et al., "Protein interactions with layers of TiO 2 nanotube and nanopore arrays: morphology and surface charge influence," *Acta Biomaterialia*, vol. 45, pp. 357–366, 2016.

[43] W. Yang, X. Xi, X. Shen, P. Liu, Y. Hu, and K. Cai, "Titania nanotubes dimensions-dependent protein adsorption and its effect on the growth of osteoblasts," *Journal of Biomedical Materials Research Part A*, vol. 102, no. 10, pp. 3598–3608, 2013.

[44] S. Minagar, J. Wang, C. C. Berndt, E. P. Ivanova, and C. Wen, "Cell response of anodized nanotubes on titanium and titanium alloys," *Journal of Biomedical Materials Research Part A*, vol. 101, no. 9, pp. 2726–2739, 2013.

[45] L. Zhao, L. Liu, Z. Wu, Y. Zhang, and P. K. Chu, "Effects of micropitted/nanotubular titania topographies on bone mesenchymal stem cell osteogenic differentiation," *Biomaterials*, vol. 33, no. 9, pp. 2629–2641, 2012.

[46] L. M. Bjursten, L. Rasmusson, S. Oh, G. C. Smith, K. S. Brammer, and S. Jin, "Titanium dioxide nanotubes enhance bone bonding in-vivo," *Journal of Biomedical Materials Research Part A*, vol. 9999, pp. 1218–1224, 2010.

[47] N. Wang, H. Li, W. Lü et al., "Effects of TiO$_2$ nanotubes with different diameters on gene expression and osseointegration of implants in minipigs," *Biomaterials*, vol. 32, no. 29, pp. 6900–6911, 2011.

[48] C. Yao, E. B. Slamovich, and T. J. Webster, "Enhanced osteoblast functions on anodized titanium with nanotube-like structures," *Journal of Biomedical Materials Research Part A*, vol. 85, no. 1, pp. 157–166, 2008.

[49] J. Park, S. Bauer, K. A. Schlegel, F. W. Neukam, K. von der Mark, and P. Schmuki, "TiO$_2$ nanotube surfaces: 15 nm-an optimal length scale of surface topography for cell adhesion and differentiation," *Small*, vol. 5, no. 6, pp. 666–671, 2009.

[50] S. Bauer, J. Park, J. Faltenbacher, S. Berger, K. von der Mark, and P. Schmuki, "Size selective behavior of mesenchymal stem cells on ZrO$_2$ and TiO$_2$ nanotube arrays," *Integrative Biology*, vol. 1, no. 8-9, pp. 525–532, 2009.

[51] J. Park, S. Bauer, K. von der Mark, and P. Schmuki, "Nanosize and vitality: TiO$_2$ nanotube diameter directs cell fate," *Nano Letters*, vol. 7, no. 6, pp. 1686–1691, 2007.

[52] M. J. Dalby, N. Gadegaard, and R. O. C. Oreffo, "Harnessing nanotopography and integrin-matrix interactions to influence stem cell fate," *Nature Materials*, vol. 13, no. 6, pp. 558–569, 2014.

[53] C. Huang, X. Liu, Y. Liu, and Y. Wang, "Room temperature ferromagnetism of Co-doped TiO$_2$ nanotube arrays prepared by sol-gel template synthesis," *Chemical Physics Letters*, vol. 432, no. 4–6, pp. 468–472, 2006.

[54] J. Qiu, Z. Jin, Z. Liu et al., "Fabrication of TiO$_2$ nanotube film by well-aligned ZnO nanorod array film and sol-gel process," *Thin Solid Films*, vol. 515, no. 5, pp. 2897–2902, 2007.

[55] T. Maiyalagan, B. Viswanathan, and U. V. Varadaraju, "Fabrication and characterization of uniform TiO$_2$ nanotube arrays by sol-gel template method," *Bulletin of Materials Science*, vol. 29, pp. 705–708, 2006.

[56] S. M. Liu, L. M. Gan, L. H. Liu, W. D. Zhang, and H. C. Zeng, "Synthesis of single-crystalline TiO$_2$ nanotubes," *Chemistry of Materials*, vol. 14, no. 3, pp. 1391–1397, 2002.

[57] C.-C. Wang and J. Y. Ying, "Sol–Gel synthesis and hydrothermal processing of anatase and rutile titania nanocrystals," *Chemistry of Materials*, vol. 11, no. 11, pp. 3113–3120, 1999.

[58] Z. Miao, D. Xu, J. Ouyang, G. Guo, X. Zhao, and Y. Tang, "Electrochemically induced Sol–Gel preparation of single-crystalline TiO_2 nanowires," *Nano Letters*, vol. 2, no. 7, pp. 717–720, 2002.

[59] S. D. Perera, R. G. Mariano, K. Vu et al., "Hydrothermal synthesis of graphene-TiO_2 nanotube composites with enhanced photocatalytic activity," *ACS Catalysis*, vol. 2, no. 6, pp. 949–956, 2012.

[60] M. G. Choi, Y.-G. Lee, S.-W. Song, and K. M. Kim, "Lithium-ion battery anode properties of TiO_2 nanotubes prepared by the hydrothermal synthesis of mixed (anatase and rutile) particles," *Electrochimica Acta*, vol. 55, no. 20, pp. 5975–5983, 2010.

[61] Y.-K. Zhou, L. Cao, F.-B. Zhang, B.-l. He, and H.-L. Li, "Lithium insertion into TiO[sub 2] nanotube prepared by the hydrothermal process," *Journal of Electrochemical Society*, vol. 150, no. 9, article A1246, 2003.

[62] D. V. Bavykin, V. N. Parmon, A. A. Lapkin, and F. C. Walsh, "The effect of hydrothermal conditions on the mesoporous structure of TiO_2 nanotubes," *Journal of Materials Chemistry*, vol. 14, no. 22, p. 3370, 2004.

[63] Q. Zhang, L. Gao, J. Sun, and S. Zheng, "Preparation of long TiO_2 nanotubes from ultrafine rutile nanocrystals," *Chemistry Letters*, vol. 31, no. 2, pp. 226-227, 2002.

[64] H. Ou and S. Lo, "Review of titania nanotubes synthesized via the hydrothermal treatment: fabrication, modification, and application," *Separation and Purification Technology*, vol. 58, no. 1, pp. 179–191, 2007.

[65] J.-Y. Huang, K.-Q. Zhang, and Y.-K. Lai, "Fabrication, modification, and emerging applications of TiO_2 nanotube arrays by electrochemical synthesis: a review," *International Journal of Photoenergy*, vol. 2013, Article ID 761971, 19 pages, 2013.

[66] E. Matykina, A. Conde, J. de Damborenea, D. M. Y. Marero, and M. A. Arenas, "Growth of TiO_2-based nanotubes on Ti-6Al-4V alloy," *Electrochimica Acta*, vol. 56, no. 25, pp. 9209–9218, 2011.

[67] D. Losic and S. Simovic, "Self-ordered nanopore and nanotube platforms for drug delivery applications," *Expert Opinion on Drug Delivery*, vol. 6, no. 12, pp. 1363–1381, 2009.

[68] Y. R. Smith, R. S. Ray, K. Carlson, B. Sarma, and M. Misra, "Self-ordered titanium dioxide nanotube arrays: anodic synthesis and their photo/electro-catalytic applications," *Materials*, vol. 6, no. 7, pp. 2892–2957, 2013.

[69] V. S. Saji, H. C. Choe, and W. A. Brantley, "An electrochemical study on self-ordered nanoporous and nanotubular oxide on Ti-35Nb-5Ta-7Zr alloy for biomedical applications," *Acta Biomaterialia*, vol. 5, no. 6, pp. 2303–2310, 2009.

[70] M. F. Hossain, R. S. Mandal, M. R. Haque, and M. S. Islam, "Fabrication of TiO_2 nanotube arrays in room temperature by anode oxidation method," in *Proceedings of 2012 7th International Conference on Electrical and Computer Engineering*, pp. 94–97, Dhaka, India, December 2012.

[71] K. Subramani, "Titanium surface modification techniques for implant fabrication - from microscale to the nanoscale," *Journal of Biomimetics, Biomaterials and Tissue Engineering*, vol. 5, pp. 39–56, 2010.

[72] N. Swami, Z. Cui, and L. S. Nair, "Titania nanotubes: novel nanostructures for improved osseointegration," *Journal of Heat Transfer*, vol. 133, no. 3, article 034002, 2011.

[73] X. Zhu, J. Chen, L. Scheideler, R. Reichl, and J. G. Gerstorfer, "Effects of topography and composition of titanium surface oxides on osteoblast responses," *Biomaterials*, vol. 25, no. 18, pp. 4087–4103, 2004.

[74] A. Mazzarolo, M. Curioni, A. Vicenzo, P. Skeldon, and G. E. Thompson, "Anodic growth of titanium oxide: electrochemical behaviour and morphological evolution," *Electrochimica Acta*, vol. 75, pp. 288–295, 2012.

[75] A. Ghicov, H. Tsuchiya, J. M. Macak, and P. Schmuki, "Titanium oxide nanotubes prepared in phosphate electrolytes," *Electrochemistry Communications*, vol. 7, no. 5, pp. 505–509, 2005.

[76] J. M. Macak and P. Schmuki, "Anodic growth of self-organized anodic TiO_2 nanotubes in viscous electrolytes," *Electrochimica Acta*, vol. 52, no. 3, pp. 1258–1264, 2006.

[77] A. Valota, D. J. LeClere, P. Skeldon et al., "Influence of water content on nanotubular anodic titania formed in fluoride/glycerol electrolytes," *Electrochimica Acta*, vol. 54, no. 18, pp. 4321–4327, 2009.

[78] G. D. Sulka, J. Kapusta-Kołodziej, A. Brzózka, and M. Jaskuła, "Fabrication of nanoporous TiO_2 by electrochemical anodization," *Electrochimica Acta*, vol. 55, no. 14, pp. 4359–4367, 2010.

[79] Z. Bolukoglu, I. Karakaya, and M. Erdogan, "Formation of titanium dioxide nanotube arrays by anodizing Ti-6Al-4V alloy," *ECS Transactions*, vol. 58, pp. 45–52, 2014.

[80] S. Bauer, S. Kleber, and P. Schmuki, "TiO_2 nanotubes: tailoring the geometry in H_3PO_4/HF electrolytes," *Electrochemistry Communications*, vol. 8, no. 8, pp. 1321–1325, 2006.

[81] K. Indira, U. K. Mudali, T. Nishimura, and N. Rajendran, "A review on TiO_2 nanotubes: influence of anodization parameters, formation mechanism, properties, corrosion behavior, and biomedical applications," *Journal of Bio- and Tribo-Corrosion*, vol. 1, no. 4, 2015.

[82] S. Goodarzi, F. Moztarzadeh, N. Nezafati, and H. Omidvar, "Titanium dioxide nanotube arrays: a novel approach into periodontal tissue regeneration on the surface of titanium implants," *Advanced Materials Letters*, vol. 7, no. 3, pp. 209–215, 2016.

[83] B. Chen, "Growth of anodic alumina nanopores and titania nanotubes and their applications," Doctoral Dissertation, Virginia Polytechnic Institute and State University, Blacksburg, VA, USA, 2013.

[84] A. Jaroenworaluck, D. Regonini, C. R. Bowen, R. Stevens, and D. Allsopp, "Macro, micro and nanostructure of TiO_2 anodised films prepared in a fluorine-containing electrolyte," *Journal of Materials Science*, vol. 42, no. 16, pp. 6729–6734, 2007.

[85] U. Donatus, G. E. Thompson, D. Elabar, T. Hashimoto, and S. Morsch, "Features in aluminium alloy grains and their effects on anodizing and corrosion," *Surface and Coatings Technology*, vol. 277, pp. 91–98, 2015.

[86] A. Atyaoui, H. Cachet, E. M. M. Sutter, and L. Bousselmi, "Effect of the anodization voltage on the dimensions and photoactivity of titania nanotubes arrays," *Surface and Interface Analysis*, vol. 45, no. 11-12, pp. 1751–1759, 2013.

[87] S. A. Ali Yahia, L. Hamadou, A. Kadri, N. Benbrahim, and E. M. M. Sutter, "Effect of anodizing potential on the formation and EIS characteristics of TiO_2 nanotube arrays," *Journal of Electrochemical Society*, vol. 159, no. 4, pp. 83–92, 2012.

[88] Y. Sun and K.-P. Yan, "Effect of anodization voltage on performance of TiO_2 nanotube arrays for hydrogen generation in a two-compartment photoelectrochemical cell," *International Journal of Hydrogen Energy*, vol. 39, no. 22, pp. 11368–11375, 2014.

[89] P. W. Doll, M. Wolf, M. Weichert, R. Ahrens, A. E. Guber, and B. Spindler, "Nanostructuring of titanium by anodic oxidation

with sulfuric and hydrofluoric acid," *Current Directions in Biomedical Engineering*, vol. 4, no. 1, pp. 641–644, 2018.

[90] T. D. Dikova, M. G. Hahm, D. P. Hashim, N. T. Narayanan, R. Vajtai, and P. M. Ajayan, "Mechanism of TiO$_2$ nanotubes formation on the surface of pure Ti and Ti-6Al-4V alloy," *Advanced Materials Research*, vol. 939, pp. 655–662, 2014.

[91] T. D. Dikova, M. G. Hahm, D. P. Hashim, T. N. Narayanan, R. Vajtai, and P. M. Ajayan, "Growth mechanism of TiO$_2$ nanotubes on the Ti-6Al-4V surface," in *Proceedings of IX International Congress "Machines, Technologies, Materials"*, Varna, Bulgaria, September 2012.

[92] A. Kaczmarek-Pawelska and E. Krasicka-Cydzik, "Morphological and chemical relationships in nanotubes formed by anodizing of Ti6Al4V alloy," *De Gruyter*, vol. 14, no. 4, pp. 12–20, 2014.

[93] P. Xiao, B. B. Garcia, Q. Guo, D. Liu, and G. Cao, "TiO$_2$ nanotube arrays fabricated by anodization in different electrolytes for biosensing," *Electrochem. commun.*vol. 9, no. 9, pp. 2441–2447, 2007.

[94] G. K. Mor, O. K. Varghese, M. Paulose, K. Shankar, and C. A. Grimes, "A review on highly ordered, vertically oriented TiO$_2$ nanotube arrays: fabrication, material properties, and solar energy applications," *Solar Energy Materials and Solar Cells*, vol. 90, no. 14, pp. 2011–2075, 2006.

Research Article

Tunable Piezophotonic Effect on Core-Shell Nanoparticles Prepared by Laser Ablation in Liquids under External Voltage

A. K. Kodeary[1,2] **and S. M. Hamidi** (iD) [1]

[1]*Magneto-plasmonic Lab, Laser and Plasma Research Institute, Shahid Beheshti University, Tehran, Iran*
[2]*Department of Laser Physics, College of Science, University of Babylon, Babylon, Iraq*

Correspondence should be addressed to S. M. Hamidi; m_hamidi@sbu.ac.ir

We report an experimental study on the piezophotonic effect of gold and lead zirconate titanate ($PbZrTiO_3$) nanoparticles (NPs) and also their core-shell nanostructures prepared by the laser ablation in liquid method. To obtain these NPs and composite materials, the targets were immersed in deionized water and a polymeric solution of polyvinyl pyrrolidone (PVP) under Nd:YAG laser pulses irradiation. Linear and nonlinear properties of these NPs were studied by optical spectroscopy and the Z-scan technique. Furthermore, tunable nonlinear properties of the NPs were measured under an external electric field under illumination to investigate the piezophotonic effect. Our results show that, at the interface of PZT and Au, due to the Schottky barrier, we have electron/hole recombination prevention, which leads to efficient enhancement in the nonlinear properties.

1. Introduction

The piezophotonic effect, which can be viewed as a two-way coupling impact among piezoelectricity and photoexcitation properties [1, 2], the conjugation of excitation by photons, piezoelectricity, and semiconductor properties (piezophototronic effect) of ZnO nanomaterials, was investigated by Wang et al. [1–4]. Their examination exhibited that the properties of the noncentro symmetry semiconductors could be tuned under piezoelectric fields. As a result of these findings, the materials received much attention in the electronic or photonic communities [5–7].

These materials are introduced as nanogenerators [8], high-power generators [9], electromechanical sensors [10], actuators [11], and energy converters [12] based on the coupling of piezoelectric and semiconducting properties. To achieve these applications, one of the most important arms is the material with the best piezoelectric effect such as PbZrTiO3 (PZT), which has low coercion, has large polarization, and acts as a high-Curie temperature electric insulator [13].

To get above-mentioned applications from these materials, they are a lot of reports in the bulk, thin film, or single nanoparticels of PZT structures [14]. After that, to get more efficiency, composite, sandwich, or heterogeneous structures of these materials have been proposed. Consequently, the terminology "core/shell" of the semiconductor and metal was adopted to obtain the properties which arise from them, which are not the mix of individual properties, and also to obtain some tunable and synergetic properties emerging from the activity between metal and semiconductor components [15–17].

One may know that the materials made of noble-metal nanoparticles show efficient resonance due to the collective oscillation of electrons, named the surface plasmon resonance (SPR) phenomenon. This resonance in different propagative or localized forms can be used for amplification of the electric field in the vicinity of any other materials. The improvement of the local electric field is responsible for the amplification of the linear and also nonlinear properties [18–23].

According to the abovementioned properties, the semiconductor/metal interface can be used for controlling

the optical properties of nanostructures by external or internal parameters such as electric or magnetic field and size of the core or shell part, respectively. These optical properties can be classified into two main parts: linear and nonlinear. For the linear part, there are a lot of papers which focus on the SPR wavelength and also the Fermi level or Fermi pinning in the interface of them and so on [9]. For the nonlinear part, there are few works which focus on the change in the nonlinear properties of bare core-shell nanostructures by using the Z-scan approach, which is an outstanding and generally used procedure to characterize the nonlinear optical properties of materials [24, 25].

On the other hand, tuning and adjusting the optical and piezophotonic properties of nanostructures based on understanding of interfacial phenomena is a very important topic in the field of NPs. Until now, there is not any investigation about the linear and nonlinear properties under external electric and optical fields. In this study, we prepared Au, PZT, and Au@PZT and PZT@Au core/shell NPs by the laser ablation in liquids (LAL) method because of the various advantages of this technique, for example, simplicity of the experimental setup, low cost, and environmental friendly. This technique has become a promising method for the synthesis of NP systems such as single or core shell in liquid solutions [19, 26, 27]. This work focuses on the exact calculation of the effect of external electric field on the nonlinear refractive index, which was calculated by the closed-aperture z-scan technique to show the piezophotonic effect on samples. In addition, because the ferroelectric materials are sensitive to the external electric field, we use them in a transparent dielectric matrix under two internal (the local fields experienced around metal NPs) and external electric fields.

2. Theory

Nanomaterials with large third-order optical nonlinearities have recently become the important topic for researchers and are of wide scientific interest, mostly because of their possible application in rapid optical switching devices, which are becoming more and more important and are more commonly used [28]. The nonlinearities of the third order are usually studied in centrosymmetric media, in which the second-order nonlinear susceptibility is zero [29].

In a linear dielectric medium, there is a linear relation arising from interaction between the induced electric polarization and the electric field for light as follows:

$$p = \varepsilon_{o}\chi \cdot E, \tag{1}$$

where ε_{o} is the permittivity of vacuum and χ is the dielectric susceptibility of the medium.

The polarization P is a product of the individual dipole moment p, which is induced by the applied electric field E, and the number density of dipole moments. This relation between p and E becomes nonlinear as E enhanced enough high values. External electric fields are almost always smaller than the characteristic interatomic fields, even when laser beams are used, which means that the nonlinearity is usually weak [28, 29]. This is the basic representation for a nonlinear optical

medium. By this fact and the combination with Maxwell's equations, the refractive index, $n = n_{o} + n_{2}I$, and the optical absorption, $\alpha = \alpha_{o} + \beta I$, can be represented as functions of the intensity I of the incident laser beam [30]. This nonlinear part of the refractive index can be written as follows:

$$n_{2} = \frac{\Delta\Phi^{o}}{k * I_{o} * L_{eff}}, \tag{2}$$

where I_{o} indicates the intensity of the incident beam at the focal point as a function of the intensity of the laser, I, $I_{o} = I/\pi(w_{o})^{2}$ and

$$\Delta T = 0.406\,(1 - S)^{0.25}\,\Delta\Phi^{o}, \tag{3}$$

where

$$\begin{aligned}\Delta\Phi^{o} &\leq \pi, \\ \Delta T &= T_{peak} - T_{valley},\end{aligned} \tag{4}$$

where T_{peak} and T_{valley} are the maximum and minimum values of transmittance for closed-aperture Z-scan technique, respectively, $\Delta\Phi^{o}$ is the nonlinear phase shift, and S is the aperture's linear transmittance [30–32]. Also, L_{eff} is the effective length of the material as a function of the sample length, L, and linear absorption coefficient, α_{o}, given as [28–34]

$$L_{eff} = \frac{[1 - \exp{(-\alpha_{o}L)}]}{\alpha_{o}}, \tag{5}$$

where L is the sample length and α_{o} is the linear absorption coefficient [28–34].

3. Experimental Method

The schematic diagram of the experimental setup is described in Figure 1 which shows the nanoparticle generation setup by the laser ablation in liquid method. Experiments were carried out by using Q-switched Nd:YAG lasers, operating at a wavelength of 1064 nm, pulse width of (5 ns), and repetition rate of (10 Hz), and 100 mJ energy per pulse was focused on the samples.

The laser beam was directed on the pure (99.9%) gold with a thickness of 1 mm and the PZT alloy with a thickness of 2 mm, which were used as the target and immersed in liquid for comparison (deionized water and polyvinyl pyrrolidone (PVP), a polymer with a mixture of 1% PVP and deionized water dissolved using a magnetic stirrer). In order to obtain more stable solution, in the container, we use a glass vessel under a high-reflectivity mirror and a lens with 150 mm focal length. The water was kept at the height above the target at 10 mm, and a quartz cover was used to avoid the splashing to the surroundings of the vessel.

The distance between the lens and the target was adjusted to obtain a best spot of laser beam focused on the target. For the preparation of bimetallic Au@PZT and PZT@Au core-shell NPs, a sequential two-step ablation method, shown schematically in Figure 2, was used. In this method, first Au NP colloidal solution was prepared by laser ablation of Au target in deionized water environment . Once, in a PVP again, irradiation of target endured for 3 min and was accompanied
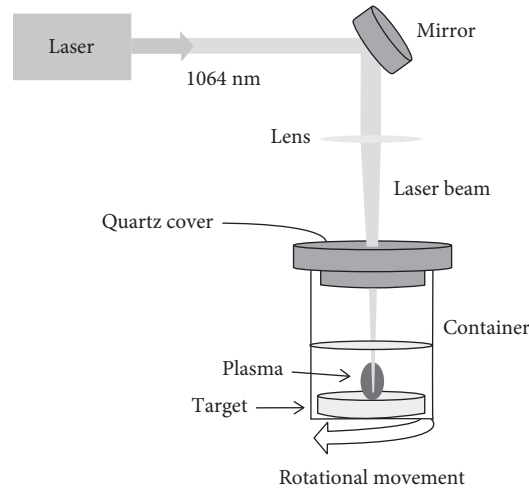
FIGURE 1: Schematic diagram of the experimental setup used in nanoparticles preparation by laser ablation confined in a liquid medium.
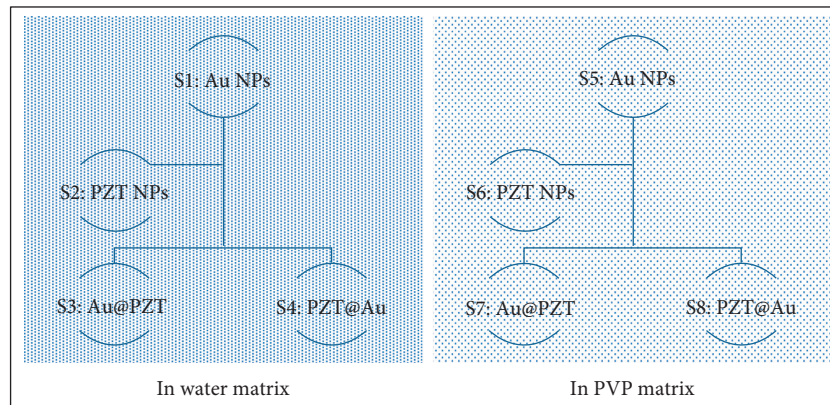

FIGURE 2: The steps to prepare the core-shell nanoparticles for samples.

by a homogeneous liquid staining by pink color because of the plasmon resonance band of Au NPs in the visible region. During illumination by laser pulses, color change of the colloid was observed, and this process continued till the color of colloid became red, followed by ablation of the PZT target in the previously prepared Au NPs colloidal solution. The PZT NPs act as shell and form core for ablated hot Au species. The ablation duration was 2-3 min for PZT to obtain core-shell morphology with varying shell thickness. After preparation, all of the samples were stirred in an ultrasonic bath at room temperature (RT) for about 15 min.

In order to study the effects of an external electric field on the nonlinear refractive index of the NP samples, we employed the closed-aperture Z-scan technique, and measurements have been performed at $\lambda = 532$ nm, which is close to the SPR absorption band of the materials, using a CW diode-pumped solid-state laser as the light source.

The laser beam gave a Gaussian profile by vertical polarization and a power of 120 mW at normal incidence geometry. The sample was moved forward and backward along the Z-axis around the beam waist of the laser during the measurement, under the effect of an external electric field (used variable voltages (0–7 volt)), to analyze the nonlinear variation of the refractive index. The schematic of the setup for the Z-scan experiment is shown in Figure 3.

4. Results and Discussion

Optical absorption spectra of prepared NPs and core/shell samples were measured using a UV–visible spectrophotometer. The behavior is shown in Figure 4.

Figure 4(a) shows the UV-visible absorption of the products S1 to S4 NPs and core/shell samples in deionized water solution, and the UV-visible absorption of the products S5 to S8 NPs and core/shell samples in PVP solution is illustrated in Figure 4(b). These figures show that each sample has a surface plasmon resonance (SPR) absorption spectrum as indicated by their NPs sizes. The measured SPR peak of these samples indicates that the resonance peak become stronger in PVP solution because the matrix is more stable. Movability of the SPR wavelength of the samples occurs as shown in Table 1.

This red shift was because of the larger refractive index of core-shell structure when compared with PZT and Au NPs.
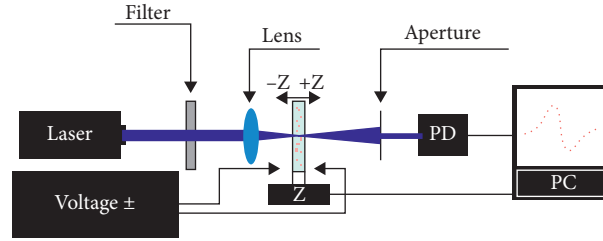
FIGURE 3: Schematic drawing of the experimental arrangement for closed-aperture Z-scan technique.
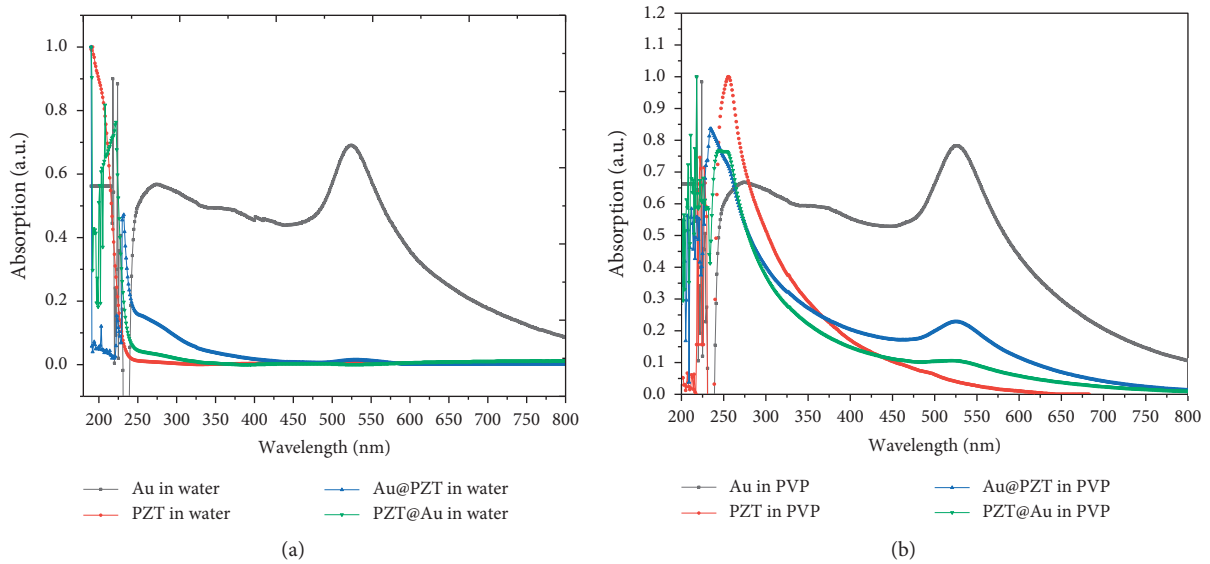

FIGURE 4: Absorption spectra of core-shell NPs: (a) in water solvent and (b) in PVP solvent.

Furthermore, the SPR depends unequivocally on the NPs shape and the size of the nanoparticles and also is sensitive to the refractive index of the surrounding medium due to the difference in shell thicknesses [9, 17, 35, 36].

Also, morphology of the samples was investigated by the use of a field emission scanning electron microscopy (FESEM) model (JSM-7610F), operating at an accelerating voltage of (10 kV), to identify and determine the shape and size of the produced particles. The formation of a metallic phase core/shell made up of particles of quasi-spherical morphology with a size range for core from 50 nm to 90 nm and shell from 20 nm to 34 nm for Au@PZT in water, and the sizes starting to increase to more than 100 nm for PZT@Au in the polymeric solution can be seen from Figure 5. It can be seen that there were no agglomeration effects present when the ablation was performed directly in the polymeric solution.

We realize that the dielectric properties of the material are extremely important and play the main role in the position and intensity of the peak of SPR of NPs. As we expected, coupling between the metallic and piezoelectric medium yields to the change in the refractive index of the samples.

These properties have been characterized by relation between $\varepsilon_1 = n^2 - k^2$ and $\varepsilon_2 = 2nK$ as shown in Figure 6, for

TABLE 1: SPR in different solutions for all samples.

Samples	SPR in water matrix	SPR in PVP matrix
Au NPs	524 nm	526 nm
PZT NPs	202 nm	255 nm
Au@PZT	529@231 nm	527@235 nm
PZT@Au	222@526 nm	246@529 nm

samples in deionized water and Figure 7, for samples in the polymeric solution.

It is evident from these figures that when Au NPs are ablated in water matrix, we have the main resonance peak in the refractive index as clarified by the absorption spectrum. But, when NPs are prepared in the PVP matrix, we can see slight change in the imaginary part of the refractive index in spite of decrease in the real part of the refractive index. This change can be described by the fact that we have PVP supporting larger gold NPs which is confirmed by FESEM image. This is clarified when we compare Au@PZT NPs in water matrix with those NPs in PVP (Figures 6(c) and 7(c)), in which we can see two distinct peaks in the PVP matrix in both real and imaginary parts of the refractive indices.

Measurements of the nonlinear refractive index in NPs and core/shell samples are revealed by using the Z-scan
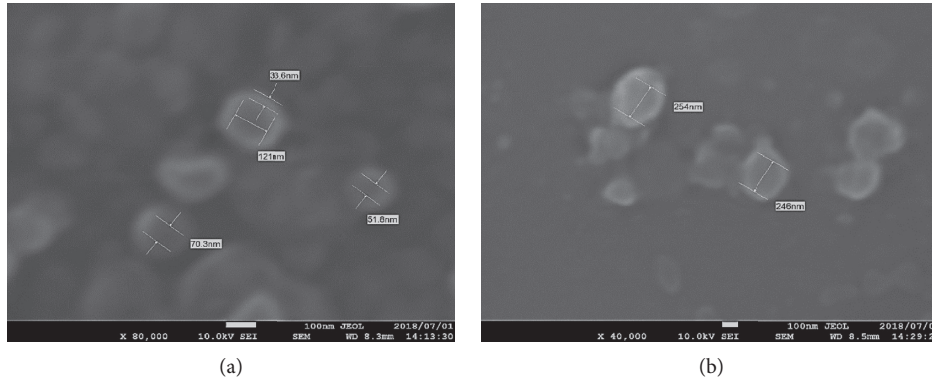
(a)

(b)

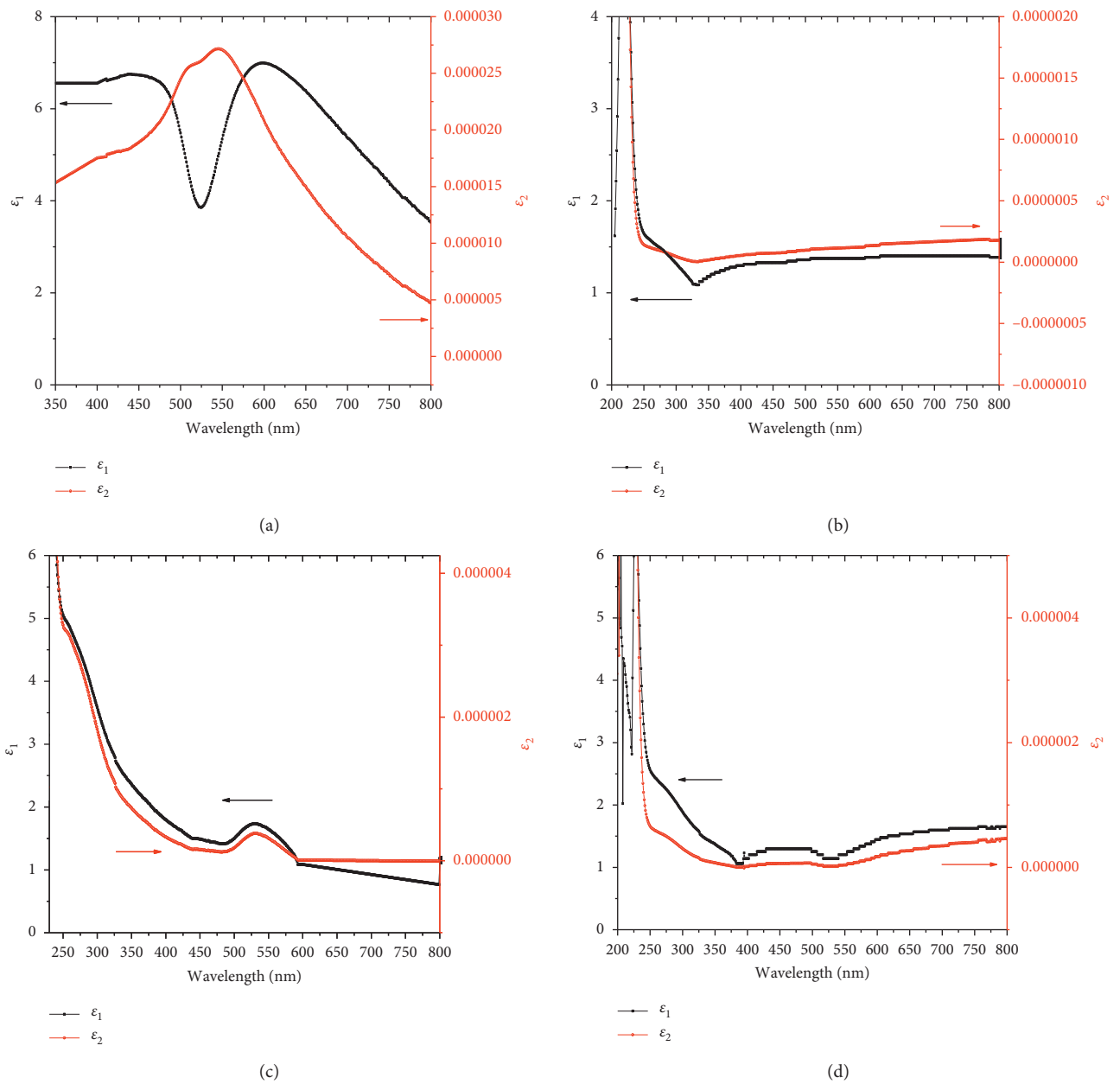FIGURE 5: FESEM image of (a) Au@PZT in water and (b) PZT@Au in PVP.

(a)

(b)

(c)

(d)

FIGURE 6: The relationship between ε_1 and ε_2 with wavelength in the water matrix.
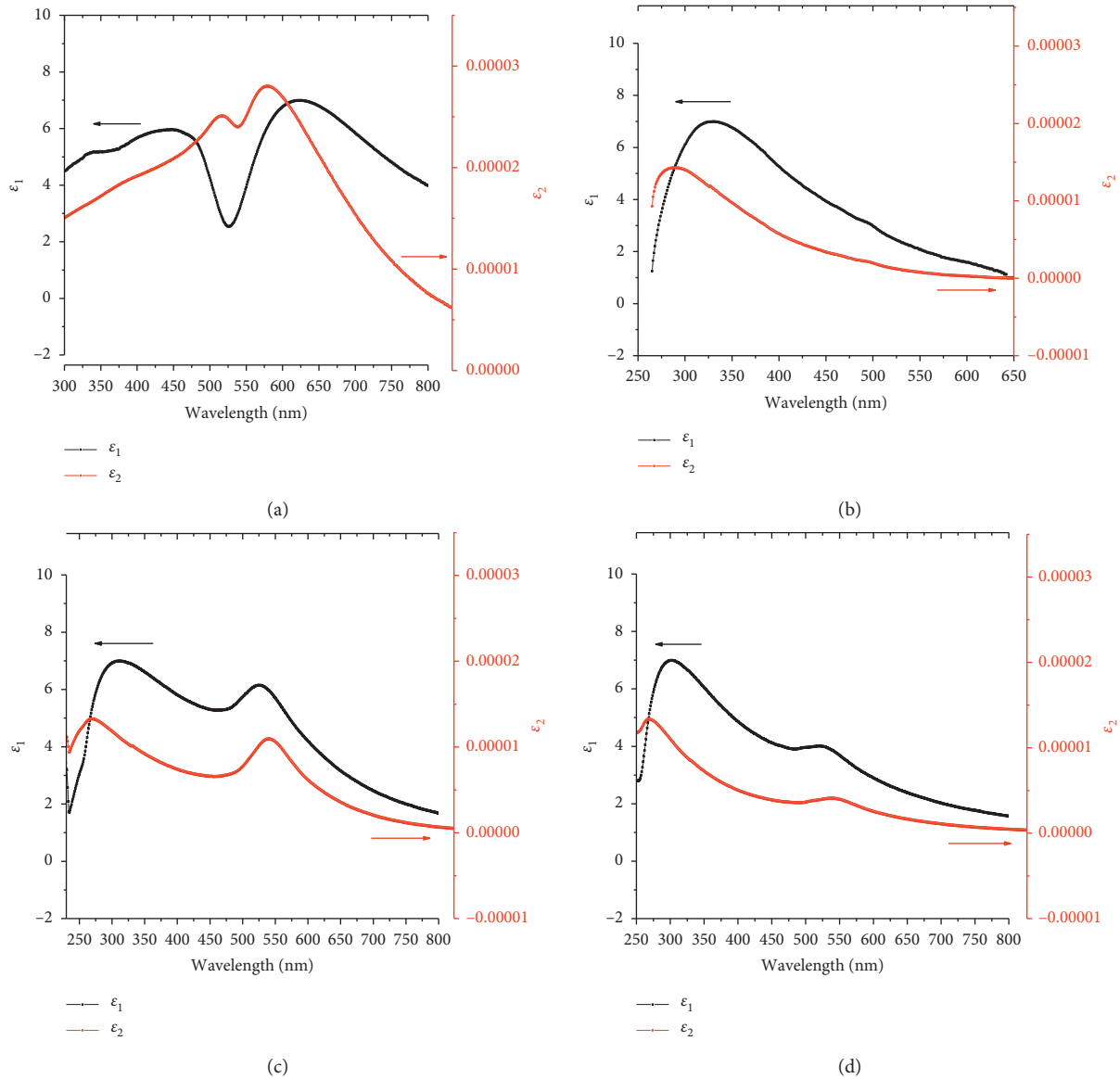
FIGURE 7: The relationship between ε_1 and ε_2 with wavelength in the PVP matrix.

technique. The scan started from a distance near the focus to check the fact that the generating samples in a PVP polymer solution have a nonlinear refractive index value greater than that generated in deionized water. It can be seen that the peak-valley pattern of the normalized transmittance curve indicates the positive sign for samples produced in the water solution, except Au NPs. This is different from negative sign, in which the valley comes after the transmittance peak, indicating the self-defocusing phenomena in all applied voltages. Furthermore, the valley-peak configuration indicates the negative sign for samples produced in the PVP solution except Au@PZT NPs, as shown in Figure 8.

One may know that the SPR wavelength in the nanocomposite materials can be actively modulated at regular intervals through the application of external parameters such as electric field. The effect of the external electric field on the nonlinear refractive index was studied with a direct

variable voltage (0–7 volt) effect on the sample inside the cell during scanning using the Z-scan technique. We observed that an increase in the amount of voltage leads to increasing distance between the peak-valley transmittance (i.e., the difference of the normalized transmission between the peak and the valley). This means there is an increase in the quantity of nonlinear refractive index of all samples, as shown in Figure 9.

Figure 10 indicates that we have an increase in the amount of nonlinear refractive index in the nanoparticles in the polymer solution as compared to the water solution. Also, we have a clear increase in this amount when an external electric field is affected. This is an important result in the study of the effects on optical and electronic properties of devices.

A comparison of all samples with some plots was drawn, as shown in Figure 11, and we conclude that there are
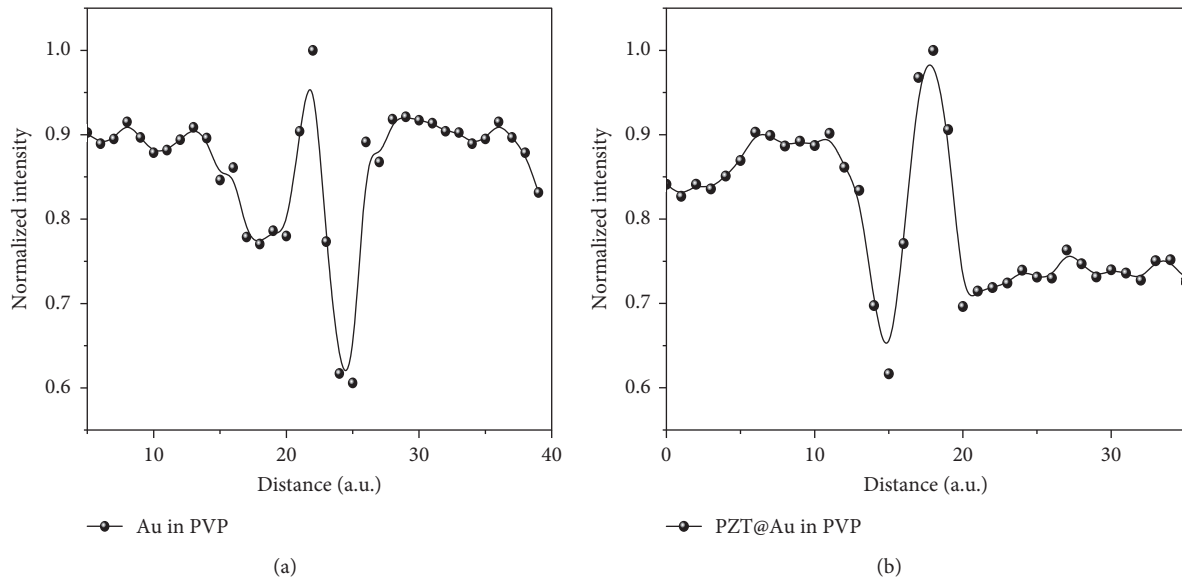
FIGURE 8: Transmittance with closed-aperture Z-scan of Au NPs and PZT@Au core-shell NPs in PVP solution.
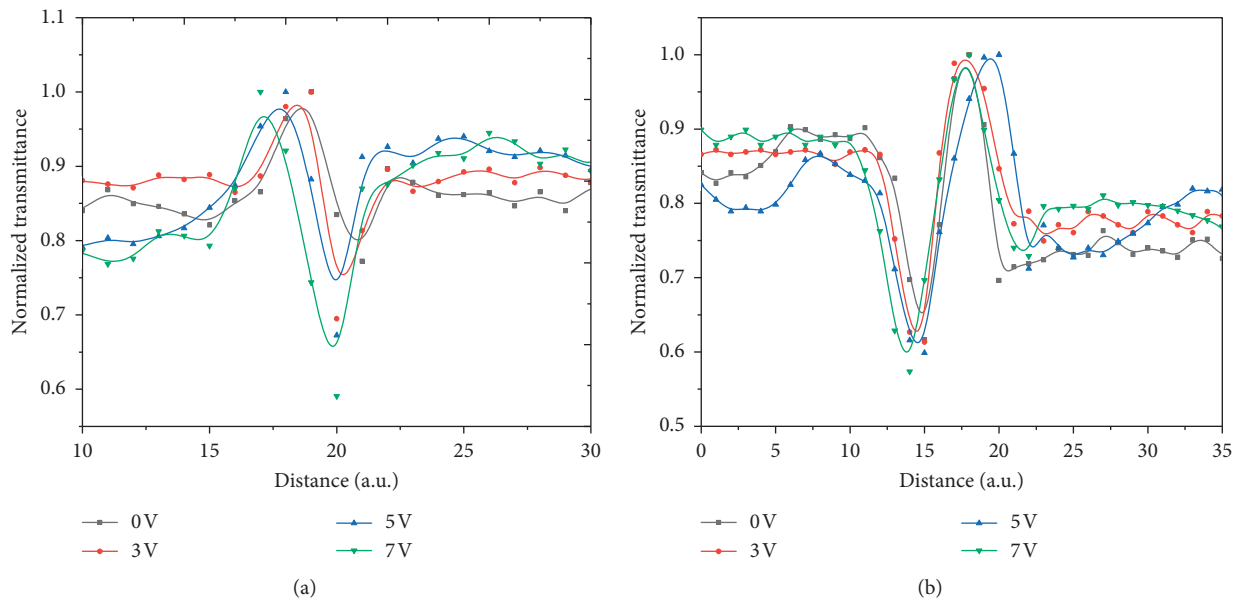
FIGURE 9: Transmittance with closed-aperture Z-scan of the effects of the external electric field.

samples in which the nonlinear refractive index changes slightly, while other samples have a significant change in their magnitude. These changes depend on the boundary conditions between the core and the shell of the samples.

Our results show significant adjustability for the nonlinear refractive index for each set of NPs. When an electric field was applied (0–7 volt) to the NP samples, the enhancement can be seen for the nonlinear refractive index with rate 48% for metal NPs, while the proportion of improvement did not exceed 10% for the core/shell NPs.

There are various physical mechanisms that result in the nonlinear change of incorporate refractive index,

electrostriction, electronic polarization, photorefractive effect, ultrafast electronic effects [30], and thermal effect [31], as the molecular reorientation collectively contributes to nonlinear change of indices [25, 37–39].

Our results show that the changes of the nonlinear indices are drastically because of the reorientation procedure of the induced polarization of the core/shell NPs and the electric field of the laser beam as changes are increased with increased applied voltage on core/shell NPs. Thermal effects can considerably contribute to the nonlinear refractive index under a CW laser for sample illumination which can occur because of thermal effects [40, 41]. In addition, we expect

(a)

(b)

(c)

(d)

FIGURE 10: Change in the nonlinear refractive index by changing solution and voltages for all samples.

that thermal effect has more impact than the other effects. This result agrees with [32].
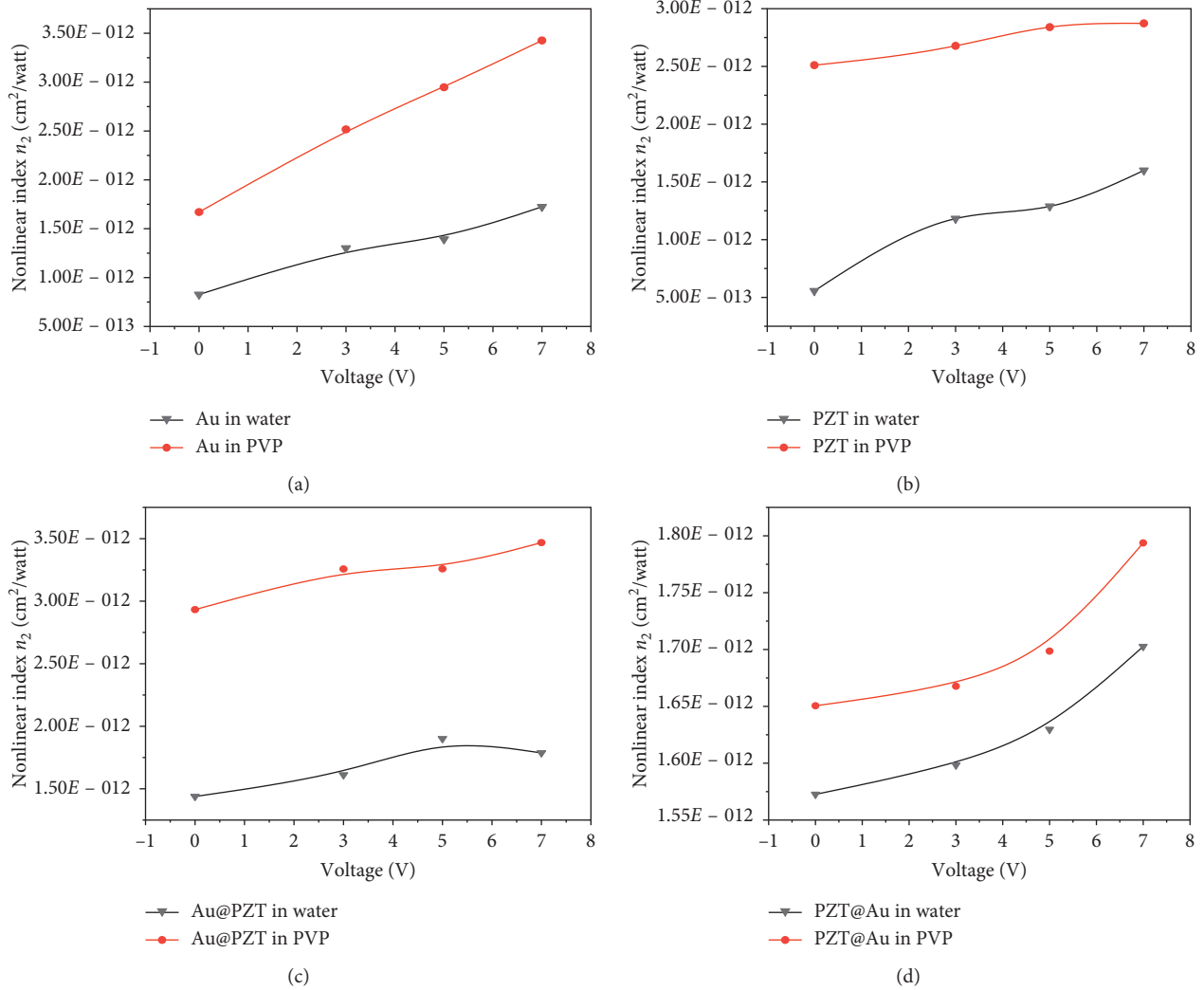
To get more sense about this manner, we use the energy diagram of the core and shell and investigate the interface physical phenomena such as Schottky barrier heights which are very important at the metal/semiconductor interfaces.

It, to a great extent, defines the current transport and the potential distribution through these interfaces and, consequently, the usefulness of the electronic devices [13]. The energy band diagrams of the PZT@ Au core@ shell NPs interfaces are shown in Figure 12. The vacuum levels derived from the work functions for typical PZT and metal Au are about 5.8 and 5.1 eV, respectively, with an ionization potential of PZT of 6.8 eV [13, 42]. The possible band bowing in the PZT substrate is not shown in the graphs.

The electron affinity $\chi = 3.4$ eV of the cleaned PZT thin films is derived from the XPS measurement, and an energy gap of 3.4 eV is considered from Reference [13]. By considering the Schottky barrier heights for electrons at the interfaces and taking work function of 5.1 eV for Au into account, the dipole potential δ can be derived from the discontinuity of the vacuum level E_{VAC} at the interface.

Here, E_{CB}, E_{F}, and E_{VB} are the conduction band, Fermi level, and valence band of PZT, respectively. The Fermi-level position at the PZT/Au interface has been determined utilizing a combination of metal work function and PZT electron affinity, $E_{\text{F}} - E_{\text{VB}} = 1.8$ eV, by the barriers for the injections of electrons ($\Phi_{\text{Bn}} = E_{\text{CB}} - E_{\text{F}}$) and holes ($\Phi_{\text{Bp}} = E_{\text{F}} - E_{\text{VB}}$) [13, 42]. Irradiating with the visible light, within the energy gap of semiconductors, such as the laser light of 532 nm, leads to absorption of photons and generates an electric field at the Schottky barrier which forces the photogenerated e^- and h^+ to isolate in opposite directions. When the PZT@Au NPs are irradiated with light, the e^- in the valence band of PZT comes to be excited to the conduction band. Since the EF of PZT@Au is at a lower level than the PZT conduction band, the Au interbands capture e^- from PZT. Thus, the Au layer acts as the reservoir for the e^- and prevents the fast recombination of photo-excited e^- and h^+ in the semiconductor [42, 43]. This leads to increases in the absorption coefficient and thus nonlinear refractive index in the SPR sample quantities. This work will give some idea to those interested in scientific research for more advancement of piezophotonic effects in the optical drives.
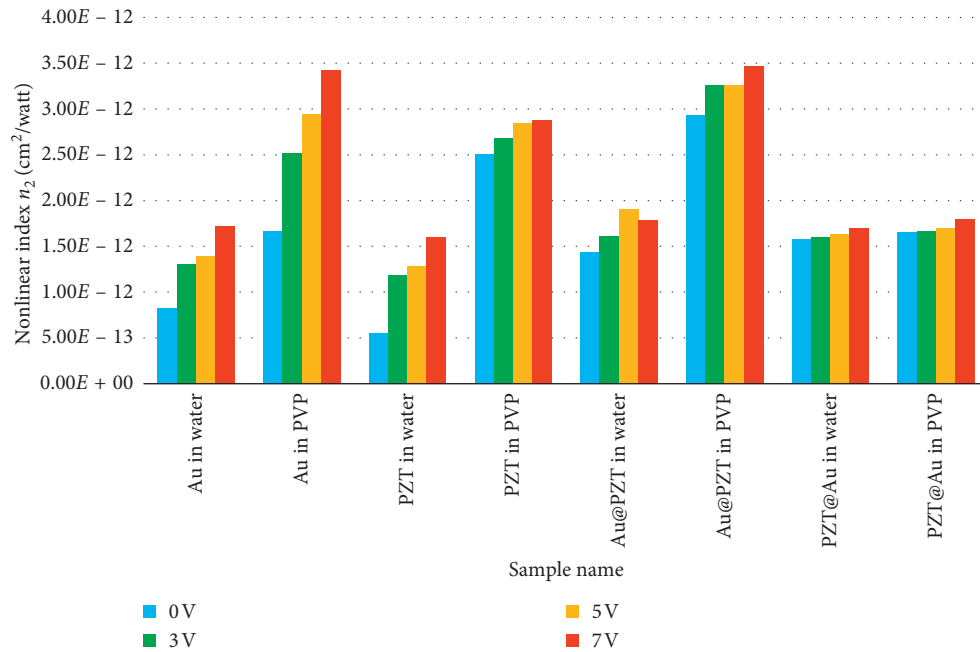
FIGURE 11: Effect of voltages on the nonlinear refractive index for different samples.
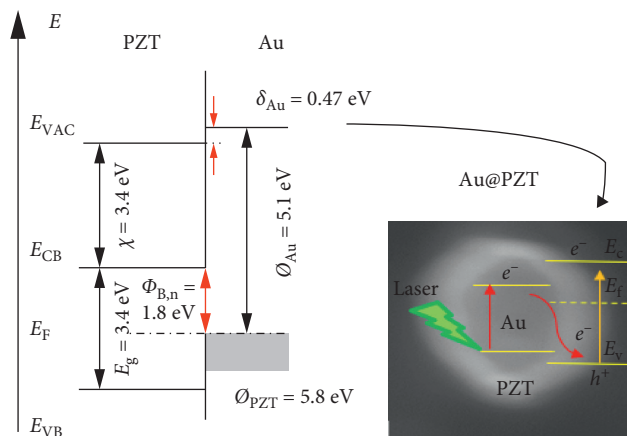
FIGURE 12: Band diagram of PZT/Au core/shell NP interfaces containing interface states reflected by the dipole potential δ.

5. Conclusions

In summary, we have synthesized Au NPs, PZT NPs, and core/shell NPs dispersed in various solvents by pulsed laser ablation with nanosecond laser pulses at 1064 nm and studied their optical-limiting properties. Our results show significant adjustability and tunability of the absorption band and SPR for each set of NPs that may be useful in the design of optical absorption devices. As we described how an external electric field affects the nonlinear refractive index of the samples, by using the closed-aperture Z-scan technique, a result suggests that the electric field modifies controlling of nonlinear refractive index values to samples which could be a perspective issue in piezophotonic materials development. Furthermore, combining the ferroelectric properties of PZT with the SPR wonders of Au NPs, we achieved tunability of the optical properties of the nanocomposite such as nonlinearity under external voltage.

Data Availability

The data used to support the findings of this study are available from the corresponding author upon request.

Conflicts of Interest

The authors declare that there are no conflicts of interest regarding the publication of this paper.

References

[1] Z. L. Wang, "Piezotronic and piezophototronic effects," *The Journal of Physical Chemistry Letters*, vol. 1, no. 9, pp. 1388–1393, 2010.

[2] Z. L. Wang, "Piezopotential gated nanowire devices: piezotronics and piezo-phototronics," *Nano Today*, vol. 5, no. 6, pp. 540–552, 2010.

[3] Z. L. Wang, "Progress in piezotronics and piezo-phototronics," *Advanced Materials*, vol. 24, no. 34, pp. 4632–4646, 2012.

[4] W. Wu, C. Pan, Y. Zhang, X. Wen, and Z. L. Wang, "Piezotronics and piezo-phototronics - from single nanodevices to array of devices and then to integrated functional system," *Nano Today*, vol. 8, no. 6, pp. 619–642, 2013.

[5] K. Jenkins, V. Nguyen, R. Zhu, and R. Yang, "Piezotronic effect: an emerging mechanism for sensing applications," *Sensors*, vol. 15, no. 9, pp. 22914–22940, 2015.

[6] W. Wu and Z. L. Wang, "Piezotronics and piezo-phototronics for adaptive electronics and optoelectronics," *Nature Reviews Materials*, vol. 1, no. 7, 2016.

[7] Z. Guo, H. Pan, C. Li et al., "Dynamic carrier transport modulation for constructing advanced devices with improved performance by piezotronic and piezo-phototronic effects: a brief review," *Semiconductor Science and Technology*, vol. 32, no. 8, article 083001, 2017.

[8] K. Y. Lee, J. Bae, S. Kim et al., "Depletion width engineering via surface modification for high performance semiconducting piezoelectric nanogenerators," *Nano Energy*, vol. 8, pp. 165–173, 2014.

[9] K. C. Hsieh, H. L. Chen, D. H. Wan, and J. Shieh, "Active modulation of surface plasmon resonance wavelengths by applying an electric field to gold nanoparticle-embedded ferroelectric films," *Journal of Physical Chemistry C*, vol. 112, no. 31, pp. 11673–11678, 2008.

[10] H. Li, Y. Yu, M. B. Starr, Z. Li, and X. Wang, "Piezotronic-enhanced photoelectrochemical reactions in Ni(OH)2-Decorated ZnO photoanodes," *Journal of Physical Chemistry Letters*, vol. 6, no. 17, pp. 3410–3416, 2015.

[11] M.-C. Wong, L. Chen, M.-K. Tsang, Y. Zhang, and J. Hao, "Magnetic-induced luminescence from flexible composite laminates by coupling magnetic field to piezophotonic effect," *Advanced Materials*, vol. 27, no. 30, pp. 4488–4495, 2015.

[12] Y. Bai, Z. J. Wang, B. He, J. Z. Cui, and Z. D. Zhang, "Enhancement of polarization in ferroelectric films via the incorporation of gold nanoparticles," *ACS Omega*, vol. 2, no. 12, pp. 9067–9073, 2017.

[13] F. Chen, W.-B. Wu, S.-Y. Li, and A. Klein, "Energy band alignment at ferroelectric/electrode interface determined by photoelectron spectroscopy," *Chinese Physics B*, vol. 23, no. 1, article 017702, 2014.

[14] H. Imam, K. Elsayed, M. A. Ahmed, and R. Ramdan, "Effect of experimental parameters on the fabrication of gold nanoparticles via laser ablation," *Optics and Photonics Journal*, vol. 02, no. 2, pp. 73–84, 2012.

[15] R. Ghosh Chaudhuri and S. Paria, "Core/shell nanoparticles: classes, properties, synthesis mechanisms, characterization, and applications," *Chemical Reviews*, vol. 112, no. 4, pp. 2373–2433, 2011.

[16] A. Essaidi, "Size control of gold nanoparticles during laser ablation in liquids with different functional molecules," *Journal of Laser Micro/Nanoengineering*, vol. 8, no. 2, pp. 131–136, 2013.

[17] C. D. Sai and A. B. Ngac, "Effect of core-shell structure on optical properties of Au-Cu2O nanoparticles," *Physica B: Condensed Matter*, vol. 532, pp. 216–220, 2018.

[18] S. M. Hamidi and M. A. Oskuei, "Adjustable surface plasmon resonance with Au, Ag, and Ag@Au core-shell nanoparticles," *Chinese Optics Letters*, vol. 12, no. 3, pp. 31601–31604, 2014.

[19] F. Mafuné, J.-y. Kohno, Y. Takeda, and T. Kondow, "Full physical preparation of size-selected gold nanoparticles in solution: laser ablation and laser-induced size control," *Journal of Physical Chemistry B*, vol. 106, no. 31, pp. 7575–7577, 2002.

[20] A. Granmayeh Rad, H. Abbasi, and M. H. Afzali, "Gold nanoparticles: synthesising, characterizing and reviewing novel application in recent years," *Physics Procedia*, vol. 22, pp. 203–208, 2011.

[21] W. H. Eisa, E. Al-Ashkar, S. M. El-Mossalamy, and S. S. M. Ali, "PVP induce self-seeding process for growth of Au@Ag core@shell nanocomposites," *Chemical Physics Letters*, vol. 651, pp. 28–33, 2016.

[22] F. Bao, J.-F. Li, B. Ren, R.-A. Gu, and Z.-Q. Tian, "Synthesis and characterization of Au@Co and Au@Ni Core–Shell nanoparticles and their applications in surface-enhanced Raman spectroscopy," *Journal of Physical Chemistry C*, vol. 112, no. 2, pp. 345–350, 2008.

[23] S. M. Hamidi and M. A. Oskuei, "Magneto-plasmonic effect in cobalt thin film incorporating core-shell Ag@Au nanoparticles," *Journal of Superconductivity and Novel Magnetism*, vol. 27, no. 6, pp. 1469–1472, 2013.

[24] S. Yilmaz, "Optical properties of some mixed nematic liquid crystals in electric field," *Materials Chemistry and Physics*, vol. 110, no. 1, pp. 140–144, 2008.

[25] Z. Dehghani, E. Saievar Iranizad, and M. Nadafan, "Investigation of electric field effect on the third order nonlinear optical properties of Fe3O4 nanoparticles-doped nematic liquid crystal," *Optics Communications*, vol. 334, pp. 16–21, 2015.

[26] S. Scaramuzza, M. Zerbetto, and V. Amendola, "Synthesis of gold nanoparticles in liquid environment by laser ablation with geometrically confined configurations: insights to improve size control and productivity," *Journal of Physical Chemistry C*, vol. 120, no. 17, pp. 9453–9463, 2016.

[27] V. Amendola and M. Moreno, "Laser ablation synthesis in solution and size manipulation of noble metal nanoparticles," *Physical Chemistry Chemical Physics*, vol. 11, no. 20, p. 3805, 2009.

[28] M. Yin, H. P. Li, S. H. Tang, and W. Ji, "Determination of nonlinear absorption and refraction by single Z-scan method," *Applied Physics B: Lasers and Optics*, vol. 70, no. 4, pp. 587–591, 2000.

[29] B. E. Saleh and M. C. Teich, "Fundamentals of photonics," in *Wiley Series in Pure and Applied Optics*, Wiley, Hoboken, NJ, USA, 1991.

[30] N. Dalir, S. Javadian, and Z. Dehghani, "High optical nonlinearity of nematic liquid crystal doped with graphen oxide," *Journal of Molecular Liquids*, vol. 244, pp. 103–109, 2017.

[31] M. Nadafan, R. Malekfar, and Z. Dehghani, "Structural and optical properties of cordierite glass-ceramic doped in polyurethane matrix," *AIP Advances*, vol. 5, no. 6, article 067135, 2015.

[32] M. Nadafan, R. Malekfar, and Z. Dehghani, "Microstructural and nonlinear optical properties of SiO2 and Al2O3 nanoparticles doped in polyurethane," *Journal of Materials Research*, vol. 30, no. 11, pp. 1788–1796, 2015.

[33] H. Y. Hora and R. Shen, "The Principles of Nonlinear Optics, John Wiley & Sons, New York, 1984, 576 pages," *Laser and Particle Beams*, vol. 4, no. 2, p. 318, 1986.

[34] I.-C. Khoo and S.-T. Wu, *Optics and Nonlinear Optics of 17 Liquid Crystals*, World Scientific Books, Singapore, 1993.

[35] S. M. Majhi, G. K. Naik, H.-J. Lee et al., "Au@NiO core-shell nanoparticles as a p-type gas sensor: novel synthesis, characterization, and their gas sensing properties with sensing mechanism," *Sensors and Actuators B: Chemical*, vol. 268, pp. 223–231, 2018.

[36] M. Heinz, V. V. Srabionyan, L. A. Avakyan et al., "Formation of bimetallic gold-silver nanoparticles in glass by UV laser irradiation," *Journal of Alloys and Compounds*, vol. 767, pp. 1253–1263, 2018.

[37] Z. Dehghani, N. Dalir, M. Nadafan, M. H. Majles Ara, and E. Saievar Iranizad, "Investigation of electrical and nonlinear optical properties of colloidal composite nematic liquid crystal," *Journal of Molecular Liquids*, vol. 225, pp. 502–509, 2017.

[38] D. R. Vinayakumara, M. Kumar, P. Sreekanth, R. Philip, and S. Kumar, "Synthesis, characterization and nonlinear optical studies of novel blue-light emitting room temperature truxene discotic liquid crystals," *RSC Advances*, vol. 5, no. 34, pp. 26596–26603, 2015.

[39] E. Saievar Iranizad, Z. Dehghani, and M. Nadafan, "Nonlinear optical properties of nematic liquid crystal doped with different compositional percentage of synthesis of Fe_3O_4 nanoparticles," *Journal of Molecular Liquids*, vol. 190, pp. 6–9, 2014.

[40] S. Pramodini, P. Poornesh, and K. K. Nagaraja, "Thermally induced nonlinear optical response and optical power limiting of acid blue 40 dye," *Current Applied Physics*, vol. 13, no. 7, pp. 1175–1182, 2013.

[41] D. H. G. Espinosa and R. K. Onmori, "Optical nonlinearities and thermal lens effect of a-Si:H films investigated by Z-scan technique," *Physics Procedia*, vol. 28, pp. 33–38, 2012.

[42] J. Jadhav and S. Biswas, "Hybrid ZnO:Ag core-shell nanoparticles for wastewater treatment: growth mechanism and plasmonically enhanced photocatalytic activity," *Applied Surface Science*, vol. 456, pp. 49–58, 2018.

[43] P. Mahala, M. Patel, N. Gupta, J. Kim, and B. H. Lee, "Schottky junction interfacial properties at high temperature: a case of AgNWs embedded metal oxide/p-Si," *Physica B: Condensed Matter*, vol. 537, pp. 228–235, 2018.

Research Article

Surface Modification by Combination of Dip-Pen Nanolithography and Soft Lithography for Reduction of Bacterial Adhesion

Santiago Arango-Santander [ID],[1,2] **Alejandro Pelaez-Vargas** [ID],[1] **Sidónio C. Freitas** [ID],[1] **and Claudia García**[2]

[1]*GIOM Group, School of Dentistry, Universidad Cooperativa de Colombia, Carrera 47 # 37 sur 18, Envigado, Colombia*
[2]*Cerámicos y Vítreos Group, School of Physics, Universidad Nacional de Colombia, Calle 59 A # 63-20, Medellín, Colombia*

Correspondence should be addressed to Santiago Arango-Santander; santiago.arango@campusucc.edu.co

Dip-pen nanolithography (DPN) and soft lithography are techniques suitable to modify the surface of biomaterials. Modified surfaces might play a role in modulating cells and reducing bacterial adhesion and biofilm formation. The main objective of this study was threefold: first, to create patterns at microscale on model surfaces using DPN; second, to duplicate and transfer these patterns to a real biomaterial surface using a microstamping technique; and finally, to assess bacterial adhesion to these developed patterned surfaces using the cariogenic species *Streptococcus mutans*. DPN was used with a polymeric adhesive to create dot patterns on model surfaces. Elastomeric polydimethylsiloxane was used to duplicate the patterns and silica sol to transfer them to the medical grade stainless steel 316L surface by microstamping. Optical microscopy and atomic force microscopy (AFM) were used to characterize the patterns. *S. mutans* adhesion was assessed by colony-forming units (CFUs), MTT viability assay, and scanning electron microscopy (SEM). DPN allowed creating microarrays from 1 to 5 μm in diameter on model surfaces that were successfully transferred to the stainless steel 316L surface via microstamping. A significant reduction up to one order of magnitude in bacterial adhesion to micropatterned surfaces was observed. The presented experimental approach may be used to create patterns at microscale on a surface and transfer them to other surfaces of interest. A reduction in bacterial adhesion to patterned surfaces might have a major impact since adhesion is a key step in biofilm formation and development of biomaterial-related infections.

1. Introduction

Biomimetics can be defined as the science that studies the formation, structure, or function of biologically produced substances and materials and biological mechanisms and processes to synthetize similar products by artificial mechanisms which mimic nature [1], is an approach that could be applied to materials science, and contributes to enhance or increase biomaterials compatibility [2]. Surface characteristics based on shark tissues have been applied to a polymeric material allowing the reduction of *S. aureus* adhesion and biofilm formation [3]. In addition, this same pattern was used on silicone to assess reduction of adhesion and biofilm formation of pneumonia-related bacterial species, and similar results were obtained [4]. Therefore, controlled modification of the surface with patterns based on natural structures has shown that bacterial adhesion and biofilm formation may be delayed compared to unmodified surfaces [3, 5]. Glinel et al. [6] summarize different approaches, such as coating materials with essential oils or antiquorum-sensing molecules, immobilization of antimicrobial peptides, and fabrication of structures on the surface of materials, that have been investigated to incorporate biomimetics into surface modification as an alternative to creating antibacterial surfaces.

Surfaces can be modified using different techniques, including photolithography [7], soft lithography [8–11], dip-pen nanolithography [12], ultrasonic nanocrystal surface

modification (UNSM) [13], colloid lithography, vapor annealing [14], or laser beam irradiation [15], among others.

Photolithography has long been recognized as the most common technique to manufacture the master model necessary for soft lithography [3, 7, 8, 11, 16, 17]. Chung et al. [3] used photolithography and soft lithography to modify the surface of PDMS in order to evaluate bacterial behavior in contact with patterned surfaces and found that bacteria are slower to colonize and form a mature biofilm on a patterned surface. Hochbaum and Aizenberg [5] obtained similar results and concluded that a patterned surface is more difficult to be colonized by bacteria as the size of the features approaches the size of a single bacterium. Vasudevan et al. [18] modified PDMS to compare bacterial adhesion to modified versus flat surfaces and found that *E. cloacae* covered more surface on flat PDMS (50%) than any of the modified PDMS surfaces (20% or below). Xu and Siedlecki [19] used photolithography and soft lithography to modify polyurethane urea to evaluate bacterial adhesion of *S. epidermidis* and *S. aureus* under dynamic conditions and concluded that bacterial adhesion followed a decreasing tendency as the shear rate increased on the modified surface compared to a flat surface, particularly for *S. epidermidis* in PBS, and adhesion reduction reached values up to 90%. However, photolithography presents several disadvantages, especially in the biomedical field, since it requires expensive equipment and facilities, is composed of several rigorous steps, no control over surface chemistry exists, and cannot be implemented on curved or nonplanar surfaces [20].

Soft lithography is a collection of indirect techniques through duplication and transfer procedures that allow the fabrication of patterned surfaces at the micron and submicron levels [7, 8]. This set of techniques relies on an elastic polymer to be used as a mask or stamp to pattern soft materials, such as polymers, gels, and organic monolayers. The soft lithographic techniques have in common the use of poly(dimethylsiloxane) (PDMS) as the key component to copy the structures fabricated from a model known as master. Among the advantages of this technique, the high number of replicas that may be produced in PDMS from one master is perhaps the most relevant [21].

Dip-pen nanolithography (DPN) is a direct technique that allows creating patterns directly on the surface of materials for a variety of purposes, including protein deposition [22, 23] or fabrication of protein arrays [24, 25]. It is a tip-based technique that uses an atomic force microscopy tip as a "nib," a solid substrate as "paper," and molecules with chemical affinity for the solid substrate as "ink" [12]. Many solutions and molecules, including proteins, colloidal particles, and inorganic compounds, have been used as inks [23, 25, 26]. The advantages of DPN include the fabrication of complex multicomponent assemblies with no cross contamination [24], the process is adaptable and is not ink or surface specific, no special operating conditions are required, and any pattern may be created [27]. Its main disadvantage is that patterning of large areas may become a slow process since each feature has to be made separately [28].

Photolithography and soft lithography are two widely reported techniques to modify the surface of materials for biomedical applications [11, 16, 17]. DPN has received attention as an alternative to chemically modifying a surface [29] and as a tool to create patterns to be used with other lithographic techniques [30]. However, the combination of soft lithography and dip-pen nanolithography for biomedical applications, particularly for evaluation of bacterial adhesion to modified surfaces, has not been studied as far as we know. DPN may be a promising alternative method to create the master since this technique offers some advantages over photolithography, including the fact that it is a direct deposition method that does not require a series of steps and any pattern could be fabricated on any surface, including nonplanar surfaces.

The current work presents, to the best of our knowledge, for the first time the application of these combined technologies to modify the surface of a medical grade material in order to reduce bacterial adhesion. Therefore, the objective of this work was to create dot patterns on model surfaces of silicon and gold using DPN, then duplicate and transfer these patterns to the surface of stainless steel 316L using a soft lithographic technique, and evaluate the adhesion of the cariogenic species *Streptococcus mutans* to these developed surfaces. Patterned surfaces may have a potential interest in medicine and dentistry for enhancing the surface of devices such as orthopedic implants, dental prosthetics, cardiac valves, or osseous-fixation plates, among others, as modified surfaces have demonstrated not only a reduction in bacterial adhesion [3–6] but also an improvement in cellular adhesion and arrangement [10, 11], which will ultimately lead to improving the correlation between biomaterials/devices and surrounding tissues.

2. Materials and Methods

2.1. Chemicals. A commercial polymeric adhesive (Norland Optical Adhesive 68T, Norland Products, Inc., USA) was used as ink. It was kept at 4°C throughout the experiments.

Silica sol was prepared using the one-stage sol-gel method as previously described by us [31, 32]. Tetraethylorthosilicate (TEOS) and methyltriethoxysilane (MTES) (ABCR GmbH & Co., Germany) were used as silica precursors for the hybrid sol, 0.1 N nitric acid (Merck Millipore, USA) and acetic acid (glacial, 100% v/v, Merck Millipore, USA) were used as catalysts, and absolute ethanol (99.9% v/v, Merck Millipore, USA) was used as solvent. The final concentration of SiO_2 was $18\,gL^{-1}$.

2.2. Substrates. Commercial 1 cm × 1 cm silicon and gold wafers (Nanoink, Inc., USA) were used as model substrates due to their affinity for the ink. These substrates contain an embedded matrix of letters to assist in pattern location for further imaging and analysis.

Stainless steel 316L (SS316L) (Onlinemetals.com, USA) 10 × 10 × 1 mm plates were polished using 1 μm diamond paste (LECO Corporation, USA) until a mirror-like surface was obtained. Then, SS316L plates were sequentially cleaned using surfactant, acetone (99.8% v/v, Merck Millipore, USA), distilled water, and absolute ethanol (99% v/v, Merck

Millipore, USA) for 8 min each in an ultrasound bath and let dry in air.

2.3. Dot Pattern Master Fabrication.

DPN was carried out using the NLP 2000 system (NanoInk, Inc., USA). $0.4 \mu L$ of ink were injected into each well of a twelve-well plate (NanoInk, Inc., USA). M triangular tips (10-tip arrays) were selected to deposit the ink on the substrates considering their stiffness.

The master designed ($\sim 10 \, mm^2$) consisted of a dot array disposed in an 11×11 matrix, which means that each tip fabricated 11 dots in the X axis and 11 in the Y axis per line. This configuration was selected because the space taken by two consecutive dots, including the space between them, was approximately $6 \mu m$. As each type M triangular tip deposits ink in the X axis at a length of $66 \mu m$, this configuration allowed each tip to fabricate its own 11×11 arrangement without overlapping with the neighbor array. Thus, each line of dots was composed of 121 dots in the X axis and 11 dots in the Y axis. Lines were repeatedly fabricated to cover the entire area. A Z-clearance of $50 \mu m$ and a dwell time of 0.5 seconds were established.

2.4. Microstamping.

Polydimethylsiloxane (PDMS) (Silastic T-2, Dow Corning Corporation, USA) was used to duplicate the master created on both substrates (Figure 1). Only silicon and gold masters which comprised dots of $1 \mu m$ diameter were used. PDMS was prepared according to the manufacturer and cured for 24 h. Then, it was carefully removed from the surface, visually inspected to verify its physical integrity, and thermally treated at 80°C for 3 h to complete polymerization. The PDMS was used as a microstamp to transfer SiO_2 to SS316L surfaces. In brief, $7 \mu L$ of the silica sol were deposited onto the stainless-steel surface, a PDMS microstamp was placed over the drop, gentle pressure was applied, and the sol was allowed to gel for 4 h at RT. The PDMS stamp was then carefully removed, and the stainless-steel plate with the transferred pattern was heat treated at 450°C for 30 min in a furnace.

Three types of samples were obtained. SS316L control group (SS polished) was comprised of polished plates and two experimental groups: flat SiO_2-coated plates (SS coated) prepared by dip coating (4 cm/min) and SiO_2-patterned plates (SS micropatterned) obtained by microstamping. SS-coated and SS-micropatterned plates were thermally treated at 450°C for 30 min.

2.5. Surface Characterization.

Dot master and PDMS microstamp surfaces were characterized using optical microscopy (OM) (Axio Vert 40 MAT, Carl Zeiss Microscopy GmbH, Germany) and atomic force microscopy (AFM) (Nanosurf Easyscan 2, Nanosurf AG, Switzerland). For AFM acquisition, a NCLR (Nanosensors™, Switzerland) tip at a force constant of 48 N/m in the tapping mode was used. Images postprocessing was performed using software AxioVision (V 4.9.1.0, Carl Zeiss Microscopy GmbH,

Germany), software Image J 1.51 J [33], and software WSxM 5.0 [34].

SS316L surface properties were evaluated by AFM as described above and by contact angle measurement. 10 AFM images of $50 \mu m \times 50 \mu m$ were used for surface roughness measurements with the arithmetic average of the roughness profile (Ra) calculated using software for AFM analysis (Gwyddion 2.34, Department of Nanometrology, Czech Metrology Institute, Czech Republic). Contact angle measurements followed the sessile drop method on 10 random plates from each group using a camera (Canon EOS Rebel XS, Japan) and a macrolens (105 mm F2.8 EX DG OS, Sigma, USA) with the angle values obtained using software AxioVision.

2.6. Biological Characterization.

Streptococcus mutans (ATCC 25175, Microbiologics, USA) was used to characterize bacterial adhesion to control and experimental surfaces.

Bacteria were grown in brain-heart infusion (BHI) agar (Scharlab S.L., Spain) supplemented with 0.2 U/ml bacitracin (Sigma Fluka, USA) for 24 h at 37° ± 1°C. Then, they were cultured in a solution of peptone water (3% peptone and 20% sucrose in distilled water) at 37° ± 1°C for 24 h. The bacterial solution was centrifuged, and the supernatant was discarded. The bacterial pellet was resuspended in peptone water at 10^{-7} CFUs/ml by measuring the nephelometric turbidity unit (NTU) (based on a calibration curve of NTU vs CFU/ml). SS316L plates from control and experimental groups were placed in single well of 24-well nontreated polystyrene plates (Costar, Corning, Inc., USA), and 1 ml of bacterial solution was added to each well. Plates were incubated at 37° ± 1°C for 2, 4, 8, 12, and 24 h. After each incubation time, SS316L plates were removed, washed three times with $500 \mu l$ of 0.9% saline solution to remove nonadherent bacteria, and prepared for characterization methods.

For scanning electron microscopy (JEOL JSM-5910LV, Japan), analyses of bacterial adhesion morphology and coverage, control, and experimental surfaces were preincubated with 3% glutaraldehyde to permanently fix bacterial cells.

The MTT (3-(4,5-dimethylthiazol-2-yl)-2,5-diphenyltetrazolium bromide) tetrazolium reduction assay was used to assess cell viability. In brief, $500 \mu l$ of MTT solution prepared with 5 mg/ml in distilled and sterile water (Molecular Probe, USA) was added to control and experimental surfaces and incubated at 37° ± 1°C for 4 h. Afterwards, surfaces were photographed using an inverted microscope (AxioVert 40 MAT, Carl Zeiss Microscopy GmbH, Germany) at 50X. Software Image J 1.51 J [33] was used to calculate the percentage area covered by bacterial colonies.

Samples from control and experimental surfaces were also subjected to a 3-second sonication at 50% power (Qsonica 125, USA) in 10 ml of 0.9% saline solution. Serial dilutions of the sonicated solutions were prepared and $10 \mu l$ from each tube were cultured in the BHI agar in triplicate following the drop plate method [35]. Culture plates were
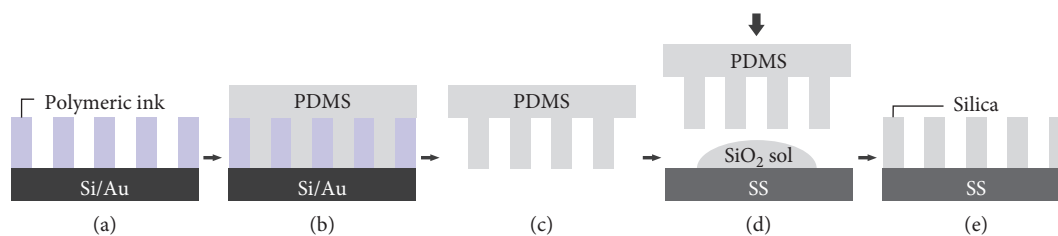
FIGURE 1: A: master pattern created through DPN. B: PDMS onto pattern. C: negative pattern duplicate in PDMS (microstamp). D: transfer to the SS316L substrate using silica sol. E: dot pattern in silica on SS316L.

incubated at $37° \pm 1°C$ for 48 h, and then colony-forming units (CFUs) were counted. This entire process was repeated three times in different time periods.

2.7. Statistical Analysis. Experimental results are presented as the mean ± standard deviation (SD). Comparison between groups was performed using the one-way ANOVA test with post hoc Tukey method. Values of $p < 0.05$ were considered statistically significant. Software SPSS (V. 22) was used for statistical analysis.

The datasets generated during the current study are available upon request from the corresponding author.

3. Results

3.1. Dot Master Fabrication. A commercial adhesive was used as ink to create a pattern on model silicon and gold substrates.

Dot matrices were first created on silicon. Dot dimensions were determined using the DPN system and confirmed by means of OM, SEM, and AFM. OM images showed dot diameters averaging $2.9 \pm 0.27\,\mu m$ and 314 ± 21 nm of height. The separation between two consecutive dots depended on the diameter of each dot. Figure 2 shows SEM and AFM images of patterns deposited on silicon and gold.

As it was observed on silicon, dot diameter averaged $2.8\,\mu m$ and features showed heights in the 200–400 nm range with a separation between two neighboring dots between 3 and $5\,\mu m$ on gold.

3.2. Microstamping. Figure 3 shows a $50 \times 50\,\mu m$ AFM image of a negative duplicate of the positive dot pattern created on the surface (PDMS stamp). Transfer of dot patterns to SS316L using silica sol was successful as the dot diameter averaged $2.49 \pm 0.4\,\mu m$ and dot height averaged 298 ± 26 nm, which were in the same size range as the features created on the original substrates (Figure 4).

3.3. Surface Properties. Contact angle measurements showed an increase from polished to coated to micropatterned SS (Figure 5). The difference in contact angle measurements was statistically significant among the three surface treatments ($p = 0.001$). Regarding roughness, coated SS showed the lowest values, followed by polished and micropatterned.

The difference in roughness between coated and micropatterned SS was statistically significant ($p = 0.001$).

3.4. Biological Characterization. Streptococcus mutans was added to the three substrates (SS polished, SS coated, and SS micropatterned) for five different time periods (2, 4, 8, 12, and 24 h). The MTT assay showed bacterial viability increasing from 4 to 8 h regardless of surface treatment. The lowest bacterial colonization was observed on the SS-patterned surface at both times (Figures 6(c) and 6(f)). The percentage of the covered area at 4 h did not show differences for SS-polished, SS-coated and SS-patterned surfaces (~33%, 34%, and 31%, respectively). However, at 8 h, the percentage of the covered area showed an important reduction in the SS-patterned surface (23%) compared to SS-polished (47%) and SS-coated (51%) surfaces.

Bacterial adhesion quantified by CFUs increased from 2 to 8 h and then decreased up to 24 h (Figure 7). SS coated showed statistically significant differences in bacterial adhesion and colonization between 2 and 4 h ($p = 0.001$) and 2 and 8 h ($p = 0.001$), when the maximum colonization was observed. A statistically significant reduction from 8 to 24 h was observed ($p = 0.001$). SS micropatterned showed the lowest bacterial adhesion and colonization, and no statistically significant differences were found at different times. In the control surface SS polished, a statistically significant difference was found in bacterial adhesion between 4 and 8 h ($p = 0.001$). Then, a statistically significant reduction up to 24 h was observed ($p = 0.001$). Among groups, there was a statistically significant difference between control SS polished and SS coated ($p = 0.003$) and between SS coated and SS micropatterned ($p = 0.003$) at 4 h. Likewise, statistically significant differences between control SS polished and SS micropatterned ($p = 0.003$) and between SS coated and SS micropatterned ($p = 0.001$) at 8 h were found. SEM images of bacterial adhesion and colonization on the different surfaces are shown in Figure 8.

4. Discussion

A combination of DPN and soft lithography with the objective of modifying the surface of a biomaterial to analyze whether this approach could have an effect on bacterial adhesion has not been published to the best of our knowledge. Therefore, DPN was used to fabricate the patterns on model surfaces, and soft lithography was employed to transfer such pattern to a real biomaterial surface. Such
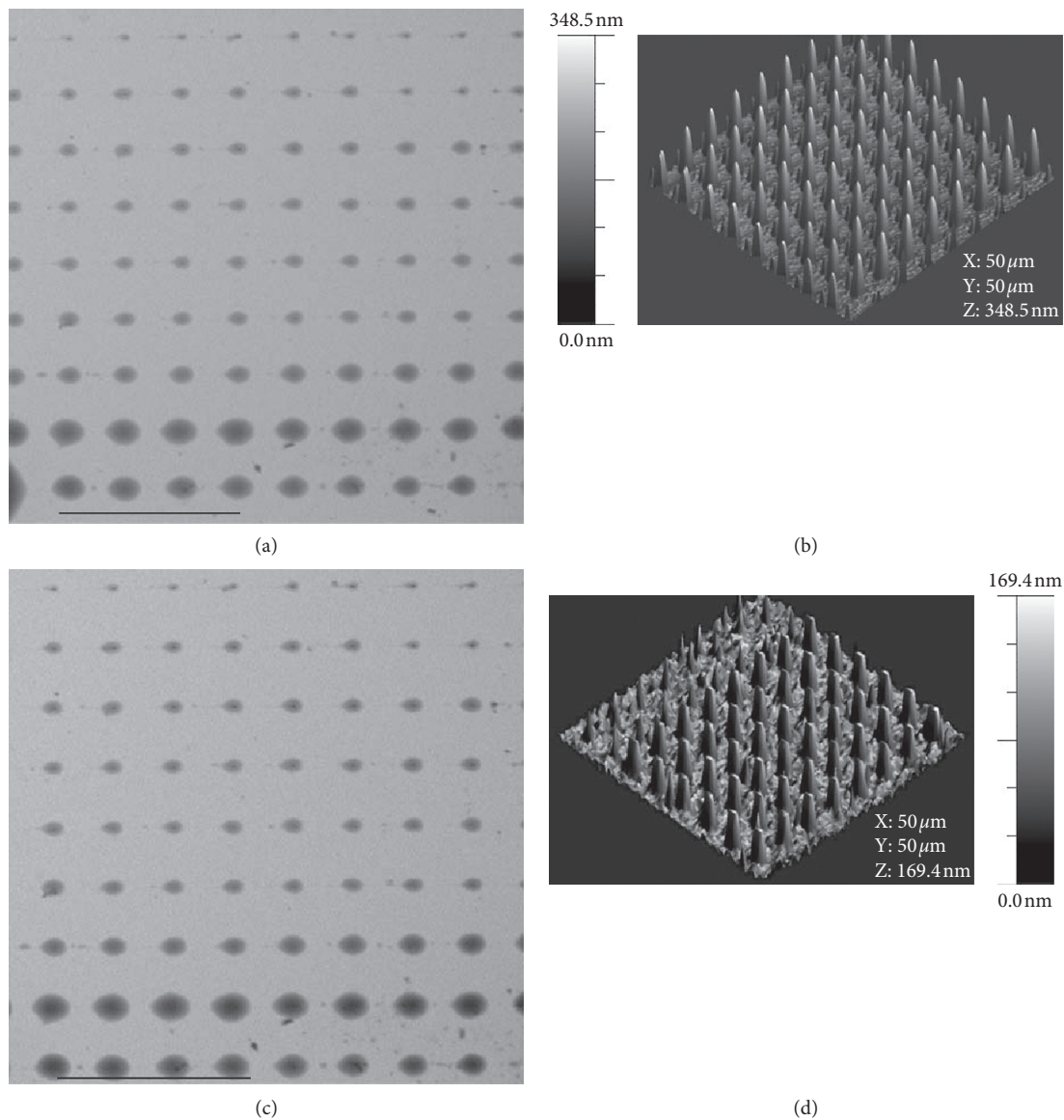
(a)

(b)

(c)

(d)

FIGURE 2: SEM and AFM images of the polymeric dot pattern on silicon (a, b) and gold (c, d). The bars in (a) and (c) are 20 μm.
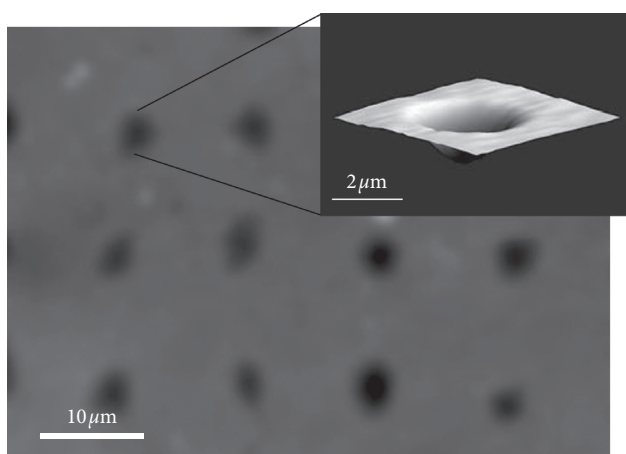

FIGURE 3: AFM image of the negative dot pattern on PDMS and detail of one of the negative dots (upper right).

substrates were selected because the silica sol and the polymeric adhesive showed high affinity with both metallic and nonmetallic substrates.

Two main complications appeared during pattern fabrication. Firstly, ink was difficult to apply on both substrates due to its high viscosity, which congested and fractured the tips. Congested tips, in turn, applied substantial amounts of ink on a single spot, creating ponds of ink on the substrate. This was especially evident on silicon surfaces. Careful calibration and manipulation of the NLP system was necessary to counteract this condition. The process of applying ink on gold substrates was more straightforward, although tip congestion and pond formation were also observed. A process of bleeding the excess of ink, as suggested by Wang et al. [27], was applied to ensure that the correct amount of ink was deposited. Nevertheless, some ponds were observed when fabricating the patterns, and some of them forming

308.9 nm

X: 50 μm
Y: 50 μm
Z: 308.9 nm

0.0 nm
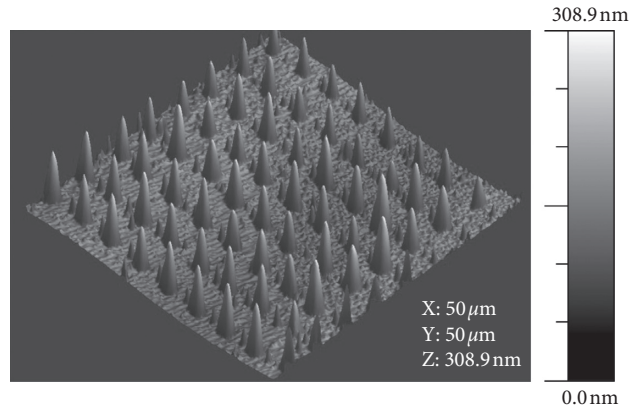
Figure 4: AFM image of pattern transference to SS316L.

	SS polished	SS coated	SS micropatterned
Contact angle (°)	57 ± 4	75 ± 3	87 ± 3
Ra (nm)	23 ± 10	17 ± 7	70 ± 17
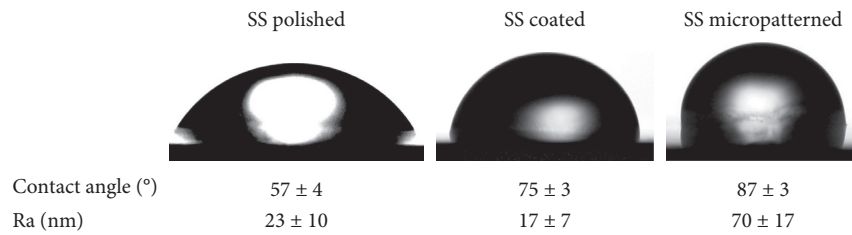
Figure 5: Water contact angles images of SS polished (a), SS coated (b), and SS micropatterned (c) and contact angle and roughness average measurements.

(a)

(b)

(c)

(d)

Figure 6: Continued.

(e)

(f)
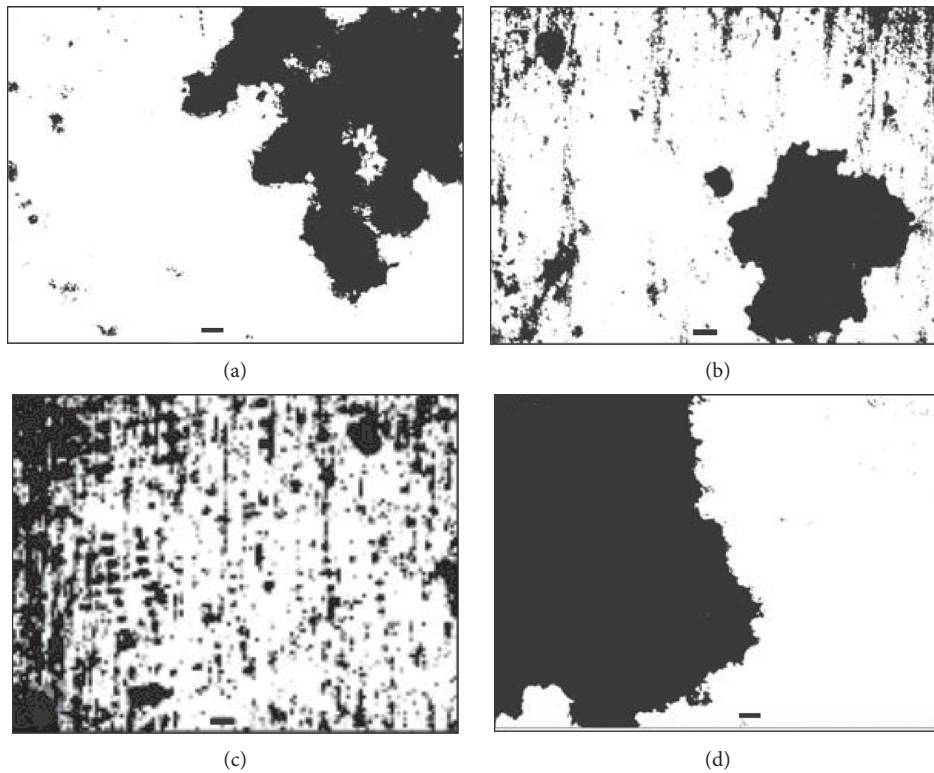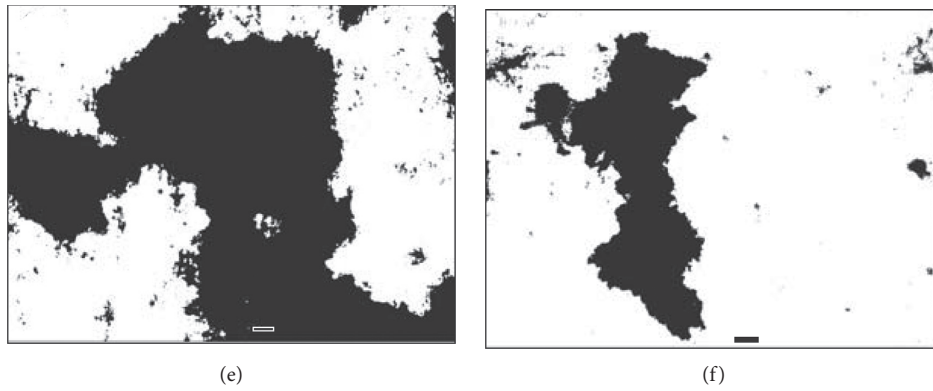
FIGURE 6: MTT images at 4 h (a–c) and 8 h (d–f): SS polished (a, d), SS coated (b, e), and SS patterned (c, f). Black spots are bacterial accumulation on each surface. The bar is 20 μm.
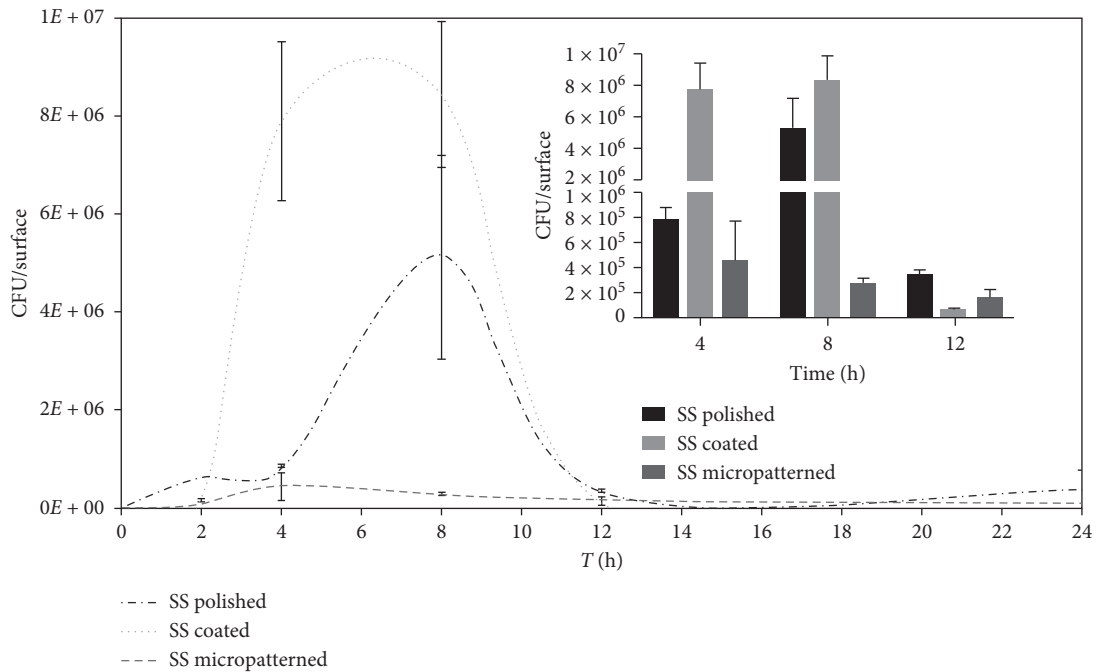
FIGURE 7: Bacterial adhesion and colonization at the different times. The inset figure shows bacterial adhesion at 4, 8 and 12 h, with maximum adhesion at 8 h.

(a)

(b)

(c)
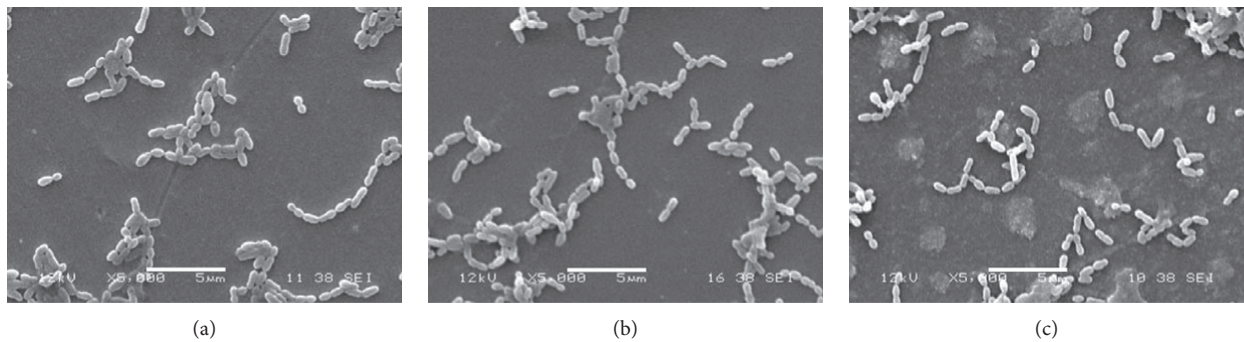
FIGURE 8: Bacterial colonization at 8 h on SS polished (a), SS coated (b), and SS micropatterned (c). The bar is 5 μm.

after the process had been initiated. Secondly, some tips would not always carry enough ink to create a particular pattern, so empty spots within a specific pattern could be observed. This situation was corrected, when possible, by creating another pattern on-site.

The features created with DPN in the current work are in the order of microns (1–5 μm in diameter) and submicrons (over 100 to over 400 nm in height), although nanometric sizes (50–100 nm) can be reached [36]. The topography was designed considering the fact that S. mutans organize in short chains and clusters, as observed in SEM images, so the physical obstacles (dot height and pitch) had to be constructed in such a way that they should surround groups of bacteria rather than a single bacterium as it has been proposed that the size of the features in the same range as the bacterial species reduce bacterial adhesion and colonization because such features act as physical barriers [5].

The duplication process was straightforward, and the dimensions of the fabricated patterns on silicon and gold were conserved after transferring to stainless steel as PDMS is capable of copying and transferring features below the threshold than those created in this work (800 nm) [37]. After the silica coated and patterned surfaces were obtained, surface characterization by means of surface roughness and contact angle measurement to analyze surface hydrophobicity was performed. Hydrophobicity increased after coating or patterning the stainless-steel surface, which is in accordance to other studies having SS coated with silica [38–41]. Santos et al. [39] observed an increase in hydrophobicity but did not present any explanation for this, while Yang et al. [41] obtained contact angle values of over 120° with silica sol synthetized using TEOS and MTES as precursors at different molar ratios and explained that the hydrophobicity largely depends on surface chemistry and morphology of the silica films. On the contrary, Hosseinalipour et al. [38] found that hydrophilicity increases as TEOS ratios increase when used a silica sol with tetraethylorthosilicate (TEOS) and 3-methacryloxypropyl-trimethoxysilane (TMSM) at different molar ratios. However, more recently, Wang et al. [40] evaluated SS316L samples coated with silica sol prepared using TEOS and MTES as precursors at different molar ratios and found an increase in hydrophobicity as the TEOS : MTES ratio increased. Their contact angle values for the same TEOS : MTES ratio as obtained in the present work (40 : 60) were similar (85°) and higher than the uncoated SS316L samples (27°). According to Wang et al., this increase in hydrophobicity in the current work may be explained by the amount of methyl groups that, in turn, would lower the ability of the surface to absorb water [40]. In regarding roughness, it was reduced after SS being coated with silica, which may be explained by the deposition of a thick homogeneous silica film that was able to cover the underneath surface masking its scratches and therefore making it smoother. The highest roughness shown by the patterned surface may be explicated by the fact that PDMS showed a rougher surface (47.4 ± 24.1 nm on average) and the roughness of such material might have been transferred to the substrate.

Bacterial adhesion to a biomaterial is a dynamic process, and many variables are involved with surface properties that play a significant role in the early steps of adhesion. In the current work, bacterial adhesion to patterned surfaces showed a reduction of at least one order of magnitude compared with polished and silica-coated SS316L, which is significant for a short-time contact study (24 h). The adhesion peak of this bacterial strain onto the control surface (uncoated SS) under the conditions of these experiments was 8 h, so this time was the most relevant in this study. In addition, low viability was observed after 12 h probably due to the fact that the culture medium was not replaced and bacteria could be deprived of nutrients. Furthermore, the surface patterned with silica was the roughest and also the most hydrophobic, while the silica coated surface was more hydrophilic and smooth, but they showed an opposite behavior to bacterial adhesion. These findings demonstrate that the highest antibacterial effect shown by the patterned surface could be explained by a physical rather than a chemical phenomenon (from the silica). The accessible contact area is relevant for bacteria to adhere, and since S. mutans organize in short chains and form small clusters, the pattern created on the surface may have acted as physical obstacles for clusters to organize, expand, and find each other, at least temporarily, which did not occur on the flat surfaces (polished or coated). In addition, the most hydrophobic surface showed the lowest bacterial adhesion, which may suggest that this bacterial strain possess a more hydrophilic surface, as suggested by Satou et al. [42] after finding that different strains of S. mutans have a hydrophilic surface and that hydrophilic bacterial show higher adhesion to hydrophilic surfaces [43]. Considering surface modification and its effect on bacteria adhesion, the results of this work are in agreement with other authors once it shows that the introduction of micropatterns reduces in 95% the S. mutans adhesion at 8 h, which is even higher than described by Chung et al. [3] with 87% reduction in S. aureus at 14 days and similar to May et al. [4] ranging between 95.6 and 99.9% since they evaluated different bacterial strains.

The current work presents an alternative approach in which surface modification by a combination of DPN and microstamping showed reduction of bacterial adhesion to a modified surface. Besides reduction of bacterial adhesion, this combination presented a number of advantages, including the fact that DPN shows high resolution and is a versatile technique because patterns can be created on virtually any substrate, as long as chemical affinity exists, and soft lithography is a high-throughput technique, which counteracts the fact that DPN is a very low throughput procedure. The applicability of DPN in real-life biomaterials resides in the ability to create any pattern on any substrate using any compound as ink. Some limitations have to be addressed beforehand, including high costs and low throughput. In our consideration, the combination with soft lithography overcomes the latter limitation. Future considerations should include longer evaluation periods, evaluation with different bacterial strains, and surface effects using multispecies approaches.

5. Conclusions

Surface patterning via DPN showed to be a time-consuming process to pattern large areas, but its high resolution demonstrated to be a suitable alternative to photolithography for the fabrication of the master that is necessary for soft lithography. Moreover, the combination of DPN and soft lithography improved the process, and larger areas could be patterned in a reduced amount of time. Patterned surfaces showed lower bacterial adhesion compared to coated or polished surfaces. The results of this work showed that physical surface modification with these combined techniques is a successful approach to reduce bacterial adhesion and biofilm formation on biomaterials, which may assist in preventing biomaterial-related infections.

Data Availability

The data used to support the findings of this study are available from the corresponding author upon request.

Conflicts of Interest

The authors declare that there are no conflicts of interest.

Acknowledgments

References

[1] B. Bhushan, "Biomimetics: lessons from nature-an overview," *Philosophical Transactions of the Royal Society A: Mathematical, Physical and Engineering Sciences*, vol. 367, no. 1893, pp. 1445–1486, 2009.

[2] M. B. Rahmany and M. Van Dyke, "Biomimetic approaches to modulate cellular adhesion in biomaterials: a review," *Acta Biomaterialia*, vol. 9, no. 3, pp. 5431–5437, 2013.

[3] K. K. Chung, J. F. Schumacher, E. M. Sampson, R. A. Burne, P. J. Antonelli, and A. B. Brennan, "Impact of engineered surface microtopography on biofilm formation of *Staphylococcus aureus*," *Biointerphases*, vol. 2, no. 2, pp. 89–94, 2007.

[4] R. M. May, M. G. Hoffman, M. J. Sogo et al., "Micro-patterned surfaces reduce bacterial colonization and biofilm formation in vitro: potential for enhancing endotracheal tube designs," *Clinical and Translational Medicine*, vol. 3, no. 1, p. 8, 2014.

[5] A. I. Hochbaum and J. Aizenberg, "Bacteria pattern spontaneously on periodic nanostructure arrays," *Nano Letters*, vol. 10, no. 9, pp. 3717–3721, 2010.

[6] K. Glinel, P. Thebault, V. Humblot, C. M. Pradier, and T. Jouenne, "Antibacterial surfaces developed from bioinspired approaches," *Acta Biomaterialia*, vol. 8, no. 5, pp. 1670–1684, 2012.

[7] A. Pelaez-Vargas, D. Gallego-Perez, A. Carvalho, M. H. Fernandes, D. J. Hansford, and F. J. Monteiro, "Effects of density of anisotropic microstamped silica thin films on guided bone tissue regeneration-in vitro study," *Journal of Biomedical Materials Research Part B: Applied Biomaterials*, vol. 101B, no. 5, pp. 762–769, 2013.

[8] A. Carvalho, A. Pelaez-Vargas, D. Gallego-Perez et al., "Micropatterned silica thin films with nanohydroxyapatite micro-aggregates for guided tissue regeneration," *Dental Materials*, vol. 28, no. 12, pp. 1250–1260, 2012.

[9] Y. Xia and G. M. Whitesides, "Soft lithography," *Angewandte Chemie International Edition*, vol. 37, no. 5, pp. 550–575, 1998.

[10] A. Pelaez-Vargas, D. Gallego-Perez, N. Ferrell, M. H. Fernandes, D. Hansford, and F. J. Monteiro, "Early spreading and propagation of human bone marrow stem cells on isotropic and anisotropic topographies of silica thin films produced via microstamping," *Microscopy and Microanalysis*, vol. 16, no. 6, pp. 670–676, 2010.

[11] A. Pelaez-Vargas, D. Gallego-Perez, M. Magallanes-Perdomo et al., "Isotropic micropatterned silica coatings on zirconia induce guided cell growth for dental implants," *Dental Materials*, vol. 27, no. 6, pp. 581–589, 2011.

[12] R. D. Piner, J. Zhu, F. Xu, S. Hong, and C. A. Mirkin, ""Dip-Pen" nanolithography," *Science*, vol. 283, no. 5402, pp. 661–663, 1999.

[13] X. Hou, S. Mankoci, N. Walters et al., "Hierarchical structures on nickel-titanium fabricated by ultrasonic nanocrystal surface modification," *Materials Science and Engineering: C*, vol. 93, pp. 12–20, 2018.

[14] E. Miliutina, O. Guselnikova, V. Marchuk et al., "Vapor annealing and colloid lithography—an effective tool to control spatial resolution of surface modification," *Langmuir*, vol. 34, no. 43, pp. 12861–12869, 2018.

[15] L. C. Pires, F. P. S. Guastaldi, A. V. B. Nogueira, N. T. C. Oliveira, A. C. Guastaldi, and J. A. Cirelli, "Physicochemical, morphological, and biological analyses of Ti-15Mo alloy surface modified by laser beam irradiation," *Lasers in Medical Science*, pp. 1–10, 2018.

[16] A. Pelaez-Vargas, N. Ferrel, M. H. Fernandes, D. Hansford, and F. J. Monteiro, "Cells spreading on micro-fabricated silica thin film coatings," *Microscopy and Microanalysis*, vol. 15, no. 3, pp. 77-78, 2009.

[17] A. Pelaez-Vargas, N. Ferrel, M. H. Fernandes, D. J. Hansford, and F. J. Monteiro, "Cellular alignment induction during early in vitro culture stages using micropatterned glass coatings produced by sol-gel process," *Key Engineering Materials*, vol. 396-398, pp. 303–306, 2009.

[18] R. Vasudevan, A. J. Kennedy, M. Merritt, F. H. Crocker, and R. H. Baney, "Microscale patterned surfaces reduce bacterial fouling-microscopic and theoretical analysis," *Colloids and Surfaces B: Biointerfaces*, vol. 117, pp. 225–232, 2014.

[19] L. C. Xu and C. A. Siedlecki, "Submicron-textured biomaterial surface reduces staphylococcal bacterial adhesion and biofilm formation," *Acta Biomaterialia*, vol. 8, no. 1, pp. 72–81, 2012.

[20] K. T. M. Tran and T. D. Nguyen, "Lithography-based methods to manufacture materials at small scales," *Journal of Science: Advanced Materials and Devices*, vol. 2, no. 1, pp. 1–14, 2017.

[21] D. B. Weibel, W. R. DiLuzio, and G. M. Whitesides, "Microfabrication meets microbiology," *Nature*, vol. 5, no. 3, pp. 209–218, 2007.

[22] J. H. Lim, D. S. Ginger, K. B. Lee, J. Heo, J. M. Nam, and C. A. Mirkin, "Direct-write dip-pen nanolithography of proteins on modified silicon oxide surfaces," *Angewandte*

Chemie International Edition, vol. 42, no. 20, pp. 2309–2312, 2003.

[23] D. L. Wilson, R. Martin, S. Hong, M. Cronin-Golomb, C. A. Mirkin, and D. L. Kaplan, "Surface organization and nanopatterning of collagen by dip-pen nanolithography," *Proceedings of the National Academy of Sciences*, vol. 98, no. 24, pp. 13660–13664, 2001.

[24] K. B. Lee, J. H. Lim, and C. A. Mirkin, "Protein nanostructures formed via direct-write dip-pen nanolithography," *Journal of the American Chemical Society*, vol. 125, no. 19, pp. 5588-5589, 2003.

[25] K. B. Lee, S. J. Park, C. A. Mirkin, J. C. Smith, and M. Mrksich, "Protein nanoarrays generated by dip-pen nanolithography," *Science*, vol. 295, no. 5560, pp. 1702–1705, 2002.

[26] S. Gilles, A. Tuchscherer, H. Lang, and U. Simon, "Dip-pen-based direct writing of conducting silver dots," *Journal of Colloid and Interface Science*, vol. 406, pp. 256–262, 2013.

[27] H. T. Wang, O. A. Nafday, J. R. Haaheim et al., "Toward conductive traces: dip-pen nanolithography of silver nanoparticle-based inks," *Applied Physics Letters*, vol. 93, no. 14, p. 143105, 2008.

[28] K. Anselme, P. Davidson, A. M. Popa, M. Giazzon, M. Liley, and L. Ploux, "The interaction of cells and bacteria with surfaces structured at the nanometre scale," *Acta Biomaterialia*, vol. 6, no. 10, pp. 3824–3846, 2010.

[29] Z. Zheng, W. J. Jang, G. Zheng, and C. A. Mirkin, "Topographically flat, chemically patterned PDMS stamps made by dip-pen nanolithography," *Angewandte Chemie International Edition*, vol. 47, no. 51, pp. 9951–9954, 2008.

[30] J. W. Jang, R. G. Sanedrin, A. J. Senesi et al., "Generation of metal photomasks by dip-pen nanolithography," *Small*, vol. 5, no. 16, pp. 1850–1853, 2009.

[31] C. García, S. Ceré, and A. Durán, "Bioactive coatings prepared by sol-gel on stainless steel 316L," *Journal of Non-Crystalline Solids*, vol. 348, pp. 218–224, 2004.

[32] C. García, S. Ceré, and A. Durán, "Bioactive coatings deposited on titanium alloys," *Journal of Non-Crystalline Solids*, vol. 352, no. 32–35, pp. 3488–3495, 2006.

[33] C. A. Schneider, W. S. Rasband, and K. W. Eliceiri, "NIH Image to ImageJ: 25 years of image analysis," *Nature Methods*, vol. 9, no. 7, pp. 671–675, 2012.

[34] I. Horcas, R. Fernandez, J. M. Gomez-Rodriguez, J. Colchero, J. Gomez-Herrero, and A. M. Baro, "WSXM: a software for scanning probe microscopy and a tool for nanotechnology," *Review of Scientific Instruments*, vol. 78, no. 1, article 013705, 2007.

[35] H. Naghili, H. Tajik, K. Mardani, S. M. Razavi Rouhani, A. Ehsani, and P. Zare, "Validation of drop plate technique for bacterial enumeration by parametric and nonparametric tests," *Veterinary Research Forum*, vol. 4, no. 3, pp. 179–183, 2013.

[36] D. S. Ginger, H. Zhang, and C. A. Mirkin, "The evolution of dip-pen nanolithography," *Angewandte Chemie International Edition*, vol. 43, no. 1, pp. 30–45, 2004.

[37] G. Csucs, T. Künzler, K. Feldman, F. Robin, and N. D. Spencer, "Microcontact printing of macromolecules with submicrometer resolution by means of polyolefin stamps," *Langmuir*, vol. 19, no. 15, pp. 6104–6109, 2003.

[38] M. Hosseinalipour, A. Ershad-langroudi, A. N. Hayati, and A. M. Nabizade-Haghighi, "Characterization of sol–gel coated 316L stainless steel for biomedical applications," *Progress in Organic Coatings*, vol. 67, no. 4, pp. 371–374, 2010.

[39] O. Santos, T. Nylander, R. Rosmaninho et al., "Modified stainless steel surfaces targeted to reduce fouling—surface characterization," *Journal of Food Engineering*, vol. 64, no. 1, pp. 63–79, 2004.

[40] M. Wang, Y. Wang, Y. Chen, and H. Gu, "Improving endothelialization on 316L stainless steel through wettability controllable coating by sol-gel technology," *Applied Surface Science*, vol. 268, pp. 73–78, 2013.

[41] H. Yang, P. Pi, Z. Q. Cai et al., "Facile preparation of super-hydrophobic and super-oleophilic silica film on stainless steel mesh via sol–gel process," *Applied Surface Science*, vol. 256, no. 13, pp. 4095–4102, 2010.

[42] J. Satou, A. Fukunaga, N. Satou, H. Shintani, and K. Okuda, "Streptococcal adherence on various restorative materials," *Journal of Dental Research*, vol. 67, no. 3, pp. 588–591, 1988.

[43] M. Katsikogianni and Y. F. Missirlis, "Concise review of mechanisms of bacterial adhesion to biomaterials and of techniques used in estimating bacteria-material interactions," *European Cells and Materials*, vol. 8, pp. 37–57, 2004.

Research Article

Konjac Sponge Derived Carbon Flakes with Optimized Pore Structure for High-Performance Supercapacitor

Bing Han (ID)**, Chongchong Geng** (ID)**, and Gong Cheng** (ID)

College of Environmental Science and Engineering, North China Electric Power University, Beijing 102206, China

Correspondence should be addressed to Bing Han; hanbing01@ncepu.edu.cn

Lamellar activated carbons derived from Konjac sponges (KACs) have been successfully fabricated through a facile KOH activation method. By manipulating the activation temperature and KOH/C ratio, the achieved KACs exhibit ultrahigh specific surface area up to ~3000 m^2/g and hierarchical pore structure with tunable micro/mesopore distribution. Notably, KACs possess plenty of worm-shaped micropores formed by graphene stacking layers with the lateral distance close to size of hydrated electrolyte ions. Owing to optimized pore structure, high graphitization, and extra O/N doping, KACs exhibited much enhanced specific capacitance (253.0 F/g), superior rate ability (77% retention of capacitance at 10 A/g), and remarkable cycling stability (0.4% decay under 5 A/g after 2000 cycles) in the acid electrolyte. The mass production ability of KAC materials and the knowledge of correlation between texture properties and capacitive performance open new opportunities for the application of such novel biomass-derived carbons in supercapacitor devices.

1. Introduction

The shortage of fossil fuels and booming demand for sustainable energy call for the development of highly efficient energy storage solutions [1, 2]. Supercapacitors (SCs), as a complementary or independent charge storage system for electric vehicles or regenerated applications, have exhibited bright prospect due to the high power density, fast charging process, and excellent cycling performance [3]. Based on the surface adsorption/desorption of electrolyte ions, electrochemical double-layer capacitors (EDLCs) are one important component of commercial electrochemical capacitors owing to their low cost and high operation safeties [4]. Nevertheless, the relatively low-energy density of EDLCs has restricted their further application. Therefore, much efforts have been made to increase the energy storage capability of EDLCs in recent years [5, 6]. One of the most effective strategies is to improve the specific capacitance through sophisticated design of electrode materials. Carbon nanomaterials are the dominant electrode materials for EDLCs. The past few decades have witnessed the development of various nanostructured carbon materials in SCs, ranging from the modified activated carbons (ACs) [7] to novel

carbon nanostructures based on carbon nanotube [8], graphene [9], or metal-organic framework- (MOF-) derived carbon [10].

ACs, by contrast, have been the mainstream electrode material in commercial SC devices due to the cost-effective and easy to scale up nature. To satisfy the demand of next generation SCs for both high-specific capacitance and rate ability, rational design of pore distribution/structure and optimization of surface modification have been urgently required for ACs while maintaining the considerable specific surface area (SSA) [11–13]. On one hand, micropores (pore size <2.0 nm) provide effective sites for ion adsorption-desorption, and mesopores (2.0 nm < pore size < 50 nm) play a dominant role in ion transportation [14]. Moreover, several studies have demonstrated the importance of sub-nanopores (pore size <1.0 nm) in largely increasing capacitance when the pore dimension matches the radius of the electrolyte ions [15, 16], which inspired attention on further optimizing the hierarchical pore structure. On the other hand, heteroatom (N, O, S, etc.) doping or group functionalization could produce surface redox reaction, therefore improving the accessibility by optimizing the wettability and introducing specific pseudocapacitance [13, 17, 18].

Furthermore, manipulation of the graphitization degree would increase the electrical conductivity, which facilitates the charge transfer especially at high rate [19, 20]. Therefore, development of well-designed ACs with high SSA, well-designed pore structure, heteroatom doping, and high graphitization degree opens new opportunities for this sort of traditional materials in future SC devices. Notably, biomass is an excellent precursor with the advantages of large amount, rich composition, and distinct primary texture [21]. Upon appropriate activation process, hierarchically porous ACs which inherit the original microstructure and heteroatom can be achieved [22, 23]. Thus, selection of appropriate carbon precursor and optimization of activation condition become the research hotspot in nowadays.

Konjac, which is composed of glucomannan with D-mannose and i-glucose in b(1,4) linkages, has been widely used as an agent for food ingredient in Asia [24]. Due to its low cost, easy for gelation, and good biocompatibility, Konjac glucomannan (KGM) has served as a gelling, texturizing, and film-forming agent in industries such as food, drug, and cosmetic [25]. Nevertheless, the application of ACs derived from Konjac-derived ACs in SCs has been rarely reported. Li et al. have demonstrated the first study of Konjac gel-derived porous biochar as electrode active materials in SCs, which exhibited the specific capacitance of 273.8 F/g at 1 A/g in 1 M KOH [26]. Additionally, "snow Konjac" is a sponge-like Konjac product consisting of KGM and rice flour (mass ratio of ~1 : 1) as main gradients. Taking advantages of the viscosity of KGM and swelling property of rice flour, such Konjac sponges process a loose and porous appearance with lamellar inner wall, which are expected to serve as a novel platform to achieve new structured ACs. Herein, we fabricated two-dimensional (2-D) graphitized carbon nanosheets from the Konjac sponge through the facile KOH activation method. By tuning the carbonization temperature and KOH/C ratio, Konjac sponge-derived ACs (KACs) with ultrahigh SSA (up to ~3000 m^2/g at KOH/C > 3), tunable micro/mesopore volume, varied O/N doping, and high graphitization degree have been achieved. Impressively, such 2-D KAC nanosheets show hierarchical pore structure with coexistence of micro/mesopores. Especially, the micropores contain large amount of worm-shaped graphene stacking layers with the lateral distance close to the size of hydrated electrolyte ions, which greatly benefit the capacitive performance. Therefore, compared with non-activated samples, KACs exhibited much enhanced specific capacitance, superior rate ability, and remarkable cycling stability in acid electrolyte. The relationship between the capacitive performance (specific capacitance and rate ability) and the texture property (SSA, micropore volume, and mesopore volume) as well as the graphitization degree is also elucidated, which would largely benefit the design and practical application of such KAC materials in SCs.

2. Materials and Methods

2.1. Chemicals.
The Konjac sponge with the brand "Leshan" was bought from Jingdong Mall. Potassium hydroxide (KOH) and hydrochloric acid (HCl) used were obtained from Aladdin (Shanghai, China). N-methylpyrrolidinone (NMP) was bought from Alfa Aesar.

2.2. Fabrication of Hierarchical Porous Carbon from Konjac Sponge.
The Konjac sponge was firstly crushed and precarbonized in the tube furnace under N_2 atmosphere at 500°C for 2 h, and the achieved sample was mixed thoroughly with KOH (C/KOH ratio of 1 : 3). The mixture was then carbonized under N_2 flow at 700°C, 800°C, and 900°C for 2 h. The resultant products were marked as Konjac derived activated carbon (KAC)- 700, 800, and 900, respectively. The precarbonized sample carbonized under 700°C without the addition of KOH was denoted as UAC. To evaluate the effect of carbonized temperature on the capacitive performance, the precarbonized carbon was mixed with different C/KOH ratios (1 : 1, 1 : 2, and 1 : 4) before the further carbonization at 800°C under N_2 atmosphere. The derived samples were denoted as KAC-1, 2, and 4, respectively. KAC-800 was equal to KAC-3. All the KAC samples were washed with 2 M HCl to remove the residual KOH and centrifuged with deionized water until the solution reached neutral condition. After drying in vacuum, the KAC materials were obtained. The synthetic process is shown in Scheme 1.

2.3. Characterization.
The morphology and high-resolution imaging were obtained from a Tecnai G2 F20 U-TWIN. Material phase analysis was conducted using an X-ray diffractometer (D/max-TTRIII). Information of chemical and elemental composition was achieved from X-ray photoelectron spectroscopy (XPS). Raman analysis was performed on a Renishaw inVia plus system at 513 nm laser excitation. Texture and pore information were recognized based on N_2 adsorption-desorption isotherms from a Micromeritics ASAP 2010 analyzer.

2.4. Electrochemical Testing.
The potential of KAC-based samples as SC electrode materials was evaluated on a CHI660E workstation. The related measurements were performed through a three-electrode system with an electrolyte of 1 M H_2SO_4. KAC-based samples (KAC-700, 800, and 900 and KAC-1 and 2) were ground with specific amount of acetylene black and polyvinylidene fluoride (mass percentage is 8 : 1 : 1) in N-methyl pyrrolidone (NMP) to form slurry, which was dispensed on graphite flake to form an area of 1 cm × 1 cm. The electrodes were dried in vacuum (80°C, 12 h). The mass loading was obtained by measuring the mass of the blank substrate and the dried working electrode. The Pt plate counterelectrode, as a prepared working electrode, and Hg/Hg$_2$SO$_4$ reference electrode formed the three-electrode system. Cyclic voltammetry (CV) and galvanostatic charge-discharge (GCD) results were achieved in the potential scope of −0.6~0.3 V. Electrochemical impedance spectra (EIS) were achieved under the condition of 5 mV and 100 kHz~0.01 Hz. The specific capacitance (Cs, F/g) was calculated based on the GCD curve according to the following equation:
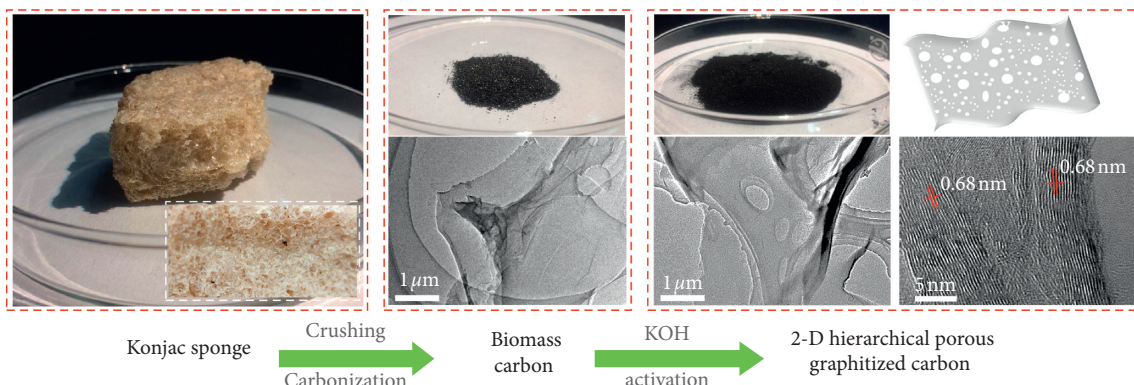
SCHEME 1: The synthetic procedures for hierarchical porous KAC materials.

$$\text{Cs} = \frac{It}{\Delta V m}, \tag{1}$$

where I and t are the charge-discharge current and discharging time, respectively, ΔV is the potential range, and m is the mass of the active material.

3. Results and Discussion

The pristine Konjac sponge precursor possessed laminar network structure in macroscopic view. TEM imaging provided intuitional information about the morphology and porous structure of the samples. As shown in Figure S1, the UAC sample exhibited very thin lamellar structure upon crushing and carbonization. The enlarged HR-TEM images indicated the amorphous nature of the nonactivated carbon flakes, which contained nanosized pores. In contrast, KOH activation gave rise to tremendous modification towards the KACs both in microstructure and graphitization. Interestingly, worm-shaped graphene bunches and amorphous area coexisted in KAC-based samples (Figures 1 and S2). The distance between graphene layers was 0.67 and 0.68 nm in KAC-700 and KAC-900, respectively (Figure S3). KAC-800 was dominated by the distorted short-range ordered crystalline with a lateral distance of ~0.67 and ~0.79 nm. As shown in Figure S4, staking graphene layers with larger lateral distance were clearly observed in KAC-1 (0.79 nm), KAC-2 (0.85 nm), and KAC-4 (0.75 nm). The enlargement of interlayer spacing for KAC-700 was further confirmed from selected-area electron diffraction (SAED) pattern (Figure S5(a)). Compared with the amorphous UAC carbon, the graphene crystallization zone indicated the increased graphitization of the KAC samples, which would largely benefit the capacitive performance arising from better electrical conductivity. Notably, the KOH etching effect became particularly obvious at a high temperature of 900°C and a high KOH/C ratio of 4 : 1, with the observation of the rough surface and plentiful mesopores. The negligible observation of the change of carbon lattice distances for KAC-4 may be due to the less-ordered crystalline area from the existence of great deal of mesopores (Figure S5(b)). Therefore, the hierarchical porous structure consisting of large amount of graphene layer subnanopore and a portion of mesopores formed due to activation process.

Furthermore, the XRD pattern of UAC showed broad peaks at $2\theta = 23°$ and $43°$ (Figure 2(a)), corresponding to the diffraction signal of (002) and (101) plane of amorphous carbon [27, 28]. KAC-based samples, in comparison, exhibited a negligible peak at 23° and largely reduced diffraction at 43° (Figures 2(a) and 2(b)), suggesting the rearrangement of the original amorphous carbon and introduction of large amount of pores. The steep increase in low-angle scatter in KAC samples compared with UAC originates from the enriched micro/mesopores [29]. As is shown in HRTEM, the graphene interlayer distance was much larger than the graphite (002) d-spacing of 0.34 nm, which may arise from the separation effect due to K insertion/intercalation into graphene layers [30]. The Raman spectra quantitatively demonstrate the graphitization degree of carbon materials (Figures 2(c) and 2(d)). KAC samples showed two Raman peaks at 1357 cm^{-1} and 1594 cm^{-1} characteristic of polycrystalline and crystal graphite, respectively [31, 32]. The intensity ratio of D-band and G-band (I_D/I_G) for KAC-700, 800, and 900 is 0.96, 0.96, and 1.00, respectively, while that for KAC-1, 2, and 4 were 0.95, 0.99, and 0.74. The much lower I_D/I_G value of KAC samples compared with commercial activated carbon (~1.92) demonstrated the high graphitization degree [33]. This result also illustrated that the disorder degree of carbon increased with the carbonization temperature. The sharper peak with temperature and KOH/C was consistent with the larger graphene separation observed from HRTEM images. On one hand, the high content of defective carbon provided more active sites or active surface areas, giving rise to improved capacitance. On the other hand, graphitized carbon increases the electric conductivity which benefited the rate capability [20]. Therefore, the optimized capacitive performance is called for the good intercoordination of both effects.

XPS spectra further provided the chemical composition and element binding information. As shown in Figure 3, the high-resolution C1s spectra of KAC-based samples consisted of a peak centered at 284.7 eV with small tail at the high-binding energy side and a shoulder peak in the range of 288.0~292.8 eV. The former peak can be deconvoluted into sp^2-bonded carbon (284.7 eV) with a small tail containing sp^3-bonded carbon (285.8 eV). The shoulder peak consisted of three individual component peaks, corresponding to
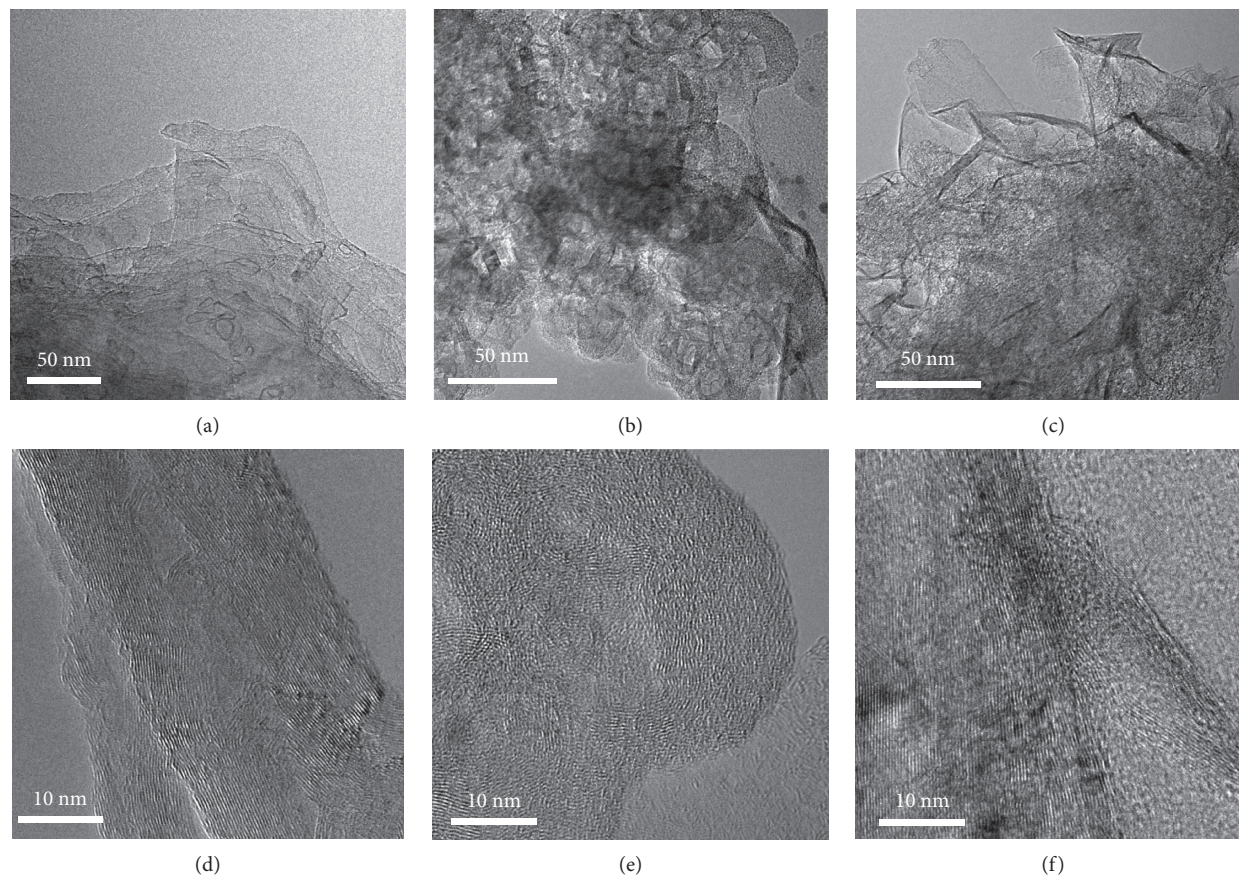
FIGURE 1: Transmission electron microscopy (TEM) images of (a, d) KAC-700, (b, e) KAC-800, and (c, f) KAC-900.

carbonyl group C=O (287.0 eV), carboxyl O-C=O (289.2 eV), and a satellite peak of π–π^* (291.4 eV), respectively [34, 35]. The overwhelmingly strong peak of sp^2 carbon demonstrated the formation of graphene-like carbon sheets with high graphitization, which agreed well with the Raman results. As shown in Figure S6, O1s spectra of KAC-based samples indicated the presence of C=O quinone-type groups (O-I), C–OH phenol groups and/or C–O–C ether groups (O-II), and chemisorbed oxygen (COOH carboxylic groups) and/or water (O-III), respectively [36]. Table S1 shows that KACs were composed of C and O and trace amount of N. With the activation temperature and the KOH/C ratio increasing, the content of carbon increased and the oxygen decreased (Table S1). The decreased total intensity of oxygenated groups is also observed from Figure S6. The existence of carbonyl/carboxyl groups and small amount of N benefited the improvement of the wettability, therefore facilitating the accessibility of the electrolyte ions. Also, the oxygenated groups provided pseudocapacitance for the EDLC-dominated capacitance of KAC-based samples [37].

As is revealed from TEM images, KOH etching process produced abundant hierarchical pores in the Konjac-derived carbon substrate. Therefore, BET characterization was conducted to further evaluate the texture properties and the effect of KOH amount and activation temperature on the pore structure of KAC materials. As shown in Figures 4(a) and 4(c), UAC and all the KAC samples exhibited steep N_2 adsorption at very low relative pressure (p/p_0), which was the characteristic of the type-I isotherm [38]. This result indicated the existence of large amount of micropores in these samples. Notably, KAC-900 and KAC-4 possessed a H_4-type hysteresis loop at $p/p_0 > 0.4$, suggesting the presence of mesopores [11]. The pore size distribution curves (Figure 4(b)) showed that all KAC-700, 800, and 900 samples possessed subnanopores centered at ~0.68 and 0.80 nm, respectively. This was consistent with the lateral distance achieved from HRTEM images. Along with the subnanopores, large micropores of ~1.20 nm and large amount of mesopores coexisted in these samples. KAC-900 exhibited larger mesopores (~2.60 nm) than KAC-700 and 800 (~2.0 nm). In contrast, UAC only showed a pore peak centered at ~1.17 nm with very low pore volume, indicating the introduction of both subnanopores and mesopores through the KOH activation process. Moreover, changing the KOH/C could also modulate the pore structure of KAC materials. KAC-1 and 2 showed similar pore distribution with KAC-800, while KAC-4 exhibited obvious introduction of enlarged mesopores of 2.76 and 3.42 nm (Figure 4(d)). Previous studies evidenced that subnanopores with the size matching up with that of electrolyte ions could greatly enhance the specific capacitance [15, 39, 40]. Considering the reported size of hydrated SO_4^{2-} ion (0.533 nm) [41, 42], KAC-700, KAC-2, and KAC-3 containing large fraction of subnanopore sized at ~0.68 nm were expected to have highly
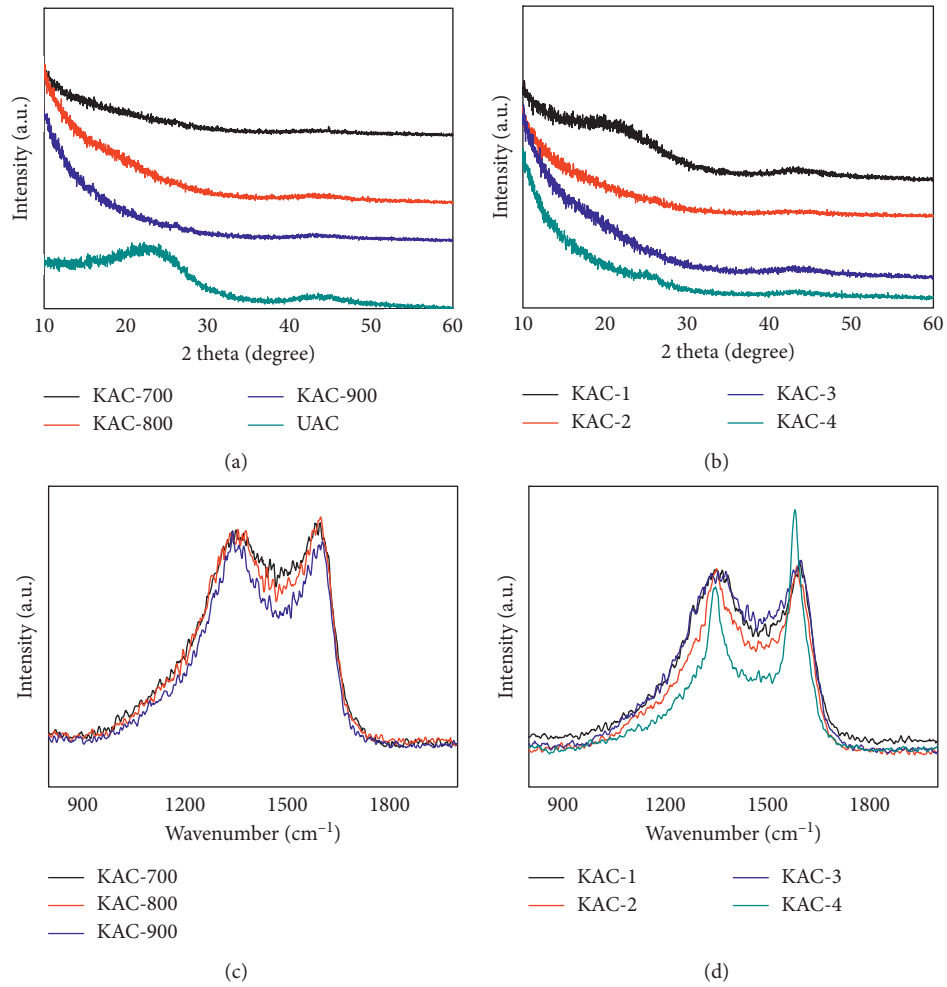
(a)

(b)

(c)

(d)

FIGURE 2: XRD patterns of KAC materials activated under (a) different temperatures and (b) different KOH/C ratios in comparison with UAC, (c) and (d) Raman spectra of KAC-based materials.
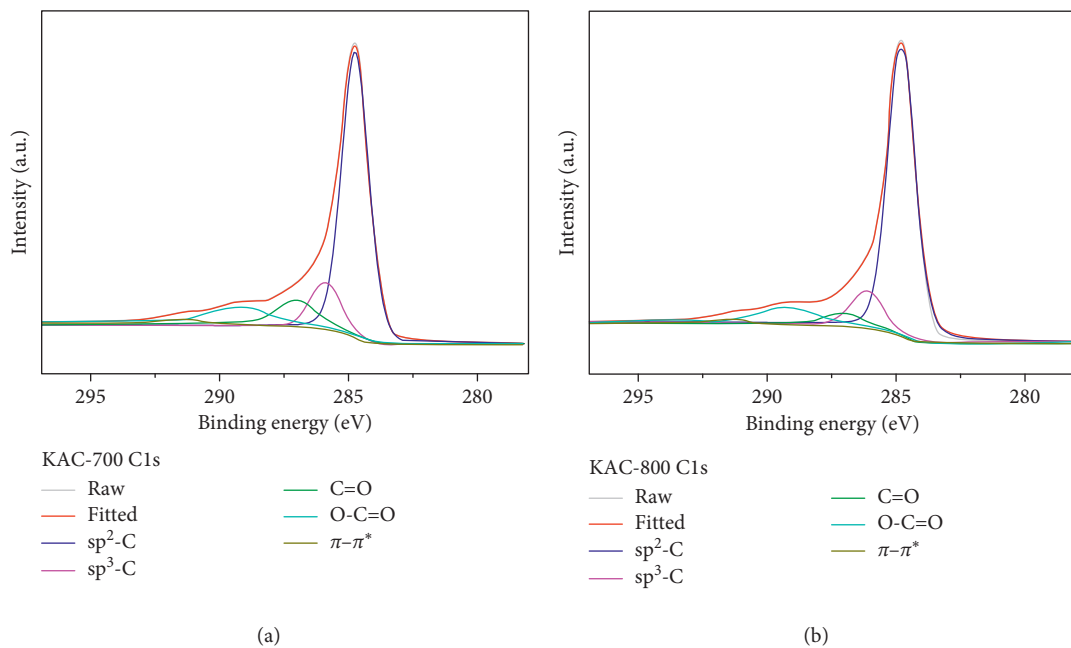

(a)

(b)

FIGURE 3: Continued.
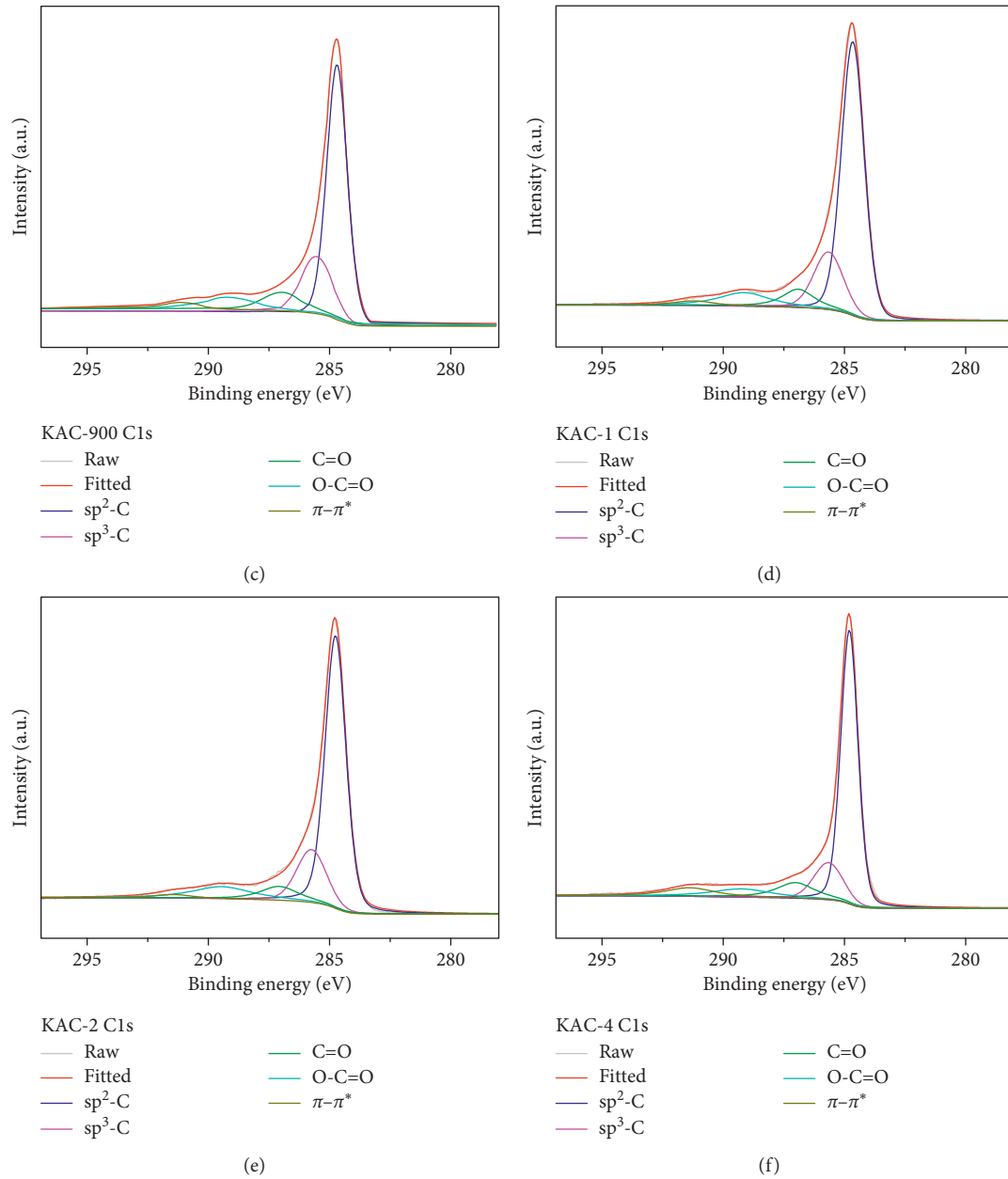
(c)

(d)

(e)

(f)

Figure 3: XPS C1s spectra of KAC-based samples.

effective surface area for ion adsorption-desorption, yielding improved specific capacitance. The worm-shaped pores formed from the carbon layers also contributed to the enhanced energy storage capability [43]. Despite the absence of macropores, the thin lamellar KAC materials would shorten the ion transportation route which reduced the diffusion impedance. Detailed specific surface area (SSA) and pore volume statistics are summarized in Table 1. At KOH/C = 3, KAC materials possessed ultrahigh SSA up to ~3117 m^2/g (KAC-700 and 900), which was about ~21 times and ~1.9 times higher than UAC and commercial-activated carbon, respectively. This result evidenced the efficiency of etching reaction between KOH and C precursor (6KOH + C ↔ 2K + 3H$_2$ +2K$_2$CO$_3$) [29, 44]. As the ratio increases, SSA based on the BET model (S_{BET}) increased. With KOH/C ratio larger

than 3 : 1, SSA did not change much with the increase of the ratio or the carbonization temperature. But the pore structure including the distribution and relevant pore volume of micropores and mesopores exhibited large differences (Table 1). According to the density functional theory (DFT) method, KAC samples achieved at lower carbonization temperature (700 and 800°C) and low KOH/C ratio (1 : 1 and 2 : 1) showed SSA with 90%~93% contribution from micropores. Nevertheless, the portion of micropores decreased to 71% and 56% under the formation of mesopores for KAC-900 and KAC-4, respectively. The pore volume was also an important parameter to evaluate the capacitance and rate ability of EDLC-type SCs. Compared with the UAC sample, the KOH activation process under different conditions gave rise to the KAC materials with
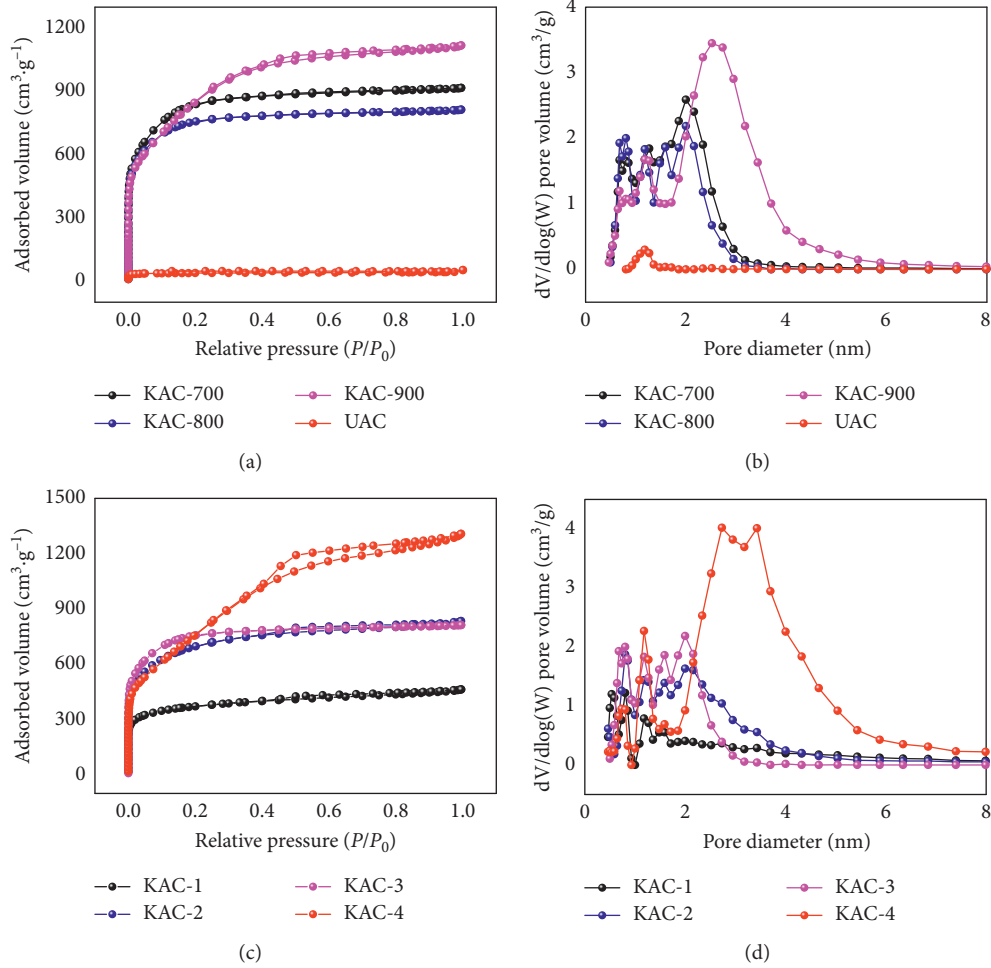
FIGURE 4: Nitrogen adsorption/desorption isotherms (a, c) and DFT pore size distribution curve (b, d) of KAC-based samples in comparison with UAC.

TABLE 1: Texture properties of the KAC samples achieved under different conditions and UAC.[a]

Sample	S_{BET} (m²/g)	S_{DFT} (m²/g)	S_{DFT} (m²/g)			Pore vol (cm³/g)		
			$d < 2$ nm	$d < 2$ nm	SSA_{mic} (%)	$d < 2$ nm	$d > 2$ nm	V_{mes}/V_{mic}
KAC-700	3117	1952	1757	195	90	0.94	0.24	0.25
KAC-800	2841	1861	1731	126	93	0.88	0.16	0.18
KAC-900	3116	1895	1352	543	71	0.70	0.77	1.10
KAC-1	1382	1178	1094	84	93	0.43	0.16	0.37
KAC-2	2557	1612	1402	210	87	0.76	0.31	0.41
KAC-4	2888	1687	949	738	56	0.49	1.24	2.53
UAC	152	70.5	68.3	2.2	97	0.05	0.005	0.10

[a]S_{BET} and S_{DFT}: the specific surface area (SSA) based on Brunauer–Emmett–Teller (BET) and density functional theory (DFT) method; SSA_{mic}: the microporous surface area; V_{mes}/V_{mic}: the ratio between mesopore and micropore volume.

highly tunable pore structure. The KAC samples had very high pore volume compared with the biomass derived carbon counterparts [34, 45, 46]. Notably, KAC-700 possessed the highest micropore volume of 0.94 cm³/g while KAC-4 had the highest ratio between mesopore and micropore volume up to 2.56. The large microporous SSA and pore volume would benefit the charge storage capability due to high electroadsorption interaction between electrolyte ions and accessible pore surface. The high ratio of V_{mes}/V_{mic}

guaranteed the high-rate transportation of ions from solution to the active surface with the large fraction of mesopores acting as ion channels [47]. Therefore, the above results indicated the advantage of the Konjac sponge as the precursor for activated biomass carbon materials, and the efficiency of KOH etching treatment in providing optimized SC electrode materials with modulated SSA and pore structure. The series of KAC samples not only provided excellent model materials for studying the dependence of

supercapacitor performance on the structural properties of carbon materials but also paved the way for desirable carbon materials for high-performance SCs.

The capacitive performance of KACs as electrode materials for SC application was tested in the aqueous solution of 1 M H_2SO_4. As shown in Figures 5(a), 6(a), and S7, all KAC samples exhibited rectangular-shaped CV curves at 5 mV/s and showed little deviation with the scan speed up to 100 mV/s, indicating the ideal EDLC behavior of the electrodes. The symmetric and triangular charge-discharge curves provided further confirmation for the good rate performance (Figures 5(b), 6(b), and S7). The small humps in CV curves originated from the pseudocapacitance due to O/N-heteroatom doping. It can be obviously noticed that KOH-activated carbons showed tremendously enhanced specific capacitance in comparison with UAC. The exact capacitance value was determined from GCD data (Table S2). When tuning the activation temperature, KAC-700 possessed the largest capacitance (235.1 F/g) at 0.5 A/g. Upon tuning the KOH/C ratio, KAC-2 and KAC-3 showed larger capacitance of 227.0 and 223.0 F/g, respectively. In overall, the modulation of KOH activation condition towards capacitance can be understood based on the previous analysis of pore information. KAC-700 had the largest microporous SSA ($1754 m^2/g$) and the maximum micropore volume ($0.94 cm^3/g$), followed by KAC-800 ($S_{mic} = 1731 m^2/g$ and $V_{mic} = 0.88 cm^3/g$ based on DFT calculation) and KAC-2 ($S_{mic} = 1402 m^2/g$ and $V_{mic} = 0.76 cm^3/g$). The large microporous surface provided abundant active sites for trapping the electrolyte ions, which greatly benefited the energy storage. Moreover, the pore structure played an important role in improving the specific capacitance. On one hand, KAC-700, KAC-2, and KAC-3 contained large fraction of the sub-nanopore sized at 0.68 nm. The well-fitted dimension with the electrolyte ion would benefit the energy storage [41, 42]. On the other hand, the moderate I_D/I_G demonstrated the existence of the defective carbon, which increased the exposed active surface for better charge storage performance.

Furthermore, rate capability was also a very important property to evaluate the capacitive performance of materials. The dependence of specific capacitance on the current density is shown in Figures 5(c) and 6(c). KAC-900 and KAC-4 showed remarkable capacitance retention of ~77% with the current density increasing from 0.5 A/g to 10 A/g, which was better than that of the rest KAC samples (70%~72%). The GCD curves of the KAC samples under different current densities are shown in Figure S8. For UAC, 71.4% of the original capacitance decayed at 10 A/g (Figure S9). The previous study revealed that the rate capability was dominated by the mesopore/micropore volume ratio [11, 47]. As shown in Figure S10, the trend of rate performance for KAC-based materials was in overall consistent with that of the V_{mes}/V_{mic} values. The improved amount of mesopores in KAC-900 and KAC-4 served as ion transportation channels from the solution to the active surface of micropores, which guaranteed the smooth charge transfer at high-charge density [48]. Besides, the overall good rate performance of other KAC samples without much mesopores can be explained by the existence of large micropores sized at ~1.20 and ~1.59 nm, which were reported to facilitate the ion

diffusion process such as mesopores [27, 49]. The high graphitization degree gave rise to good conductivity of KAC materials, therefore leading to fast electron transport with low resistance. Furthermore, the EIS measurement provided deeper insight into the impedance referring to the ion diffusion and charge transfer. The Nyquist plots of KAC samples (Figures 5(d) and 6(d)) consisted of a semicircle at the high frequency with the real-axis intercept, followed by the Warburg resistance in the mid-to-high frequency region and a steep line in the low-frequency region. The small value of the intercept indicated the low equivalent series resistance (ESR), which was in good agreement with the negligible IR drop in the discharging curves of all the KAC samples [15, 50]. The semicircle diameter corresponded to the charge transfer resistance (R_{ct}) [46]. KAC-900 and KAC-4 showed very low R_{ct} value of ~0.11 and ~0.30 Ohm, respectively. Moreover, the shorter projected length of the 45° Warburg diffusion line of KAC-900 and KAC-4 confirmed the reduced diffusion resistance of electrolyte ions owing to the mesopores and large micropores with high pore volume and graphene layers' pathways with large layer distance [37]. The above results confirmed the high capacitance retention of KAC-900 and KAC-4 at high rate. Notably, the extended spike in the low frequency was typical of capacitive behavior. The closer the straight line to 90°, the better the capacitive performance [51, 52]. By combining pore structure characterization and EIS test, the tendency of specific capacitance and rate capability of KAC samples can be well understood. Our results were compared with previous studies, and the detailed literature review of the specific capacitance is shown in Table S3.

To evaluate the cycling stability of such Konjac-derived carbon materials, charge-discharge performance was tested on KAC-700 under 5 A/g for 2000 cycles. Figure 7 demonstrates a very good cycling performance with 99.6% retention of the initial capacitance. The slight increased capacitance arose from the activation of surface in the early stage of the charge-discharge process. The inset images showed the stable charge/discharge curves from the very beginning to the last few cycles. The superior long-range cycling performance confirmed that KAC-based samples were excellent electrode materials for the applications of high-efficient and stable supercapacitors.

Above all, KAC-700 exhibited the highest specific capacitance while KAC-900 and KAC-4 showed the best rate capability among the series of KAC materials. Combining structure and composition analysis, the dependence of the capacitive performance on the texture properties and chemical composition can be revealed as follows. For KAC-700, the highest microporous volume ($0.94 cm^3/g$) provided plentiful active sites for ion storage. The optimized sub-nanopore (~0.68 nm) further boosts the capacitance. The relatively low carbonization temperature maintained large amount of O and trace N, giving rise to additive pseudo-capacitance. For KAC-900 and KAC-4, high activation temperature and KOH dose introduced large amount of mesopores of 2.76 and 3.42 nm with narrow distribution, which act as the ion transfer channels and reduce the diffusion resistance. The volume ratio between mesopores and

(a)

(b)

(c)

(d)

FIGURE 5: Electrochemical performance of KAC-700, 800, and 900 in 1 M H_2SO_4 aqueous solution. (a) CV curves at the scan rate of 5 mV/s, (b) GCD curves at 0.5 A/g, (c) specific capacitances under different current densities calculated from GCD data, and (d) Nyquist plots of the achieved samples, the inset images show enlarged impedance at the high frequency and the equivalent circuit.
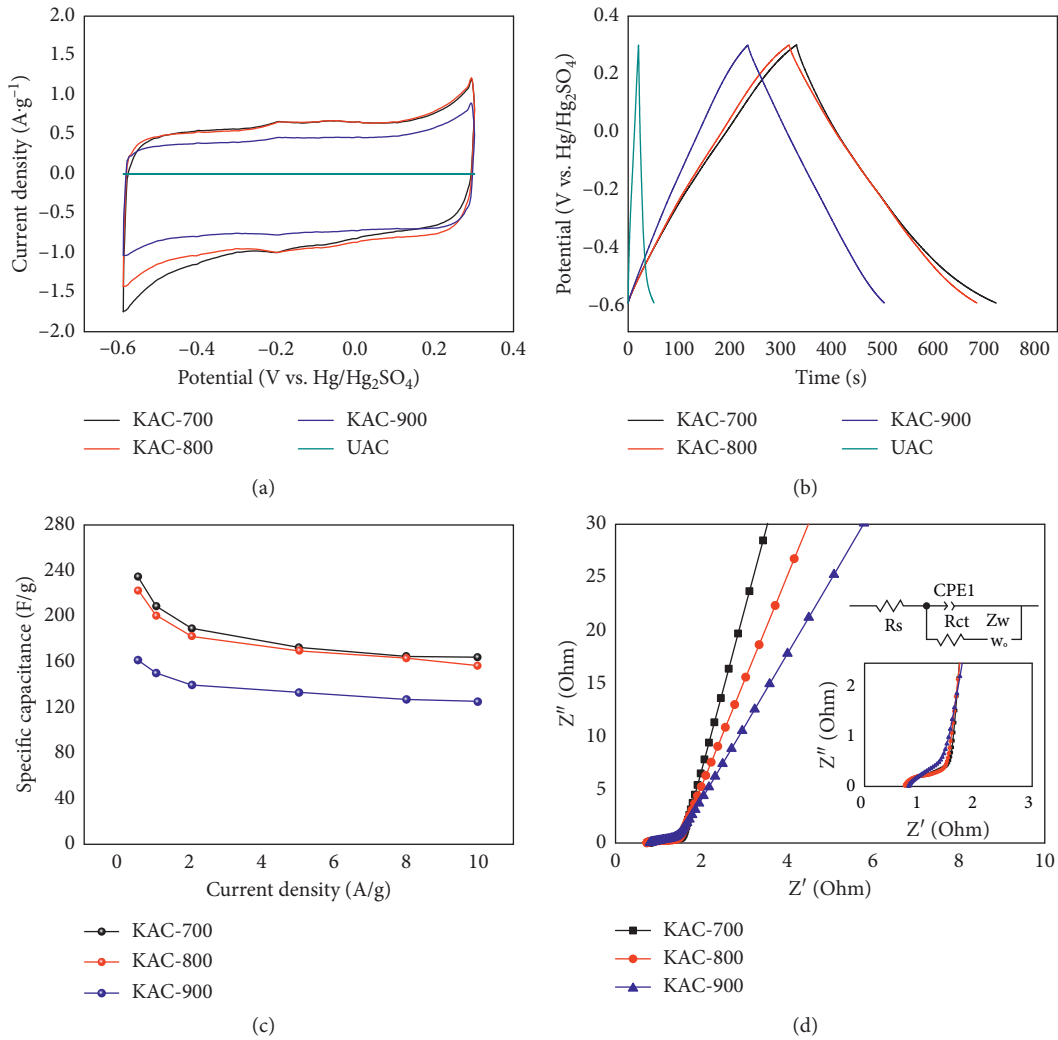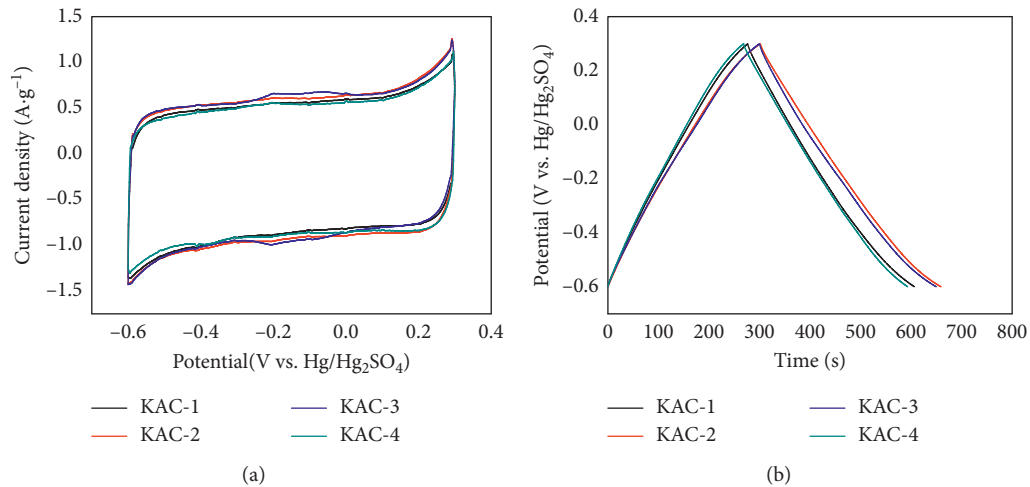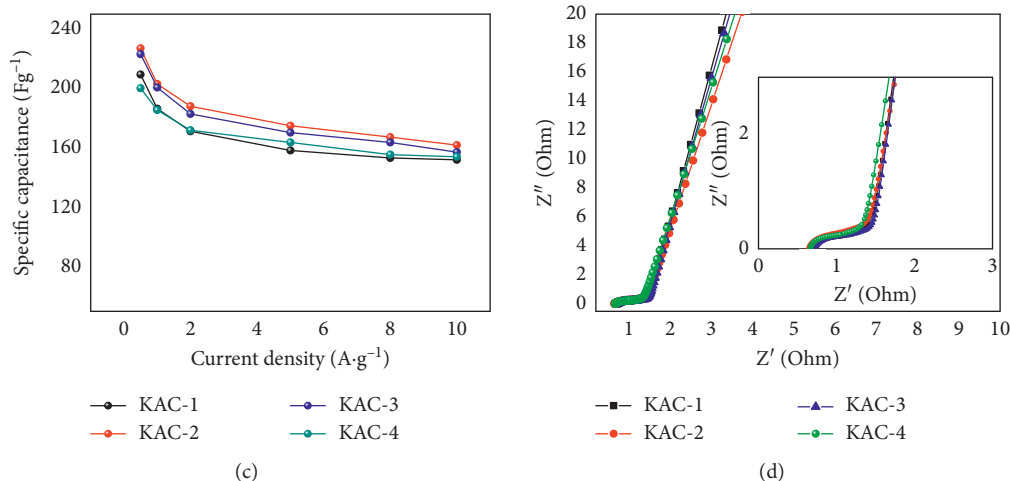

(a)

(b)

FIGURE 6: Continued.

(c)

(d)

FIGURE 6: Electrochemical performance of KAC-1, 2, 3, and 4 in 1 M H_2SO_4 aqueous solution. (a) CV curves at the scan rate of 5 mV/s, (b) GCD curves at 0.5 A/g, (c) specific capacitances under different current densities calculated from GCD data, and (d) Nyquist plots of the achieved samples, the inset images showed enlarged impedance at the high frequency.
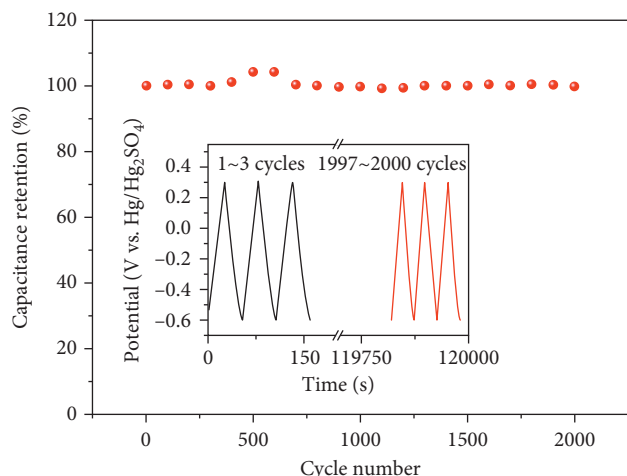

FIGURE 7: Cycling performance of KAC-700 under 5 A/g for 2000 cycles. The inset image shows the GCD curves in the first and last 3 cycles.

micropores is elevated compared with other KAC counterparts, indicating the better rate ability. The decreased O content and improved electrical conductivity benefit the charge transport especially at the high rate.

4. Conclusions

In summary, we have prepared the hierarchically porous ACs from the Konjac sponge precursor. Upon KOH activation, the KAC samples inherit the lamellar morphology of the raw materials and possess coexisted micro/mesopores with narrow size distribution. Remarkably, graphene-like layers are observed in KAC-based samples, with the stacking distance comparable to the size of the electrolyte ion. KAC-700 with rich O doping showed the highest specific capacitance owing to the largest ion accessible microporous volume with the optimized pore size. KAC-900 and KAC-4

possessed superior rate capability with the plentiful mesopores. Taking KAC-700 as an example, excellent cycling stability was obtained with only 0.4% decay of original capacitance under the current density of 5 A/g. The abundant source and simple synthetic procedure guarantee the scale-up production of such KAC materials, which would become novel and promising electrode materials for SC devices. The results achieved in this study can serve as guidance for the design and development of ACs with desirable porous structure, graphitized microstructure, and high SC performance.

Data Availability

The data used to support the findings of this study are available from the corresponding author upon request.

Conflicts of Interest

The authors declare that they have no conflicts of interest.

Acknowledgments

Supplementary Materials

Figure S1. TEM images of UAC samples under different magnifications. Figure S2. Transmission electron microscopy (TEM) images of (a and d) KAC-1, (b and e) KAC-2 and (c and f) KAC-4. Figure S3. Transmission electron microscopy (TEM) images of (a) KAC-700, (b) KAC-800 and (c) KAC-900, with the related digital micrograph showing the lateral distance information, the numbers demonstrated the lateral distance in the selected area, scale bar = 10 nm. Figure S4. TEM images of (a) KAC-1,

(b) KAC-2 and (c) KAC-4, with the related digital micrograph showing the lateral distance information, the numbers demonstrated the lateral distance in the selected area, scale bar = 10 nm. Fig S5. Selected-area electron diffraction pattern of (a) KAC-700 and (b) KAC-4. Figure S6. O1s spectra of KAC based samples. Figure S7. CV curves of KAC based materials under scan rates of 1 mV/s, 5 mV/s, 10 mV/s, 20 mV/s, 50 mV/s, 100 mV/s. Figure S8. GCD curves of KAC based materials under the current densities of 0.5 A/g, 1 A/g, 2 A/g, 5 A/g, 8 A/g and 10 A/g. Figure S9. GCD curves (a) and the calculated specific capacitance (b) of UAC sample under different current densities. Figure S10. The microporous specific surface area (SSAmic) based on DFT model (Left Y axis), the microporous volume and ratio between mesoporous and microporous volume (Vmes/Vmic) (Right Y axis) of KAC based samples. Table S1. Elemental analysis results (atomic%) based XPS data. Table S2. The specific capacitance calculated from the discharging curves of KAC based samples and the capacitance retention under 10 A/g compared with that of 0.5 A/g. Table S3. Specific capacitance of KAC based matetials using three-electrode cells reported in literatures. (*Supplementary Materials*)

References

[1] P. Simon and Y. Gogotsi, "Materials for electrochemical capacitors," *Nature Materials*, vol. 7, no. 11, pp. 845–854, 2008.

[2] Y. Wang, Y. Song, and Y. Xia, "Electrochemical capacitors: mechanism, materials, systems, characterization and applications," *Chemical Society Reviews*, vol. 45, no. 21, pp. 5925–5950, 2016.

[3] S. Dutta, A. Bhaumik, and K. C. W. Wu, "Hierarchically porous carbon derived from polymers and biomass: effect of interconnected pores on energy applications," *Energy and Environmental Science*, vol. 7, no. 11, pp. 3574–3592, 2014.

[4] B. E. Conway, *Electrochemical Supercapacitors: Scientific Fundamentals and Technological Applications*, Springer Science & Business Media, Berlin, Germany, 2013.

[5] H. Ji, X. Zhao, Z. Qiao et al., "Capacitance of carbon-based electrical double-layer capacitors," *Nature Communications*, vol. 5, no. 1, p. 3317, 2014.

[6] M. Yang, Y. Zhong, J. Bao et al., "Achieving battery-level energy density by constructing aqueous carbonaceous supercapacitors with hierarchical porous N-rich carbon materials," *Journal of Materials Chemistry A*, vol. 3, no. 21, pp. 11387–11394, 2015.

[7] J. Y. Hwang, M. Li, M. F. El-Kady, and R. B. Kaner, "Next-generation activated carbon supercapacitors: a simple step in electrode processing leads to remarkable gains in energy density," *Advanced Functional Materials*, vol. 27, no. 15, article 1605745, 2017.

[8] Z. Zhitao, W. Lie, L. Yiming et al., "Nitrogen-doped core-sheath carbon nanotube array for highly stretchable supercapacitor," *Advanced Energy Materials*, vol. 7, no. 5, article 1601814, 2017.

[9] J. Li, J. Tang, J. Yuan et al., "Enlarging energy density of supercapacitors using unequal graphene electrodes and ionic liquid electrolyte," *Electrochimica Acta*, vol. 258, pp. 1053–1058, 2017.

[10] R. R. Salunkhe, Y. Kamachi, N. L. Torad et al., "Fabrication of symmetric supercapacitors based on MOF-derived nanoporous carbons," *Journal of Materials Chemistry A*, vol. 2, no. 46, pp. 19848–19854, 2014.

[11] J. Yang, H. Wu, M. Zhu et al., "Optimized mesopores enabling enhanced rate performance in novel ultrahigh surface area meso-/microporous carbon for supercapacitors," *Nano Energy*, vol. 33, pp. 453–461, 2017.

[12] M. Oschatz, S. Boukhalfa, W. Nickel et al., "Carbide-derived carbon aerogels with tunable pore structure as versatile electrode material in high power supercapacitors," *Carbon*, vol. 113, pp. 283–291, 2017.

[13] B. Li, F. Dai, Q. Xiao et al., "Nitrogen-doped activated carbon for a high energy hybrid supercapacitor," *Energy and Environmental Science*, vol. 9, no. 1, pp. 102–106, 2016.

[14] T. Liu, F. Zhang, Y. Song, and Y. Li, "Revitalizing carbon supercapacitor electrodes with hierarchical porous structures," *Journal of Materials Chemistry A*, vol. 5, no. 34, pp. 17705–17733, 2017.

[15] K. Lee, Y. Yoon, Y. Cho et al., "Tunable sub-nanopores of graphene flake interlayers with conductive molecular linkers for supercapacitors," *ACS Nano*, vol. 10, no. 7, pp. 6799–6807, 2016.

[16] B. François, P. Volker, B. Andrea, and F. Elzbieta, "Carbons and electrolytes for advanced supercapacitors," *Advanced Materials*, vol. 26, no. 14, pp. 2219–2251, 2014.

[17] H. Liu, H. Song, X. Chen, S. Zhang, J. Zhou, and Z. Ma, "Effects of nitrogen- and oxygen-containing functional groups of activated carbon nanotubes on the electrochemical performance in supercapacitors," *Journal of Power Sources*, vol. 285, pp. 303–309, 2015.

[18] Y. Li, G. Wang, T. Wei, Z. Fan, and P. Yan, "Nitrogen and sulfur co-doped porous carbon nanosheets derived from willow catkin for supercapacitors," *Nano Energy*, vol. 19, pp. 165–175, 2016.

[19] B. Chang, W. Shi, S. Han et al., "N-rich porous carbons with a high graphitization degree and multiscale pore network for boosting high-rate supercapacitor with ultrafast charging," *Chemical Engineering Journal*, vol. 350, pp. 585–598, 2018.

[20] C. Xue, F. Yang, E. Wang et al., "Nanosized graphitic carbon with balanced micro/mesoporosity for robust supercapacitor with superior volumetric capacitance and cyclic performance," *Electrochimica Acta*, vol. 271, pp. 406–416, 2018.

[21] A. M. Abioye and F. N. Ani, "Recent development in the production of activated carbon electrodes from agricultural waste biomass for supercapacitors: a review," *Renewable and Sustainable Energy Reviews*, vol. 52, pp. 1282–1293, 2015.

[22] X. Tian, H. Ma, Z. Li et al., "Flute type micropores activated carbon from cotton stalk for high performance supercapacitors," *Journal of Power Sources*, vol. 359, pp. 88–96, 2017.

[23] G. Zhao, C. Chen, D. Yu et al., "One-step production of O-N-S co-doped three-dimensional hierarchical porous carbons for high-performance supercapacitors," *Nano Energy*, vol. 47, pp. 547–555, 2018.

[24] X. Teng, C. Ma, C. Ge et al., "Green synthesis of nitrogen-doped carbon dots from konjac flour with "off-on" fluorescence by Fe^{3+} and l-lysine for bioimaging," *Journal of Materials Chemistry B*, vol. 2, pp. 4631–4639, 2014.

[25] L. H. Cheng, A. Abd Karim, M. H. Norziah, and C. C. Seow, "Modification of the microstructural and physical properties of konjac glucomannan-based films by alkali and sodium carboxymethylcellulose," *Food Research International*, vol. 35, no. 9, pp. 829–836, 2002.

[26] Q. Li, X. Bai, Q. Meng et al., "Porous biochar generated from natural Amorphophallus konjac for high performance

supercapacitors," *Applied Surface Science*, vol. 448, pp. 16–22, 2018.

[27] J. Hou, K. Jiang, R. Wei et al., "Popcorn-derived porous carbon flakes with an ultrahigh specific surface area for superior performance supercapacitors," *ACS Applied Materials and Interfaces*, vol. 9, no. 36, pp. 30626–30634, 2017.

[28] H. Zhu, F. Shen, W. Luo et al., "Low temperature carbonization of cellulose nanocrystals for high performance carbon anode of sodium-ion batteries," *Nano Energy*, vol. 33, pp. 37–44, 2017.

[29] Y. Zhu, S. Murali, M. D. Stoller et al., "Carbon-based supercapacitors produced by activation of graphene," *Science*, vol. 332, no. 6037, pp. 1537–1541, 2011.

[30] E. Raymundo-Piñero, P. Azaïs, T. Cacciaguerra et al., "KOH and NaOH activation mechanisms of multiwalled carbon nanotubes with different structural organisation," *Carbon*, vol. 43, no. 4, pp. 786–795, 2005.

[31] A. Sadezky, H. Muckenhuber, H. Grothe, R. Niessner, and U. Pöschl, "Raman microspectroscopy of soot and related carbonaceous materials: spectral analysis and structural information," *Carbon*, vol. 43, no. 8, pp. 1731–1742, 2005.

[32] X. Gao, W. Xing, J. Zhou et al., "Superior capacitive performance of active carbons derived from Enteromorpha prolifera," *Electrochimica Acta*, vol. 133, pp. 459–466, 2014.

[33] C. Emmenegger, P. Mauron, P. Sudan et al., "Investigation of electrochemical double-layer (ECDL) capacitors electrodes based on carbon nanotubes and activated carbon materials," *Journal of Power Sources*, vol. 124, no. 1, pp. 321–329, 2003.

[34] L. Shi-Yu, J. Meng, Z. Yan et al., "Chemically exfoliating biomass into a graphene-like porous active carbon with rational pore structure, good conductivity, and large surface area for high-performance supercapacitors," *Advanced Energy Materials*, vol. 8, no. 11, article 1702545, 2018.

[35] I. K. Moon, J. Lee, R. S. Ruoff, and H. Lee, "Reduced graphene oxide by chemical graphitization," *Nature Communications*, vol. 1, no. 6, p. 73, 2010.

[36] H. J. Denisa, S. Mykola, L. G. Qing, and B. T. J., "Combined effect of nitrogen- and oxygen-containing functional groups of microporous activated carbon on its electrochemical performance in supercapacitors," *Advanced Functional Materials*, vol. 19, no. 3, pp. 438–447, 2009.

[37] C. Wang, D. Wu, H. Wang et al., "A green and scalable route to yield porous carbon sheets from biomass for supercapacitors with high capacity," *Journal of Materials Chemistry A*, vol. 6, no. 3, pp. 1244–1254, 2018.

[38] B. Han, G. Cheng, E. Zhang, L. Zhang, and X. Wang, "Three dimensional hierarchically porous ZIF-8 derived carbon/LDH core-shell composite for high performance supercapacitors," *Electrochimica Acta*, vol. 263, pp. 391–399, 2018.

[39] C. Pean, B. Daffos, B. Rotenberg et al., "Confinement, desolvation, and electrosorption effects on the diffusion of ions in nanoporous carbon electrodes," *Journal of the American Chemical Society*, vol. 137, no. 39, pp. 12627–12632, 2015.

[40] M. Salanne, B. Rotenberg, K. Naoi et al., "Efficient storage mechanisms for building better supercapacitors," *Nature Energy*, vol. 1, no. 6, article 16070, 2016.

[41] M. Endo, T. Maeda, T. Takeda et al., "Capacitance and pore-size distribution in aqueous and nonaqueous dielectrolytes using various activated carbon electrodes," *Journal of the Electrochemical Society*, vol. 148, no. 8, pp. A910–A914, 2001.

[42] D. Hulicova, M. Kodama, and H. Hatori, "Electrochemical performance of nitrogen-enriched carbons in aqueous and non-aqueous supercapacitors," *Chemistry of Materials*, vol. 18, no. 9, pp. 2318–2326, 2006.

[43] K. Urita, C. Urita, K. Fujita et al., "The ideal porous structure of EDLC carbon electrodes with extremely high capacitance," *Nanoscale*, vol. 9, no. 40, pp. 15643–15649, 2017.

[44] J. Hou, C. Cao, F. Idrees, and X. Ma, "Hierarchical porous nitrogen-doped carbon nanosheets derived from silk for ultrahigh-capacity battery anodes and supercapacitors," *ACS Nano*, vol. 9, no. 3, pp. 2556–2564, 2015.

[45] B. Liu, M. Yang, H. Chen et al., "Graphene-like porous carbon nanosheets derived from salvia splendens for high-rate performance supercapacitors," *Journal of Power Sources*, vol. 397, pp. 1–10, 2018.

[46] L. Sun, C. Tian, M. Li et al., "From coconut shell to porous graphene-like nanosheets for high-power supercapacitors," *Journal of Materials Chemistry A*, vol. 1, no. 21, pp. 6462–6470, 2013.

[47] M. Zhi, F. Yang, F. Meng et al., "Effects of pore structure on performance of an activated-carbon supercapacitor electrode recycled from scrap waste tires," *ACS Sustainable Chemistry and Engineering*, vol. 2, no. 7, pp. 1592–1598, 2014.

[48] H. Zhang, X. Zhang, and Y. Ma, "Enhanced capacitance supercapacitor electrodes from porous carbons with high mesoporous volume," *Electrochimica Acta*, vol. 184, pp. 347–355, 2015.

[49] W. Li, J. Liu, and D. Zhao, "Mesoporous materials for energy conversion and storage devices," *Nature Reviews Materials*, vol. 1, no. 6, article 16023, 2016.

[50] S. Yang, X. Wu, C. Chen et al., "Spherical [α]-Ni(OH)$_2$ nanoarchitecture grown on graphene as advanced electrochemical pseudocapacitor materials," *Chemical Communications*, vol. 48, no. 22, pp. 2773–2775, 2012.

[51] Y. Lu, S. Zhang, J. Yin et al., "Mesoporous activated carbon materials with ultrahigh mesopore volume and effective specific surface area for high performance supercapacitors," *Carbon*, vol. 124, pp. 64–71, 2017.

[52] H. Feng, H. Hu, H. Dong et al., "Hierarchical structured carbon derived from bagasse wastes: a simple and efficient synthesis route and its improved electrochemical properties for high-performance supercapacitors," *Journal of Power Sources*, vol. 302, pp. 164–173, 2016.

Research Article

Effect of Functionalized Carbon Nanotubes in the Detection of Benzene at Room Temperature

Nurjahirah Janudin (ID),[1] **Norli Abdullah,**[2] **Wan Md Zin Wan Yunus,**[3] **Faizah Md Yasin,**[4] **Mohd Hanif Yaacob,**[5] **Norshafiqah Mohamad Saidi,**[1] **and Noor Azilah Mohd Kasim** (ID)[1]

[1]*Department of Defence Science, Faculty of Defence Science and Technology, National Defence University of Malaysia, Kem Sg. Besi, 57000 Kuala Lumpur, Malaysia*
[2]*Department of Chemistry/Biology, Centre for Defence Foundation Studies, National Defence University of Malaysia, Kem Sg. Besi, 57000 Kuala Lumpur, Malaysia*
[3]*Centre for Tropicalisation (CENTROP), National Defence University of Malaysia, Kem Sg. Besi, 57000 Kuala Lumpur, Malaysia*
[4]*Department of Chemical and Environmental Engineering, Faculty of Engineering, Universiti Putra Malaysia, Serdang 43400, Malaysia*
[5]*Wireless and Photonics Network Research Centre (WiPNET), Universiti Putra Malaysia, Serdang 43400, Selangor, Malaysia*

Correspondence should be addressed to Noor Azilah Mohd Kasim; azilah@upnm.edu.my

In this paper, carbon nanotubes (CNTs) were functionalized by acid treatment and further functionalized with dodecylamine and were designated as CNT-carboxylic and CNT-amide, respectively. Then, functionalized CNTs produced were characterized with various methods to verify the attachment of a functional group. Performance of the functionalized CNTs in the detection of benzene gas was monitored at room temperature. The sample was dropped cast on the interdigitated transducer (IDT), and the changes in resistivity were recorded by a digital multimeter in a customized chamber under controlled humidity (~55%) environment. Based on the findings, it showed that the functionalized CNTs provide an extra active area for interaction between the gas analyte and CNTs, thus increasing their response and improving the sensitivity of the sensing material.

1. Introduction

Benzene, C_6H_6, is an important organic chemical compound that consists of six carbon atoms each bonded covalently with one hydrogen atom. One of the main uses of benzene is an intermediate in synthesizing other chemicals such as nitrobenzene, cumene, ethylbenzene, aniline, and cyclohexane. For example, ethylbenzene becomes a precursor of styrene, which is used in the production of polymers and plastics such as polystyrene (PS) and expanded polystyrene (EPS) [1]. Benzene has carcinogenic properties, which are well known for many years. United States Occupational Safety and Health Administration (U.S. OSHA) has set the limit of exposure in the workplace as 1 part per million (ppm) in 8-hour workday and 40-hour workweek [2]. U.S. OSHA has also fixed an action level of 0.5 ppm of benzene concentration in order to encourage lower exposure in the workplace [3].

Generally, benzene is detected using several techniques such as gas chromatography [4], mass spectrometry [5, 6], ion mobility spectrometry [7], and ultraviolet spectrophotometry [8, 9]. Even though the instruments are sensitive and produce results fast, they are bulky and not portable. Therefore, miniature gas sensors become the main interest in the detection of benzene [10–12] to overcome these obstacles. An excellent miniature gas sensor requires high sensitivity, fast response, high selectivity, and reproducibility [13]. Although sensing materials such as semiconductor metal oxides (SMO) have good performance, they need more power and have low selectivity.

Nanomaterials are a good candidate for sensing material because of their low power consumption and good chemical

selectivity [14]. Since its discovery by Ijima [15], carbon nanotubes (CNTs) have extensive application especially in the gas sensor field due to their nanosize and large surface area ratio which are important for the interaction between the gas analyte and CNTs. However, their uneven structure and agglomerations properties have limited their potential and make them less sensitive and selective [16]. Modification of the CNTs with functional groups [17], polymers [18], and metal oxide nanoparticles [19] is one of the several ways utilized to improve the compatibility of CNTs.

Modification of CNTs with various functional groups changes their electronic property, thus enhancing their selectivity and increasing their response towards specific gases. Noteworthy, the interaction of target molecules with a different functional group varies significantly [20]. Mainly, the CNTs is modified with a carboxylic group. The carboxylic group will create reactive sites at the sidewalls and end of the CNTs where vigorous interaction with target molecules happens. For example, it was shown [21] that single-walled carbon nanotubes attached with carboxylic (SWCNT-carboxylic) showed good repeatability and better response towards a mixture of 10 ppm carbon monoxide, CO, and ammonia, NH_3 gas. SWCNT-carboxylic demonstrated faster response towards CO than NH_3 gas. Other than that, the sensor synthesized from multi-walled CNTs functionalized with acid (MWCNT-carboxylic) was sensitive to hydrogen (H_2) gas with a detection limit of 0.05%, whereas pristine MWCNTs showed poor response to this gas [22]. The recovery time of the MWCNT-carboxylic sensor decreases to 100 s for 0.05% of H_2 gas as compared to 190 s for the pristine MWCNT. Leghrib et al. have developed a microsensor array for detection of benzene at room temperature by using plasma-treated multiwalled CNTs decorated with rhodium (Rh), palladium (Pd), gold (Au), or nickel (Ni). This sensor showed good sensitivity with the detection limit of benzene below 50 parts per billion (ppb) [10]. Also, a gas preconcentrator based on three different types of CNTs which is multiwalled, double-walled, and single-walled carbon nanotubes (MWCNTs, DWCNTs, and SWCNTs) was fabricated for efficient detection of benzene [23]. The results showed that MWCNTs produced via arc discharge displayed a good performance as the injector unit for the application in a gas preconcentrator.

In this paper, the functionalized CNTs were treated with sulphonitric mixture [24] and used as reaction precursor for amide functionalization by using dodecylamine as the functionalizing reactant. The surface morphology of the CNTs before and after functionalizing was examined by field emission-scanning electron microscopy attachment with energy dispersive X-Ray analysis (FESEM-EDX), and functional group attachment was confirmed by using Fourier Transform-Infrared spectroscopy (FT-IR). Then, the potential of the functionalized CNTs in the detection of benzene gas compared to the pristine CNTs and the effect of functionalization were studied by observing the changes in the resistivity of CNTs when exposed to benzene gas.

2. Methodology

2.1. Materials. Sulphuric acid (H_2SO_4, 98%), dodecylamine ($CH_3(CH_2)_{11}NH_2$, 99%), and nitric acid (HNO_3, 65%) were purchased from Merck Company (Germany). Carbon nanotubes (purity: 95%; type: multiwalled; inner diameter, ID: 5–10 nm) with a length of 10–30 μm were obtained from Nanostructured & Amorphous Materials, Inc (USA). All the chemical reagents were used without any purification and in analytical grade. For detection of benzene, benzene vapours in 100 ppm mixed with nitrogen gas were obtained from AGS Scientific Company (Singapore).

2.2. Carboxylic and Amide Functionalization of CNT. In a small beaker, 2.0 g of pristine CNTs was added to 3 : 1 H_2SO_4/HNO_3 (sulphonitric mixture) and sonicated with ultrasonication water bath for 2 hours at 70°C. After the treatment was done, the functionalized CNTs was filtered and washed repeatedly until the product reached pH 7 before drying for 24 hours in a vacuum oven [24]. This functionalized CNTs was labeled CNT-carboxylic.

For amide functionalization, dodecylamine was melted on a hotplate for half an hour at 80°C. As soon as the reactant melted fully, CNT-carboxylic was added and sonicated at the same temperature for a while before adding few drops of H_2SO_4 as a catalyst. The sonication process was continued for 5 hours. Finally, the product was filtered and washed several times until it reached pH 7 before drying for 24 hours in the vacuum oven. This functionalized CNTs was labeled CNT-amide. All the functionalized CNTs were characterized using FESEM-EDX and FT-IR analyses as well to ensure the favourable outcome in the attachment of carboxylic (-COOH) and amide (-CONH_2) functional groups on the CNTs.

2.3. Detection of Benzene by CNT. The pristine and functionalized CNTs were diluted in distilled water and sonicated for 30 minutes at 40°C. Then, by using a micropipette, 2.5 μL of the CNTs was dropped cast onto an interdigitated transducer (IDT) and dried for 30 minutes in the oven. Electrical contact was made by connecting two gold wires on the IDT and baked again in the oven for 30 minutes. IDT with the sample was placed in the customized chamber and connected to a digital multimeter to record the resistance changes. Benzene was injected 5 minutes alternately with nitrogen gas (as carrier gas) at the concentration from 0.125% to 1% at room temperature under controlled humidity environment (~55%). Resistance changes versus time were plotted to analyze the effect of functionalization of the CNTs on the detection of benzene. Other than that, the sensitivity of the CNTs also was calculated and plotted to compare the sensitivity of the pristine CNTs and the functionalized CNTs.

3. Results and Discussion

3.1. Characterization of Carboxylic and Amide Functionalization of CNT. Surface morphology and elemental composition of the functionalized CNTs were investigated by FESEM-EDX (JEOL 7600F; Institute of Bioscience, Universiti Putra Malaysia) with an accelerating voltage of 5.0 kV. Figures 1(a)–1(c) show the distinctive images of CNTs and
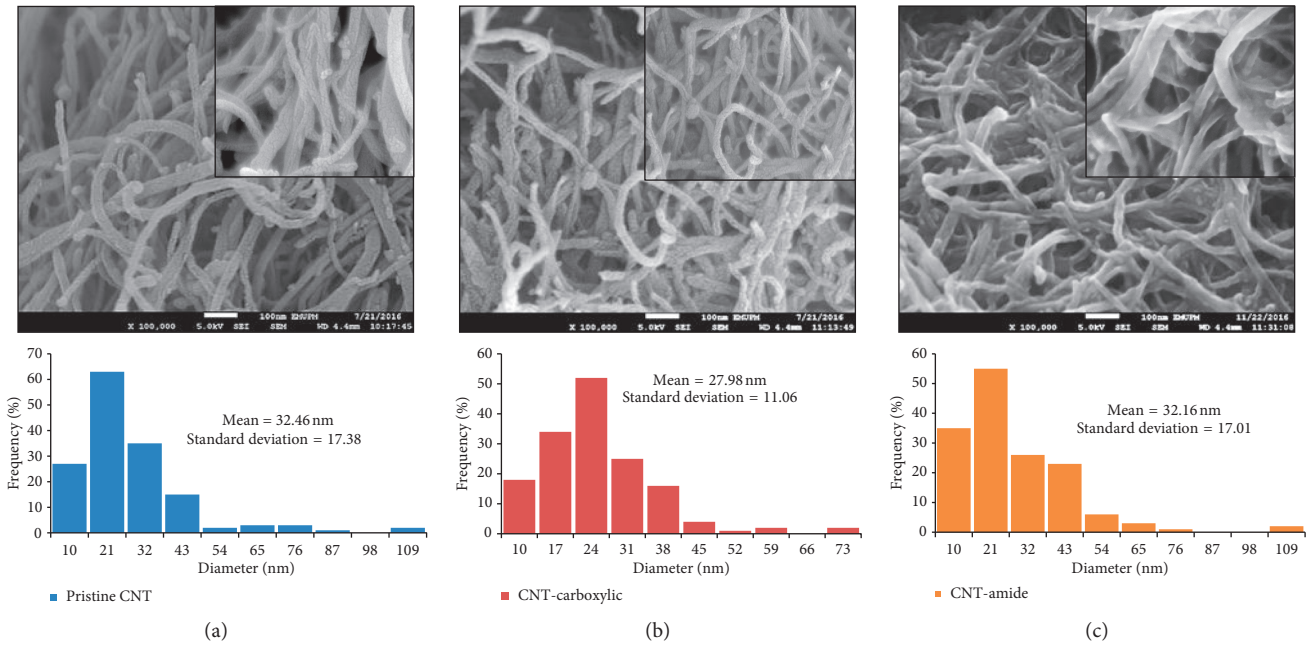
Figure 1: Micrographs of (a) pristine CNT, (b) CNT-carboxylic, and (c) CNT-amide.

their corresponding diameter size-distribution histogram. The pristine CNTs showed quite smooth structure compared to the functionalized CNTs. It is clearly shown in the insert images of Figures 1(a)–1(c) that the morphology of functionalized CNTs seems to be rough due to the treatment of acid during the functionalization process [25]. Diameter distribution of the pristine CNTs was in the range of 10 nm to 109 nm, and the mean diameter was 32.46 nm with a standard deviation of 17.38. Meanwhile, the functionalized CNTs are more aligned and dense caused by insertion of a new functional group [26]. Diameter distribution of CNT-carboxylic was decreased which was in the range of 10 to 73 nm, and the mean diameter was 27.98 nm with a standard deviation of 11.06, and diameter distribution of CNT-amide was slightly decreased which was in the range of 10 to 109 nm, and the mean diameter was 32.16 nm with a standard deviation of 17.01. The standard deviation of the functionalized CNTs samples was rather large, indicating that the diameter of the CNTs is inconsistent. In the functionalization process, the attachment of carboxylic (-COOH) and amide (-CONH$_2$) groups with the carbon-carbon double bond (C=C) of the CNTs depends on the stearic factor. Because of this effect, it is difficult to achieve a uniform functionalization; therefore, the diameter of the functionalized CNTs is inconsistent as expected. Thus, considering that the diameter alteration is caused by new functional groups [27], the elemental composition analysis has strengthened the result by showing an increase of oxygen element percentage and appearance of the nitrogen element (Table 1) as well.

The transformation produced by the insertion of new functional groups on the surface of the CNTs was qualitatively identified by using FT-IR spectroscopy (Figure 2). Table 2 shows the intensity of peaks appeared in the FT-IR spectra for all samples. All spectra showed bands at

Table 1: Elemental composition of pristine and functionalized CNTs.

Sample	Element (%)		
	C	O	N
Pristine CNT	97.02	2.98	—
CNT-carboxylic	92.84	7.19	—
CNT-amide	85.80	7.74	6.46

approximately 1640 cm^{-1} and 3100 cm^{-1}, which correlate with the C=C and O-H stretching vibrations, respectively [28]. The FT-IR spectrum of CNT-carboxylic showed the occurrence of a band at 1880 cm^{-1}, which is associated with the stretching of carbonyl from the carboxylic acid group. Moreover, an increase in the intensity of the band at 2880 cm^{-1} compared with the pristine CNTs spectrum confirmed the attachment of the carboxylic acid group (Table 2). According to a previous study [29], the hydroxyl and carboxyl groups that attached during the modification of CNTs with sulphonitric mixture were contributed to this increment. After CNT-carboxylic was further functionalized with an amine, bands at 1650, 1404, and 3300 cm^{-1} were discovered in the spectrum, which may be designated to C=O (amides), N-H bending, and N-H stretching, respectively [30]. Thus, the FT-IR spectrum of CNT-amide confirms that the surface of CNT-carboxylic was accomplished, treated by the amide functional groups.

3.2. Detection of Benzene by CNT.
Figure 3 shows resistance changes of CNTs when exposed to benzene gas with different concentrations at room temperature. As reported by Leghrib et al. [31], functionalized CNTs have good response towards benzene. Basically, detection of benzene is related to transfer of electron charges between the gas analyte and sensing materials,
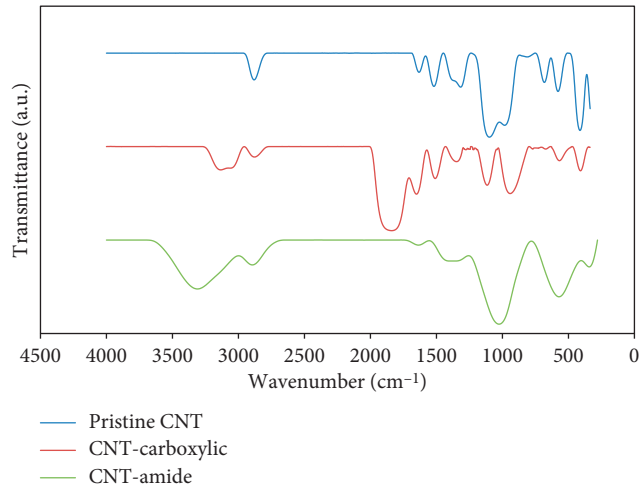
Figure 2: FT-IR spectra of (a) pristine CNT, (b) CNT-carboxylic, and (c) CNT-amide.

Table 2: Intensity of peaks appeared in pristine CNT, CNT-carboxylic, and CNT-amide.

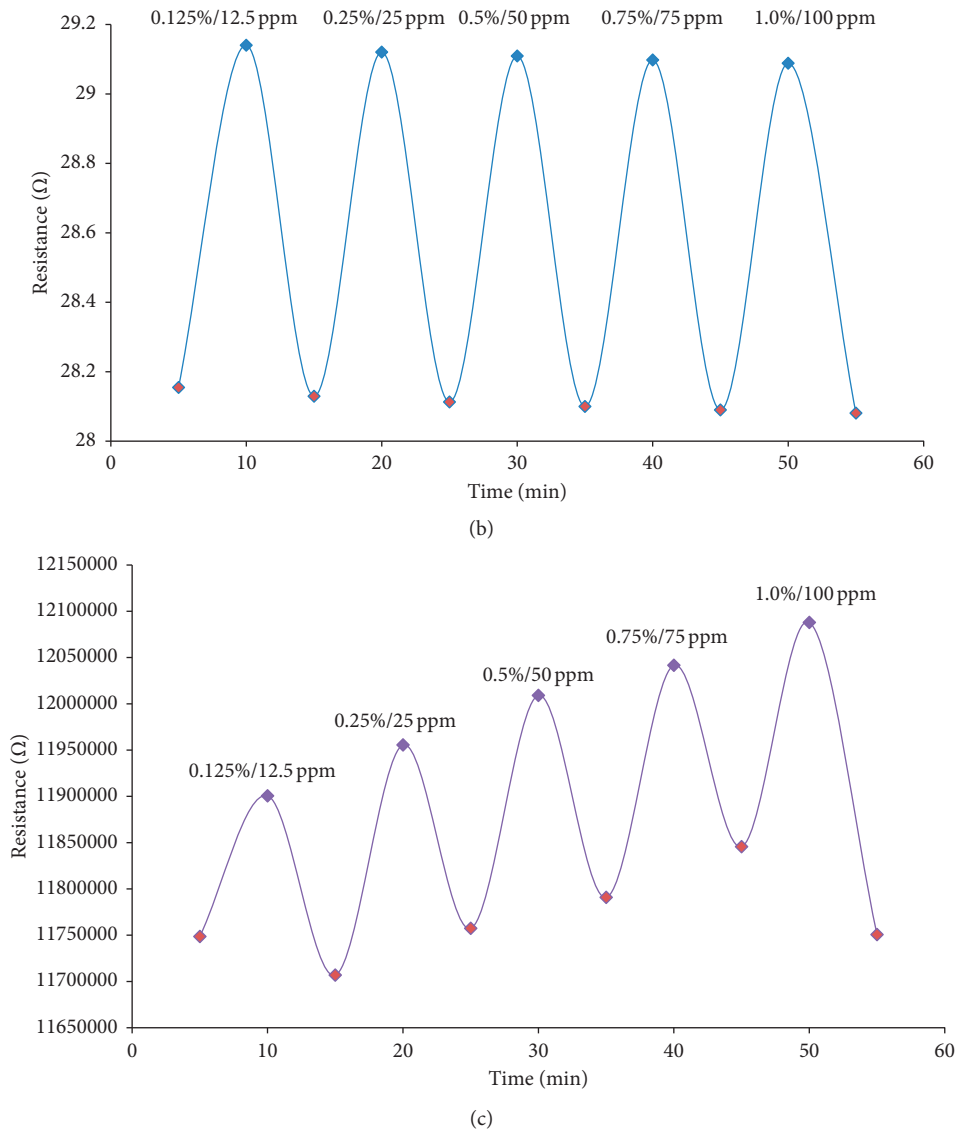| Sample	Peak (cm^{-1}) (bond)	Intensity (%)
Pristine CNT	1640 (C=C)	88
	2880 (C=O carboxyl)	74
CNT-carboxylic	1640 (C=C)	54
	1880 (C=O carbonyl)	12
	3100 (O-H)	78
	2880 (C=O carboxyl)	89
CNT-amide	1650 (C=O amide)	98
	1404 (N-H bending)	79
	2880 (C=O carboxyl)	81
	3300 (N-H stretching)	57
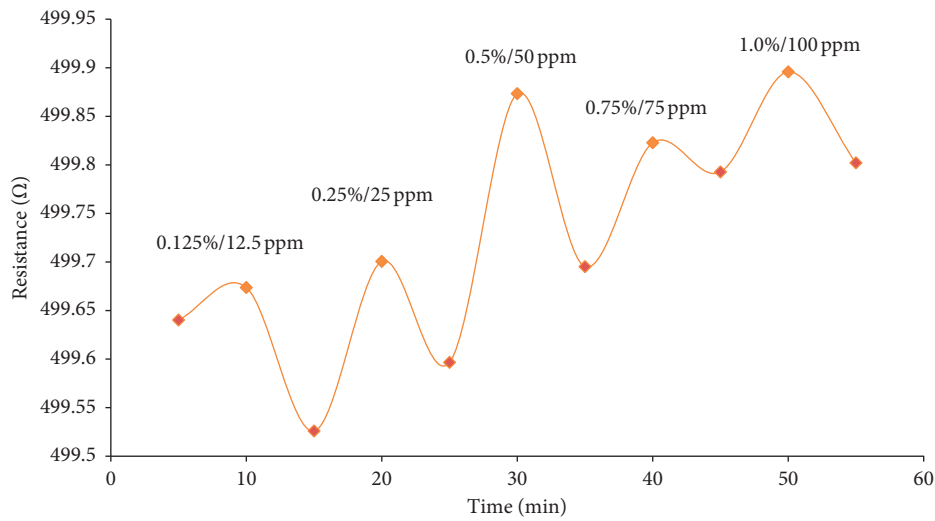
(a)

Figure 3: Continued.

(b)

(c)

FIGURE 3: Resistance changes of (a) pristine CNT, (b) CNT-carboxylic, and (c) CNT-amide towards benzene gas at room temperature.

in our case, CNTs. As it can be seen, the reciprocal changes of resistance are directly proportional to increasing concentration of benzene gas. The pristine CNTs as a sensing material showed unstable resistance reading upon exposure to benzene gas. Meanwhile, the functionalized CNTs showed the better response when increasing the benzene gas concentration.

The resistance of CNT-carboxylic increases when exposed to benzene gas, and after nitrogen gas is purged back into the system, the baseline resistance is regained. This is due to the interaction with benzene gas that shifts the Fermi level of the CNTs away from the valence band, resulting in an increase of resistance of the CNTs [32]. Because of the attachment of the carboxylic acid group on the surface of CNTs, the gas analyte most likely attached to the tail of the carboxylic group [23], which prevents the gas analyte to reach the surface of the CNTs, resulting in the same value of resistance when exposed to different concentrations of benzene gas. But, for CNT-amide, the resistance of benzene gas increased when the concentration increased. This is because the saturation effect

exists when the molecule is not desorbed completely on the surface of CNTs at room temperature unlike in the case of CNT-carboxylic. Thus, the baseline resistance of CNT-amide was difficult to regain upon the cleaning phase.

Moreover, CNTs with the functional group acts as an extra active area for gas adsorption [33], allowing more vapours to interact and eventually releasing more number of free electrons [12]. The transfer of free electron to the conduction band of oxide groups (carboxylic and amide), in the functionalized CNTs changing the hole concentration. These electrons shuttled into the nanotubes network due to positioning of tubes and the functional group. Such a process creates hole-electron recombination and reduce the number of holes in the tube. As a result, the resistance of CNTs increased as well as their sensitivity upon exposure to the benzene vapours.

Figure 4 shows a graph of the sensitivity of CNTs upon exposure to benzene gas. Sensitivity (S) of pristine CNTs and functionalized CNTs was estimated by Equation (1) [34],
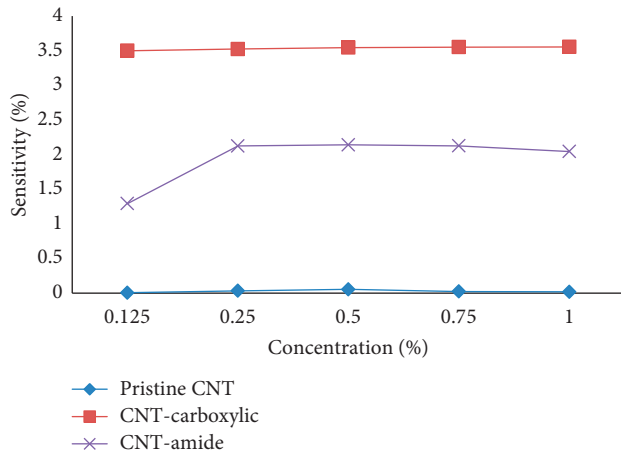
Figure 4: Sensitivity of the CNT upon exposure to benzene gas.

where R_g is the resistance of CNTs when exposed to benzene gas and R_o is the resistance of CNTs when exposed to nitrogen gas:

$$S = \frac{R_g - R_o}{R_o} \times 100\%. \tag{1}$$

From the graph, it is clearly seen that functionalized CNTs showed higher sensitivity for every concentration of benzene gas than the pristine CNTs; for example, at 0.125%, the sensitivity of the pristine CNTs is only 0.0067% compared to CNT-carboxylic (3.4995%) and CNT-amide (1.2929%). Based on this result, it can be concluded that the functionalized CNTs was highly responsive towards benzene gas due to the occurrences of a functional group on the surface of the CNTs [35].

4. Conclusion

The CNTs was functionalized with the carboxylic and amide functional groups. From the characterization analysis, it was confirmed that the functional group successfully attached on the surface of the CNTs. The functionalized CNTs shows better response and high sensitivity towards benzene at room temperature. Thus, it gives a huge impact in the detection of other gas using functionalized CNTs, a sensing material with high sensitivity and low production cost.

Data Availability

The data used to support the findings of this study are available from the corresponding author upon request.

Conflicts of Interest

The authors declare that they have no conflicts of interest.

Acknowledgments

References

[1] N. Promphet, P. Rattanarat, R. Rangkupan, O. Chailapakul, and N. Rodthongkum, "An electrochemical sensor based on graphene/polyaniline/polystyrene nanoporous fibers modified electrode for simultaneous determination of lead and cadmium," *Sensors and Actuators B: Chemical*, vol. 207, pp. 526–534, 2015.

[2] W. Al Madhoun, N. Ramli, and A. Yahaya, "Monitoring the total volatile organic compounds (TVOCs) and benzene emitted at different locations in Malaysia," *Journal of Engineering Science*, vol. 8, pp. 61–69, 2012.

[3] R. Duarte-Davidson, "Benzene in the environment: an assessment of the potential risks to the health of the population," *Occupational and Environmental Medicine*, vol. 58, no. 1, pp. 2–13, 2001.

[4] S. Zampolli, I. Elmi, F. Mancarella et al., "Real-time monitoring of sub-ppb concentrations of aromatic volatiles with a MEMS-enabled miniaturized gas-chromatograph," *Sensors and Actuators B: Chemical*, vol. 141, no. 1, pp. 322–328, 2009.

[5] G. Huang, L. Gao, J. Duncan et al., "Direct detection of benzene, toluene, and ethylbenzene at trace levels in ambient air by atmospheric pressure chemical ionization using a handheld mass spectrometer," *Journal of the American Society for Mass Spectrometry*, vol. 21, no. 1, pp. 132–135, 2010.

[6] Z. Li, C. Xu, and J. Shu, "Detection of sub-pptv benzene, toluene, and ethylbenzene via low-pressure photoionization mass spectrometry," *Analytica Chimica Acta*, vol. 964, pp. 134–141, 2017.

[7] S. Zimmermann and F. Gunzer, "Simultaneous detection of benzene and toluene using a pulsed ion mobility spectrometer," *Sensors and Actuators B: Chemical*, vol. 188, pp. 106–110, 2013.

[8] R. Emmandi, M. I. S. Sastry, and M. B. Patel, "Low level detection of benzene in food grade hexane by ultraviolet spectrophotometry," *Food Chemistry*, vol. 161, pp. 181–184, 2014.

[9] S. Camou, A. Shimizu, T. Horiuchi, and T. Haga, "Selective aqueous benzene detection at ppb level with portable sensor based on pervaporation extraction and UV-spectroscopy," *Procedia Chemistry*, vol. 1, no. 1, pp. 1495–1498, 2009.

[10] R. Leghrib, A. Felten, F. Demoisson, F. Reniers, J.-J. Pireaux, and E. Llobet, "Room-temperature, selective detection of benzene at trace levels using plasma-treated metal-decorated multiwalled carbon nanotubes," *Carbon*, vol. 48, no. 12, pp. 3477–3484, 2010.

[11] M. Leidinger, M. Rieger, T. Sauerwald, C. Alepee, and A. Schutze, "Integrated pre-concentrator gas sensor microsystem for ppb level benzene detection," *Sensors and Actuators B: Chemical*, vol. 236, pp. 988–996, 2015.

[12] V. S. Vaishnav, S. G. Patel, and J. N. Panchal, "Development of ITO thin film sensor for detection of benzene," *Sensors and Actuators B: Chemical*, vol. 206, pp. 381–388, 2015.

[13] L. Valentini, C. Cantalini, I. Armentano, J. M. Kenny, L. Lozzi, and S. Santucci, "Highly sensitive and selective sensors based on carbon nanotubes thin films for molecular detection," *Diamond and Related Materials*, vol. 13, no. 4–8, pp. 1301–1305, 2004.

[14] F. Rigoni, S. Tognolini, P. Borghetti et al., "Enhancing the sensitivity of chemiresistor gas sensors based on pristine

carbon nanotubes to detect low-ppb ammonia concentrations in the environment," *Analyst*, vol. 138, no. 24, p. 7392, 2013.

[15] S. Iijima, "Helical microtubules of graphitic carbon," *Nature*, vol. 354, no. 6348, p. 56, 1991.

[16] M. M. Chehimi, J. Pinson, and Z. Salmi, "Carbon nanotubes: surface modification and applications," in *Applied Surface Chemistry of Nanomaterials*, pp. 95–143, Nova Science Publishers, Hauppauge, NY, USA, 2013.

[17] A. S. Alshammari, M. R. Alenezi, K. T. Lai, and S. R. P. Silva, "Inkjet printing of polymer functionalized CNT gas sensor with enhanced sensing properties," *Materials Letters*, vol. 189, pp. 299–302, 2017.

[18] X. Wang, A. Ugur, H. Goktas et al., "Room temperature resistive volatile organic compound sensing materials based on a hybrid structure of vertically aligned carbon nanotubes and conformal oCVD/iCVD polymer coatings," *ACS Sensors*, vol. 1, no. 4, pp. 374–383, 2016.

[19] M. Zaki, U. Hashim, M. K. Arshad, and M. Nasir, "Characterization of difference carbon nanotube (CNTs) as a Sensing mechanism for develop of formaldehyde gas detection sensor," in *IEEE Regional Symposium on Micro and Nanoelectronics (RSM)*, pp. 1–7, IEEE, Piscataway, NJ, USA, 2017.

[20] I. V. Zaporotskova, N. P. Boroznina, Y. N. Parkhomenko, and L. V. Kozhitov, "Carbon nanotubes: sensor properties: a review," *Modern Electronic Materials*, vol. 2, no. 4, pp. 95–105, 2016.

[21] K.-Y. Dong, J. Choi, Y. D. Lee et al., "Detection of a CO and NH_3 gas gas mixture using carboxylic acid functionalized single-walled carbon nanotubes," *Nanoscale Research Letters*, vol. 8, no. 1, p. 12, 2013.

[22] S. Dhall, N. Jaggi, and R. Nathawat, "Functionalized multi-walled carbon nanotubes based hydrogen gas sensor," *Sensors and Actuators A: Physical*, vol. 201, pp. 321–327, 2013.

[23] H. Lahlou, R. Leghrib, E. Llobet, X. Vilanova, and X. Correig, "Development of a gas pre-concentrator based on carbon nanotubes for benzene detection," *Procedia Engineering*, vol. 25, pp. 239–242, 2011.

[24] N. Janudin, L. Chuah Abdullah, N. Abdullah, F. Md Yasin, N. Mohamad Saidi, and N. A. Mohd Kasim, "Comparison and characterization of acid functionalization of multi walled carbon nanotubes using various methods," *Solid State Phenomena*, vol. 264, pp. 83–86, 2017.

[25] A. Abdolmaleki, S. Mallakpour, and S. Borandeh, "Applied surface science amino acid-functionalized multi-walled carbon nanotubes for improving compatibility with chiral poly (amide-ester-imide) containing l -phenylalanine and l -tyrosine linkages," *Applied Surface Science*, vol. 287, pp. 117–123, 2013.

[26] S. Gómez, N. M. Rendtorff, E. F. Aglietti, Y. Sakka, and G. Suárez, "Surface modification of multiwall carbon nanotubes by sulfonitric treatment," *Applied Surface Science*, vol. 379, pp. 264–269, 2016.

[27] R. Abjameh, O. Moradi, and J. Amani, "The study of synthesis and functionalized single-walled carbon nanotubes with amide group," *International Nano Letters*, vol. 4, no. 2, p. 97, 2014.

[28] F. V. Ferreira, W. Franceschi, B. R. C. Menezes et al., "Dodecylamine functionalization of carbon nanotubes to improve dispersion, thermal and mechanical properties of polyethylene based nanocomposites," *Applied Surface Science*, vol. 410, pp. 267–277, 2017.

[29] F. A Abuilaiwi, T. Laoui, M. Al-harthi, and M. A. Atieh, "Modification and functionalization of multiwalled carbon nanotube (MWCNT) via fischer esterification," *Arabian Journal for Science and Engineering*, vol. 35, no. 1, pp. 37–48, 2010.

[30] Z. Zhao, Z. Yang, Y. Hu, J. Li, and X. Fan, "Multiple functionalization of multi-walled carbon nanotubes with carboxyl and amino groups," *Applied Surface Science*, vol. 276, pp. 476–481, 2013.

[31] R. Leghrib, A. Felten, F. Demoisson, F. Reniers, J. J. Pireaux, and E. Llobet, "Selective detection of benzene traces at room temperature using metal decorated carbon nanotubes," *Procedia Engineering*, vol. 5, pp. 385–388, 2010.

[32] F. A Abuilaiwi, "Hybrid gas sensor based on platinum nanoparticles/poly(methyl methacrylate)-coated single-walled carbon nanotubes for dichloromethane detection with a high response magnitude," *Sensors and Actuators B: Chemical*, vol. 35, pp. 1–8, 2016.

[33] I. Sayago, H. Santos, M. Horrillo et al., "Carbon nanotube networks as gas sensors for NO_2 detection," *Talanta*, vol. 77, no. 2, pp. 758–764, 2008.

[34] M. Y. Faizah, R. M. Sidek, and M. M. R. Naim, "Synthesis of carbon nanotubes for acetylene detection," *Journal of Engineering Science and Technology*, vol. 3, pp. 71–78, 2008.

[35] L. Q. Nguyen, P. Q. Phan, H. N. Duong, C. D. Nguyen, and L. H. Nguyen, "Enhancement of NH_3 gas sensitivity at room temperature by carbon nanotube-based sensor coated with co nanoparticles," *Sensors*, vol. 13, no. 2, pp. 1754–1762, 2013.